

ON THE DEVELOPMENT OF SMALL FORM FACTOR
HISTOTRIPSY DEVICES FOR NEUROSURGICAL
APPLICATIONS AND SMALL ANIMAL EXPERIMENTS

by

Jeffrey Woodacre

Submitted in partial fulfillment of the requirements
for the degree of Doctorate in Philosophy

at

Dalhousie University
Halifax, Nova Scotia
March 2022

© Copyright by Jeffrey Woodacre, 2022

To my ten year old self who dreamed of being a scientist.

He would be impressed.

Table of Contents

List of Tables	vi
List of Figures	vii
Abstract	xvii
List of Abbreviations and Symbols Used	xviii
Chapter 1 Introduction	1
1.1 Problem Statement	4
1.2 Research Objective	7
Chapter 2 Therapeutic Ultrasound and Cancer Treatments	10
2.1 Ultrasonic Surgical Aspirator	17
2.2 High-Intensity Focused Ultrasound (HIFU)	19
2.3 Histotripsy and Boiling Histotripsy	23
2.4 Microbubbles: Therapeutic Delivery and Ablation Assistance	29
2.4.1 Discussion on the State of Therapeutic Ultrasound in Tumor Ablation	36
2.4.2 Conclusion	40
Chapter 3 Ultrasound Transducers	41
3.1 Piezoelectric Effect	42
3.2 Piezoelectric Materials	46
3.3 Piezoelectric-Polymer Composites	50
3.4 Acoustic Matching Layers	55
3.5 Transducer Focusing	58
3.5.1 Focusing Summary	65

3.6	Transducer Modeling	65
Chapter 4	A Low-Cost Miniature Histotripsy Transducer for Precision Tissue Ablation	73
4.1	Introduction	74
4.2	Design and Fabrication	79
4.3	Characterization: No Co-registration	84
4.4	Co-registered Ablation and Imaging	95
4.5	Future Work	101
4.6	Conclusion	101
Chapter 5	Fabrication and Characterization of a 5 mm x 5mm Aluminum Lens Based Histotripsy Transducer	103
5.1	Introduction	104
5.2	Methods	108
5.2.1	Fabrication and Assembly	108
5.2.2	Acoustic Field Characterization	112
5.2.3	Drive Settings and In Vivo Ablation	114
5.3	Results	116
5.3.1	Fabrication and Assembly	116
5.3.2	Acoustic Field Characterization	118
5.3.3	Drive Settings and In Vivo Ablation	121
5.4	Discussion	125
5.5	Conclusion	132
Chapter 6	A Fresnel-based High Frequency Histotripsy Transducer for Pre-Clinical Applications	133
6.1	Introduction	133
6.2	Design and Fabrication	136

6.3	Methods	140
6.3.1	Full-Aperture Transducer	140
6.3.2	Removed Center Element Transducer	142
6.4	Results	143
6.4.1	Full Aperture PZT5A Device	143
6.4.2	Removed Center Element Transducer	150
6.5	Discussion	151
6.6	Conclusion	157
Chapter 7	Conclusion and Future Work	158
7.1	Future Work	159
Bibliography	161
Appendix A	Copyright Permissions	175

List of Tables

2.1	A table of mouse organ sizes shows that the liver is one of the largest, second to only the lungs, where most organs, except for the bowel, are less than half the size of the liver	33
4.1	The bulk properties used for each KLM layer	87
6.1	Properties Used For Fresnel Lens Design	138
6.2	Estimated Bubble Cloud Sizes for Fresnel Lens	150

List of Figures

1.1	A 145 mm aperture, annular phased array histotripsy transducer with a central hole for a co-registered imaging array, as used by Roberts <i>et. al.</i> [9]. and presented with permission by Wolters Kluwer Health, Inc. and Copyright Clearance Center.	4
2.1	(a) A purely thermal lesion with tissue damaged but intact, (b) a thermal lesion with boiling induced showing missing tissue and visible damage to surrounding tissue, (c) a mechanical tissue lesion (boiling or cavitation histotripsy) with no visible evidence of surrounding tissue damage. Image take from Khokhlova <i>et. al.</i> [43]. See Appendix A for Copyright.	15
2.2	(a) To ablate a large area, HIFU devices can be translated to create a lesion of arrays or, (b) a phased array can be used to steer the beam to ablate while holding the transducer fixed in place. Images taken from the book Therapeutic Ultrasound [55]. See Appendix A for copyright.	20
2.3	(A) A typical asymmetric waveform due to strong nonlinear acoustic behaviour (B) For cavitation cloud histotripsy (intrinsic threshold) one or two cycles reach sufficient negative pressure to cause cavitation (C) Boiling histotripsy uses less intense non-linear pulses over a longer period, relying on rapid heating to quickly boil and cause cavitation. Figure reproduced based on work by Khokhlova <i>et. al.</i> [37].	24
2.4	A shock front impinges on a gas bubble (1), reflecting and inverting the pressure waveform (2 and 3) which leads to the inverted pressure passing the intrinsic threshold and generating multiple smaller cavitation events (4). Used with permission from [71]. See Appendix A for Copyright.	25

2.5	Focused ultrasound heats a region of tissue, and at the focal center, nonlinear heating leads to rapid temperature increase and a vapor cavity forming at boiling. This vapor cavity expands, providing a reflector for follow-up acoustic waves to generate an acoustic fountain effect, leading to mechanical ablation of tissue in and around the vapor cavity. [38]. See Appendix A for Copyright Permission.	26
2.6	(a-e) The progression of cavitation events due to shock-scattering is shown, where cycles impinging on a previous bubble cloud add to the growth. (g-l) As pressure increases, the volume of cavitation events also increases, but is strictly limited to the volume above the intrinsic threshold. [71, 70]. See Appendix A for Copyright Permission.	28
2.7	As microbubbles pass through comparable sized vasculature, ultrasound insonification causes them to expand and contract, separating cells and opening the tight junctions between them. Used with permission from [55]. See Appendix A for Copyright.	30
2.8	Microbubbles can be co-injected with a therapeutic, or the therapeutic can be part of the bubble shell. When injected and insonified, the bubble can allow the drug to pass between the endothelial cells, or liquid jetting upon bubble collapse can break through endothelial cells, allowing the therapeutic (and blood) to enter the extravascular space. Used with permission from [78]. See Appendix A for Copyright.	31
3.1	(a) A typical piezoelectric medium at rest under no force nor electric field (b) A piezoelectric strains with applied electric field (c) A piezoelectric generates electric field under applied force .	43
3.2	A representative electrical impedance magnitude measurement of a piezoelectric material is shown here to illustrate the series and parallel resonances where the series resonance, ω_s , is labeled and indicated by the blue dashed line, while the parallel resonance, ω_p , is labeled and indicated by the red dashed line.	49

3.3	a) A 1-3 piezoelectric-epoxy composite starts with a solid piece of piezoelectric material. b) After two sets of perpendicular cuts are made, a matrix of pillars is left with a solid piezoelectric base. c) The space between pillars is filled with epoxy which can be sanded, machined, or lapped down to the top surface of the pillars. d) The solid base is removed through lapping or grinding, leaving a matrix of pillars embedded in epoxy. . . .	50
3.4	For PZT-5H and Spurr Epoxy, a) the value of \bar{k}_t plateaus and stays above k_t for the solid ceramic above volume fractions of 5%. b) The speed of sound for the composite varies non-linearly between the value for the epoxy alone and the value for the ceramic alone. c) The acoustic impedance, \bar{Z} , increases linearly from the value for Spurr epoxy at 0% volume fraction to 90% where the slope changes to reach a final value of 36.5 MRayl.	53
3.5	A single matching layer, acoustic impedance Z_m and thickness l , is placed between an initial and final acoustic medium to improve acoustic intensity transmission.	57
3.6	The transmitted acoustic intensity through a matching layer as a function of layer thickness which is given as a fraction of the acoustic wavelength is presented here. In this example, the initial medium has an acoustic impedance of 33.6 MRayl, and the final medium has an acoustic impedance of 1.5 MRayl. Multiple plots show how the transmission improves as the matching layer impedance increases from 1.5 to 7.1, and then drops again up to 33.5 MRayl.	57
3.7	Fermat's Principle states that, to achieve lens focus, the time of flight for a plane wave traveling path $d_l + d_m$ must equal the time of flight for a wave on path $s_l + s_m$, where s and d are distances, and v_l and v_m are sound velocities in the lens and medium, respectively	59
3.8	a) Multiple lens curves offset by a distance D_f share a focus at 8 mm. b) Linking the curves and trimming them outside the linked areas leads to the shape seen here, and revolving this curve around the focal axis gives a lens c) which can be machined.	61

3.9	Composites one through three (1-3) failed during attempts to curve them, where four (4) failed during ultrasonic cleaning and five (5) failed during bonding due to the substrate being too thin	62
3.10	A cross-section and top view of an annular array are shown here, where the electrodes are crosshatched orange, showing distinct separations between each element. On the right, electrical pulses are sent to each element with a delay, where the outer element receives the pulses earliest as sound emitted from these elements must travel further to reach the focal zone . . .	64
3.11	Generic KLM matrices multiplied together can relate any number of input-output relationships together. Here, the ABCD elements vary for each matrix	67
3.12	The model used for KLM simulations of a single-element piezoelectric transducer, where each outlined variable or set of variables is a single, 2x2 matrix in the KLM model or, in the case of the ports, an input/output.	69
3.13	The thickness of a lens varies with position along the curvature, so multiple KLM models must be used. Here, the smooth curve of a lens is discretized into multiple separate 1-D models. . .	70
3.14	A grid of points in an FEM model, where the lens material is labeled in yellow, the water medium in blue, and a red-line represents the pressure source.	71
4.1	A cross-sectional view of the transducer design shows an air-backed piezoelectric composite with an aluminum lens and parylene matching layer. The lens-piezo stack can be seen in the picture.	79
4.2	From the KLM model, the addition of a 20 μm epoxy layer shifts the output efficiency of the composite-lens-matching layer device from peaking at 4.5 MHz to 6.8 MHz, while also improving upon overall efficiency.	82

4.3	The electrical impedance of a bare piece of 10 mm diameter composite is shown here, with a KLM model closely matching. This measurement was performed with air backing and an air load on the composite.	86
4.4	The upper plot shows the electrical impedance magnitude of a composite-lens stack along with KLM models both with and without the bonding epoxy between composite and lens. Modeling the bonding epoxy is necessary to ensure the KLM resonance matches the measured resonance. Discrepancies are likely due to the inability of KLM to model internal lens reflections. The lower plot shows the electrical impedance phase where, again, the addition of 20 μm of epoxy allows KLM to more closely match the phase characteristics.	88
4.5	The transducer pressure field was measured centered at the focus, where the transducer was driven at 20 V with a 6.8 MHz, 20 cycle pulse. The acoustic waves are propagating in the axial direction. The focal -3 dB width in the radial direction is shown as measuring 0.145 mm, while the axial -3 dB length is 0.698 mm.	90
4.6	The 10 mm diameter transducer focal pressure as a function of drive voltage was measured at steady-state using a hydrophone. A linear relationship between pressure and drive voltage is seen from 2.5 V up to 17 V. Above 17 V, initial evidence of cavitation at the hydrophone tip was seen as noise in the oscilloscope signal. At 25 V, cavitation at the hydrophone tip made pressure measurements inconsistent and, therefore, measurements were stopped. The inset plot shows a one-way, single-cycle pulse response as measured with the hydrophone. The ringing after the initial pulse is likely due to reverberations within the lens. The pulse bandwidth is 59%.	92

4.7	A cavitation bubble cloud is shown as a white spot here due to averaging of multiple camera frames to produce an image. The bubble cloud measures approximately 263 μm in length, and 124 μm in diameter. A 26 gauge needle with a nominal 464 μm diameter is seen on the right for scale.	94
4.8	The histotripsy ablation lens here has a center-hole to allow an imaging tool to visualize the area in real-time during ablation. This particular endoscope is a 64-element, 40 MHz phased array endoscope designed and fabricated in-house[12].	96
4.9	Using a hydrophone, the 10 mm, co-registered ablation transducer focal pressure was measured as a function of drive voltage. A linear relationship between pressure and drive voltage is seen from 15 V up to 50 V. At 50 V, initial evidence of cavitation at the hydrophone tip was seen and measurements were stopped.	97
4.10	In the upper image (a), a Chinchilla cerebellum is imaged showing the molecular layer (dark layer), the granular layer (highly specular), and white matter tracts (thin dark lines in granular layer). In the lower image (b) which is of the same tissue slice, a histotripsy bubble cloud, visible as a highly specular region near the image center, has been plunged into the cerebellum. Both images were collected in real-time using a co-registered 40 MHz endoscopic phased array. The arrows in (b) point out the track followed by the bubble cloud, with the upper arrow pointing to the ablation entrance.	99
4.11	The co-registered transducer pressure field was measured centered at the focus, where the transducer was driven at 40 V with a 6.8 MHz, 20 cycle pulse. The acoustic waves are propagating in the axial direction. The focal -3dB width in the radial direction measures 0.116 mm, while the axial -3dB length is 0.752 mm.	100

5.1	On the left, a transducer schematic cross-section shows an air-backed piezoelectric element, in this case either a 1-3 PZT-5A-epoxy composite or Pz-39, with an elliptically machined aluminum lens topped with a quarter-wavelength parylene-C matching layer. A 1.0 mm x 0.5 mm piece of flexible circuit board is adhered to the back with cyanoacrylate glue and electrically connected to the piezo via wirebonds. A wire is soldered to the piece of flexible circuit for external connection. Ideally, the piezoelectric element would have an acoustic impedance matching that of aluminum - 17 MRayl. The inset image seen top-right is of the final machined lens on a finger-tip for scale.	109
5.2	Two devices fabricated using Pz-39 (left, center) and one using PZT-5A composite (right). An SMA connector on the rear allows cabling connection to a pulser.	111
5.3	A schematic of the in vivo experiment shows the imaging probe and histotripsy probe co-registered and targeted through the craniectomy opening. The devices are attached to a motorized positioning arm for targeting.	115
5.4	The electrical magnitude and phase for a PZT-5A transducer (black solid lines) and a Pz-39 transducer (maroon dashed line) are shown after the lens and piezo are bonded which adds a number of damped resonances.	117
5.5	The peak-to-peak focal pressure vs drive voltage for a 5 mm x 5 mm lens PZT-5A composite transducer is plotted in black with a linear fit, showing a pressure increase of 20.9 MPa / 100 V in the low-voltage regime. For the Pz-39 transducer, plotted in red, a linear fit shows a pressure increase of 35.8 MPa / 100 V.	118

5.6	A surface plot of the measured pressure field in a focal-intersection plane normal to the direction of acoustic propagation shows a -3 dB width of 0.31 mm and a FWHM of 0.43 mm in both the x-direction and y-direction. Side lobes are seen symmetrically positioned about the peak which measure, at most, 20% of the peak pressure. The red dashed line plotted along the x-position versus pressure axis shows a kWave simulated pressure measurement, where the FWHM is found to be 0.42 mm in both the x and y-directions.	119
5.7	The normalized pressure measured along the symmetry axis of the transducer through the focus, along with a k-Wave simulated pressure along the same axis. The measured -3 dB depth of field for our transducer was found to be 1.9 mm, while the simulated -3 dB depth of field is 2.1 mm. Measured -6 dB beam length was 2.9 mm.	120
5.8	The axial peak positive and negative pressures for a 6 mm focused transducer at simulated drive levels of 10, 30, 50, 70, 90 and 110 V show the progression of pressure asymmetry as the field becomes nonlinear.	121
5.9	After driving the PZT-5A device to 600 V some resonance behaviour seen as a spike in phase at 6.2 MHz is observed, while a shift in the impedance magnitude suggests a drop in the clamped dielectric as a whole.	122
5.10	A B-mode image taken on the right side of the brain near Bregma-6.0 mm during histotripsy treatment shows the bubble cloud as a small bright spot within the labeled region of interest. The brain midline, cortex, midbrain, and edge of the skull are all indicated.	123

5.11	A temporal progression of B-mode images with Power Doppler overlay focused on the ablation region from Figure 5.10 shows that from time $t = 0$ s, when ablation is initiated, to time $t = 12$ s, just prior to ablation cessation, the ablation zone grows, leaving an anechoic region indicated in frame $t = 13$ s. At time $t = 38.5$ s, 25.5 s after stopping treatment, the anechoic region has regained specularity.	124
6.1	Multiple curves (black) all focused to the marked axial location at 8 mm (X) and offset from each other by a distance D_f form the basis of the Fresnel lens. For this work, moving along each curve and stepping back to the next curve once the axial position reaches 0.64 mm creates the blue dashed line which can be revolved about the symmetry axis to form the Fresnel lens surface shape.	137
6.2	Top, side, and cross-section renderings of the final lens design are shown along the top, where the cross-section shows six separate surfaces. The bottom left and right images show the final machined Fresnel lens, both without and with a hole for co-registered imaging.	139
6.3	Normalized focal pressure measurements from a single, two (2), three (3) and five(3) cycle 6.0 MHz pulse are plotted with the single-cycle response additionally plotted in red for the two, three and five cycle responses. Arrows on the upper curve indicate the pulse arrival times from the center zone and the first three Fresnel rings.	144
6.4	Normalized focal pressure measurements from a single, two (2), three (3) and five(3) cycle 6.0 MHz pulse are plotted along with their respective time-domain Finite Element Method (FEM) simulations.	145
6.5	The 8.0 V drive level steady state focal pressure as a function of frequency swept from 5.8 to 6.5 MHz, showing a peak at 6.1 MHz with a pressure plateau from 6.05 MHz to 6.3 MHz. . . .	146

6.6	Three curves show the focal pressure at 6.1 MHz for a device without coatings (black), the same device with a quarter-wave matching layer (thick grey) and that device with a quarter-wave matching layer and the lens curve filled with epoxy. Parylene increases the peak-to-peak pressure output by 45% from 2.2 MPa to 3.2 MPa, and the epoxy reduces pressure output by 6% from 3.2 MPa to 3.0 MPa.	147
6.7	A surface plot of the measured pressure field in a focal-intersection plane normal to the direction of acoustic propagation shows a FWHM of 0.34 mm in the x-direction and 0.29 mm in the y-direction. The red dashed line shows COMSOL simulated pressure measurements, where the FWHM is calculated 0.274 mm.	148
6.8	The black curve shows the measured pressure versus axial position around the focus for the PZT5A Fresnel lens, while the red dashed line provides a simulated result. The measured -3 dB beam lengths are 0.88 mm and 0.99 mm for the measured and simulated data and 1.23 mm and 1.48 mm at -6 dB. . . .	148
6.9	Six bubble cloud images, each composed of N median-filtered images at their respective voltages, show the cloud size increasing as drive voltage is increased from 190 V to 370 V. The 190 V cloud includes two curves - brightness versus position on the plot through the largest radial and axial portions of the cloud.	149
6.10	The pressure per voltage in units normalized to the peak full-aperture device pressure, where the device with a missing center element shows a slope of 8.68 arbitrary pressure units per 100 V, compared to the 14.00 a.u. per 100 V. This is a 38% reduction in pressure.	152

Abstract

The development of surgical instruments is a growing area where histotripsy is relatively under represented. This work focuses on the miniaturization of histotripsy devices for introduction into the neurosurgery, cardiac, and tumor resection fields. Three devices were developed where the key to miniaturizing was a novel transducer stack using an elliptical aluminum lens.

A 10mm aperture aluminum lens histotripsy transducer with an f-number of 0.7 was fabricated using an air-backed 5.0MHz, PZT-5A, 1-3 dice-and-fill piezoelectric composite. A KLM model of the device showed maximum output pressure at 6.8MHz. Cavitation was observed in water by driving the composite with a single-cycle, 6.8MHz pulse at a 50Hz PRF and a bubble cloud 264 μ m long by 124 μ m wide was measured, demonstrating the highest frequency histotripsy bubble cloud to date. Co-registered imaging through the lens center was added by inserting a 30MHz phased array endoscope. Ex-vivo sub-surface tissue ablation was also demonstrated.

Two 5mm square aluminum lens histotripsy devices were built with two materials: a 40% volume fraction 1-3 PZT-5A composite and Pz-39, a porous ceramic. The composite-based device could not cavitate in water up to a 600V drive level, whereas the Pz39 based device was able to cavitate in water at a drive level of 220V. In vivo ablation of rat brain tissue was demonstrated through a skull opening while monitoring using an endoscopic 30MHz ultrasound phased-array with B-mode imaging and power Doppler overlay. Power Doppler showed the ablation zone grew steadily over 12s. Immediately after treatment the ablated area appeared anechoic, slowly becoming specular.

The final project focused on developing a 15mm diameter Fresnel-lens device, filling the lens with epoxy to create a flat aperture to simplify coupling. The Fresnel lens has a reduced curvature compared to a non-Fresnel lens, allowing integration of an imaging endoscope without excessive signal loss in the epoxy. The device was designed for 6MHz, and demonstrated free-field cavitation in water. Hydrophone measurements showed the optimal drive frequency was 6.0MHz, as designed. The center element was removed to demonstrate future endoscope integration, and although approximately 40% pressure loss was observed, the device was still capable of free-field cavitation.

List of Abbreviations and Symbols Used

Sign	Description	Unit
C_0	clamped capacitance	F
D	dielectric displacement	C/m^2
D_f	offset distance between fresnel rings	m
E	electric field	V/m
N_f	integer cycles delay in Fresnel lens at frequency, f	unitless
S	strain	m/m
T	stress	N/m^2
ϵ	permittivity	unitless
$\tan\delta_e$	dielectric loss factor	unitless
ω_p	parallel resonance frequency	rad/s
ω_s	series resonance frequency	rad/s
\bar{Z}	characteristic acoustic impedance of a composite	MRayl
$\bar{\epsilon}^S$	clamped dielectric constant of a composite	unitless
\bar{c}_0	acoustic wave propagation speed in a composite	m/s
\bar{k}_t	transversely clamped electromechanical coupling factor for a composite	unitless
c_0	acoustic wave propagation speed	m/s
d	piezoelectric constant	
d_x	distance off-axis in medium x during lens calculation	m
f_p	parallel resonance	Hz
k^2	electromechanical coupling factor	unitless
k_t	transversely clamped electromechanical coupling factor	unitless
l	piezo thickness	m
s	elastic modulus	unitless

Sign	Description	Unit
s_x	distance along focal axis in medium x during lens calculation	m
v_l	longitudinal wave speed in lens material	m/s
v_m	longitudinal wave speed in acoustic medium	m/s
Q	mechanical Quality Factor	unitless
BH	boiling histotripsy	
CUSA	Cavitron Ultrasonic Surgical Aspirator	
FEM	Finite Element Method	
FWHM	full-width at half maximum	
HIFU	High-Intensity Focused Ultrasound	
KLM	Krimholtz, Leedom, and Matthae	
MIS	minimally invasive surgery	
MRI	magnetic resonance imaging	
TID	thermal isoeffect dose	

Chapter 1

Introduction

It has been shown for a number of surgical procedures that a minimally invasive surgery (MIS) approach, when compared to open surgery, can offer improved patient outcomes including: less blood loss, fewer complications, faster recovery time, and a reduced chance of infection[1, 2, 3, 4]. These outcomes have led to a surgical trend of avoiding open surgery in favor of MIS, when possible [5, 6]. To allow more procedures to be performed as minimally invasive, it is important to develop new tools to add to a surgeon's repertoire, with the logical extension being if MIS procedures are good for patient outcomes, then fully non-invasive procedures should be better still, assuming the same surgical goal can be achieved.

The development of surgical instruments and equipment is a growing area of interest among businesses and researchers alike. From 2016 to 2025 the global surgical equipment market is expected to increase from a value of USD 10.5 billion to an estimated value of USD 20.3 billion in 2025, according to a new report by Grand View Research, Inc [7]. With this in mind, research into surgical tools could gain

a lot of attention from physicians and medical device companies who wish to be at the forefront of this technology growth while, additionally, the long-running surgical trend toward MIS/non-invasive procedures means a large portion of this funding and research could be aimed toward MIS devices. A relatively new surgical technology which shows promise as being a disruptive force in MIS/non-invasive treatments is an ultrasound ablation technique known as histotripsy.

Histotripsy, translated from Greek as 'soft-tissue breakdown', is a tissue ablation technique which was first explored in 2004 by Xu *et. al.* [8] where, at the time, histotripsy was known under the acronym, CUTE, meaning Controlled Ultrasound Tissue Erosion. Histotripsy uses high-intensity short duration ultrasound pulses to cause cavitation in soft-tissue, ablating it and leaving the broken down tissue remains. Following their publication, the University of Michigan group who published the aforementioned paper, under the leadership of Professor Charles A. Cain, went on to publish numerous papers on the effects of histotripsy on various tissues, optimization of histotripsy parameters during tissue ablation, and then began a company to market histotripsy as a surgical tool. The bulk of work performed on histotripsy so far is with respect to cancer treatments, specifically tumor ablation, with some work additionally focused on thrombolysis. For all of their work so far, the University of Michigan Histotripsy group has used extracorporeal histotripsy transducers, similar to that shown in Figure 1.1 where this particular device was used to ablate renal tissue in a

rabbit model [9].

These transducers transmit acoustic energy through the skin, into the body causing ablation at a focal point. No incision in the body is needed for many histotripsy treatments, making them fully non-invasive. The particular device shown in Figure 1.1 has a co-registered 2.5 MHz imaging probe to monitor the ablation in real-time. A review on histotripsy literature will be performed in Chapters 2 and 3, however, for now it should be noted that using large, extracorporeal transducers, histotripsy treatments cannot be easily performed adjacent to bone or near organs such as the lung or colon where there are pockets of gas. When this work began, there were no trans-cranial histotripsy devices so the only surgical ultrasound-based option for resection was the cavitation aspirator - a tool with a rapidly oscillating ablation tip which causes tissue destruction through direct contact. The project goal was, and still is, to provide a neurosurgical alternative to these aspirators. As of now trans-cranial devices exist in a research capacity, however, there are still some difficulties in treating the brain as the skull attenuates and reflects the extracorporeal histotripsy pulses limiting the usable frequencies and therefore ablation size, while imaging feedback remains limited to MRI-guidance without a partial craniotomy, also due to the acoustic properties of the skull. The current state of histotripsy neurosurgical applications leaves a great deal of room for researchers to explore, ranging from new device development to histological and neurological effects on the tissue itself, especially as

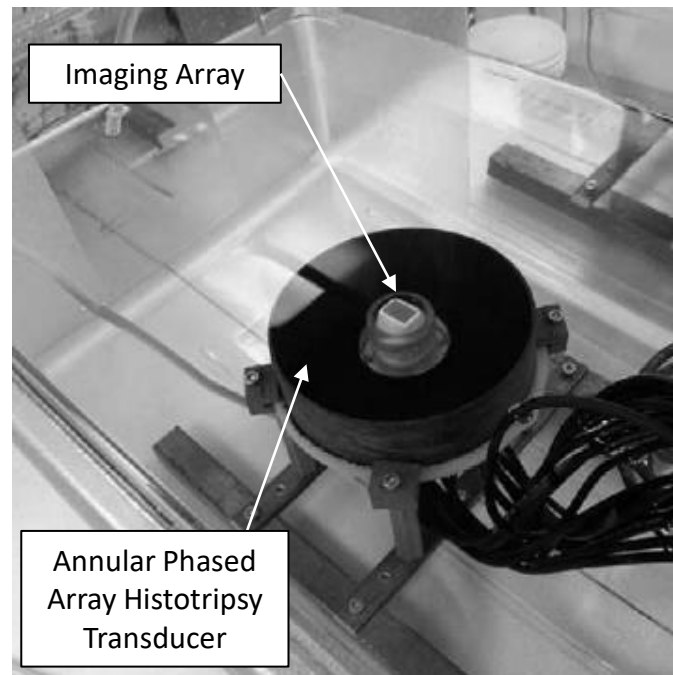


Figure 1.1: A 145 mm aperture, annular phased array histotripsy transducer with a central hole for a co-registered imaging array, as used by Roberts *et. al.* [9]. and presented with permission by Wolters Kluwer Health, Inc. and Copyright Clearance Center.

the benefits of histotripsy to neurosurgery include: ability to target and ablate a volume without damaging intervening tissues, non-thermal damage to surrounding tissue, real-time guidance if co-registered ultrasound imaging through the skull were possible, and synergy with immunotherapy treatments. With all of the above in mind this leads to the problem statement of my thesis.

1.1 Problem Statement

The current gold standard for neurosurgery is the partial craniotomy, where surgeons remove a small piece of the skull near the target site and perform resections or incisions

using optical feedback, guided by pre-operative MRI images which only provide an idea of where treatments need to take place. The tools used tend to be small to minimize damage to the brain and can allow access down the sulci if needed, so it is hypothesized that if a small, hand-held endoscopic histotripsy tool existed with the ability to image and ablate at depth without damaging the intervening tissue, surgeons may use it.

Histotripsy cannot easily be performed transcranially using the current generation of extracorporeal transducers because, as mentioned above, the skull blocks and reflects a large amount of acoustic energy. Lu *et. al.* [10] has performed pre-operative magnetic resonance imaging (MRI)-guided histotripsy ablation in a pig brain through an excised human skull although mean targeting accuracy was 2.3 mm between targeted ablation and actual ablation. Tumor ablation within the brain can also be performed using High-Intensity Focused Ultrasound (HIFU) with MRI guidance where this is done by monitoring small temperature increases near the HIFU focus to guide the treatment and then increasing power once the focus is as desired [11]. For histotripsy, this MRI guiding technique cannot be used directly as histotripsy is an on-off ablation technique and therefore could not be slowly ramped up to find focus. One caveat is that MRI can detect a temperature increase, so focus may be gained through creation of a small local temperature increase prior to histotripsy ablation. These current trans-cranial devices are relatively low frequency (<1 MHz) and so

there are fundamental limitations in the achievable precision, especially without real-time feedback. As was mentioned, currently surgeons use optical feedback to guide their work; however, this is limited to only the tissue surface and can lead to incidental damage to sub-surface arteries while also requiring electrical stimulation checks for nerve detection. With histotripsy ablating tissue below the surface, a real-time, high precision imaging modality is needed to avoid these potential pitfalls.

Our lab has developed an endoscopic form factor ultrasound probe capable of imaging sub-surface tissue which would be ideal for these neurosurgeries [12] and, additionally, we have developed the supporting electronics [13] to image with these probes. This solves the problem of imaging tissue sub-surface, so, if we could package this imaging probe together with an endoscopic form-factor histotripsy device we can then provide surgeons with a tool or tools which could change the way neurosurgery is performed. Currently, an endoscopic form factor histotripsy tool does not exist, and there will be challenges associated with combining both an imaging and ablation probe into a single, small device, so preliminary work in the development of such a tool will be broken down into tasks outlined in the following section.

So, overall it is believed that a device which can provide high-quality real-time imaging feedback while also being capable of precision ablation for sensitive areas of the brain, all under the umbrella of treating cancer through tumor ablation could be a disruptive technology within the field, displacing many of the current treatment

devices.

1.2 Research Objective

The goal of my PhD was to build up a base of work which could eventually lead to the development of a tool, integrating both a histotripsy transducer and a high-frequency ultrasound imaging array into a single co-registered device, allowing surgeons to both image and ablate tissue on a very fine scale. For a tool measuring 5 mm x 5 mm or smaller, the target would be endoscopic neurosurgery, cardiac surgery, pancreatic surgery, and potentially thrombolysis, but there is also great potential in pre-clinical small animal research for a somewhat larger device that is capable of high precision targeting and ablating anywhere in an animal model without the need for a water bath for coupling. The overall task of developing both a small endoscopic device and a small-animal device can be broken down as follows:

1. Develop a 10 mm aperture co-registered histotripsy transducer: This task, outlined in detail in Chapter 4 was the development of a 10 mm aperture histotripsy transducer that could be co-registered with our current generation of imaging endoscope. Included are simulations, steps for transducer fabrication, and testing on tissue. At the time of publication, this was the smallest histotripsy device to exist.
2. Develop a 5 mm aperture histotripsy transducer, without co-registered imaging:

This task, outlined in detail in Chapter 5, was to create a histotripsy device the size of an endoscope or surgical aspirator, capable of performing tissue ablation.

3. Develop a hand-held small-animal histotripsy device using what was learned in Tasks 1 and 2. This task, outlined in detail in Chapter 6, is to build upon the knowledge from tasks 1 and 2 and to use a Fresnel lens to remove the deep lens curvature needed for a larger device, developing a useful flat-aperture device, capable of co-registered imaging and ablation in small animal models. This would allow researchers to easily expand upon existing work on the in-vivo effects of histotripsy. It is believed that this device could allow researchers to rapidly expand into the histotripsy field by reducing the cost-barrier on transducers.

Each of the above tasks combined are the bulk of this PhD thesis work. In Chapter 2, a background review on the current state of ablative treatments and therapeutic ultrasound is performed, with discussion focusing on method of action, tumor ablation, and cancer treatment modalities. Chapter 3 provides background information in ultrasound transducer fabrication. In Chapter 4, the work to develop a 10 mm co-registered histotripsy transducer is presented with simulations, fabrication steps, and experimental results of tissue ablation. In Chapter 5, the development of a 5 mm square aperture device is presented, again, with steps for fabrication and

experimental results. Chapter 6 presents simulations and fabrication steps in the development of a Fresnel-based small animal device. Finally, Chapter 7 summarizes the results, how they contributed to the field of histotripsy device development, and what future directions should be explored.

Chapter 2

Therapeutic Ultrasound and Cancer Treatments

Given the ultrasound devices developed in this work are being targeted in cancer treatment and research, this section provides cancer and therapeutic ultrasound background within that scope.

Cancer is one of the leading causes of death world-wide, where, in the United States in 2017, cancer was reportedly the second leading cause of death (approx. 600,000 total) behind only heart disease (approx. 650,000 total)[14]. The key to successfully treating any cancer is early detection, where in many common cancers if found prior to growth into nearby tissue, the treatment methodology is almost always surgical or potentially combined with chemotherapy[15]. However, surgical treatments do not come in a one-size-fits-all package and the consensus of what treatment is best constantly changes as new technology is developed, and can vary depending on tumor location, size, as well as patient health.

In the liver, for example, surgical tumor treatment options in the past involved open-surgery for either resection or full transplant, and were limited to tumors which

had not spread. In the early 1990's, ultrasound-guided radio-frequency (RF) ablation was commercialized for liver treatment as was percutaneous microwave hyperthermia, allowing surgeons to use less invasive methods to treat smaller tumors or tumors which could not easily be resected due to blood supply proximity [16]. RF ablation is now accepted as a curative treatment in some parts of the world for very early stage tumors [17]. More recently, surgeons in general have started to move toward performing laparoscopic/non-invasive surgeries due to their inherently reduced risk, the benefits of which include: reduction in blood loss, fewer complications, faster recovery time, and a reduced chance of infection [2, 3, 4, 18, 19, 20, 1]. This shift toward minimally invasive treatments has resulted in a push to research minimally invasive techniques [5, 6], many of which are ultrasound-based, for fully non-invasive cancer treatments. The use of ultrasound-based surgical tools is not a new concept as ultrasound has been used in surgical applications since 1978 when the Cavitron Ultrasonic Surgical Aspirator (CUSA) was introduced as a neurosurgery tool [21].

The CUSA, an ablation device which uses a rapidly oscillating tip to break-up tissue on direct contact - acting essentially as an 'ultrasonic jackhammer', was quickly taken up in general surgery where, for example in the early 1980's, Hodgson [22] was able to effectively and rapidly de-bulk rectal and liver tumors. The CUSA has since been further used in additional liver resections [23, 24] as well as renal surgery [25]. Note, that these early surgeries were performed on soft-tissue, but the modern

iteration of the CUSA is also capable of ablating dense, calcified tissue and even bone [26]. Although widely used in surgical applications, the CUSA is limited to targeting areas the surgeon can see and physically reach. Another ultrasound-based technique, commonly known as high-intensity focused ultrasound, or HIFU, offers a fully non-contact ultrasound-based ablation technique allowing treatments to take place without tissue resection.

HIFU, typically used in reference to ultrasonic thermal ablation, was not seriously considered for clinical usage until precise dosage monitoring and targeting was made possible, as HIFU uses a focused ultrasound transducer to cause tissue necrosis through sustained ultrasound absorption. The result is cell hyperthermia, typically a few mm within the focal zone [11], and surgeons needed accurate targeting to avoid collateral damage as much as possible while ensuring the specific tissue was successfully ablated. High precision monitoring came from combining HIFU with magnetic resonance imaging, often abbreviated as MRgHIFU (magnetic-resonance guided HIFU), which could be used to monitor treatment anywhere in the body. Ultrasound monitoring could also be used in areas, such as the prostate, where the presence of cavitation or vapor bubbles when tissue temperature is raised to boiling levels [27] are clearly visible in a B-mode image. More recently, it has been shown possible to correlate ultrasound B-mode brightness measurements with temperature increase [28]. HIFU has been used to treat tumors in the prostate, breast and liver, among

other organs with, in many cases, reported successes in tumor reduction and/or pain relief [29]. It has also been used transcranially to treat tumors such as glioblastoma multiforme (GBM), essential tremor, and tremor caused by Parkinsons disease [30]. HIFU treatments leave the tissue intact, but dead through coagulation necrosis. In cases where it is critical to avoid thermal damage a non-thermal version of HIFU, sometimes called cavitational-HIFU, cHIFU or more commonly, histotripsy, is an alternative ultrasound tumor treatment method which relies on cavitation to break-up and liquify tissue.

Histotripsy, a tissue ablation technique which was first explored in 2004 by Xu *et. al.* [8], uses very high-intensity short duration ultrasound pulses to cause cavitation in soft-tissue, ablating it and leaving the broken-down tissue remains. This differs from thermal-HIFU which causes cell death through coagulation necrosis. Histotripsy causes tissue fractionation through short, powerful cavitation-inducing ultrasound bursts where the destruction is caused by cavitation bubbles collapsing [31] and inducing large internal shear loads in the tissue. Histotripsy has had a number of published animals trials reporting on the efficacy of treating ailments such as benign prostatic hyperplasia in a canine model [32, 33], hepatocellular carcinoma on a porcine model [34], and thrombolysis in a porcine model [35]. Additionally, recent work has been reported on neural treatments in a porcine model [36] with the goal of

eventually treating blood clots as well as brain tumors. Another similar ultrasound-based ablation technique that also uses cavitation, but with reduced power, longer duration pulses, is boiling histotripsy.

Boiling histotripsy, similar to histotripsy, breaks up tissue through mechanical fractionation. However, the initiation of the cavitation event occurs due to rapid, on the order of milliseconds, boiling of the target tissue due to non-linear absorption of ultrasound. The result of this boiling is a vapor cavity that expands quickly and further interacts with impinging acoustic waves to create acoustic micro-fountains which cause water to rapidly jet away, destroying the surrounding tissue. Similar to histotripsy, this effect, when controlled effectively, is non-thermal and does not damage surrounding tissue[37, 38]. Boiling histotripsy is a more recent development compared to HIFU and histotripsy, so at this time experimental work seems to be limited to ex-vivo experiments such as those on bovine heart and liver[39] for lesion measurements, murine tumor models [40, 41], and a preliminary in-vivo healthy porcine model for testing liver and kidney ablation [42].

As a visual comparison of tissue effects between HIFU, a more aggressive HIFU where the tissue reached boiling, and histotripsy, observe the three lesions in Figure 2.1. The first, labeled *a* shows a thermal lesion (small white area) which would be representative of a HIFU treatment where the tissue remains intact, however the cells in the targeted volume would have gone through some kind of necrosis leading to

death [43]. This type of treatment, in Figure 2.1a, would require accurate dosimetry or MRI assistance to create consistent ablation regions and avoid collateral damage. The second image, Figure 2.1b, shows what could happen in a HIFU style treatment at higher acoustic intensities, where uncontrolled boiling has been induced at the focus leading to thermal lesions with a vaporized core. This boiling induced ablation could be visualized with ultrasound imaging as the boiling would be clearly visible in a standard B-mode ultrasound imaging modality, or with MRI to determine the thermal effects to surrounding tissue. Figure 2.1c shows the effects of a mechanical fractionation, caused by either histotripsy or boiling histotripsy, where tissue is clearly missing but no visual indication of thermal damage such as discoloration surrounding the ablation site exists.

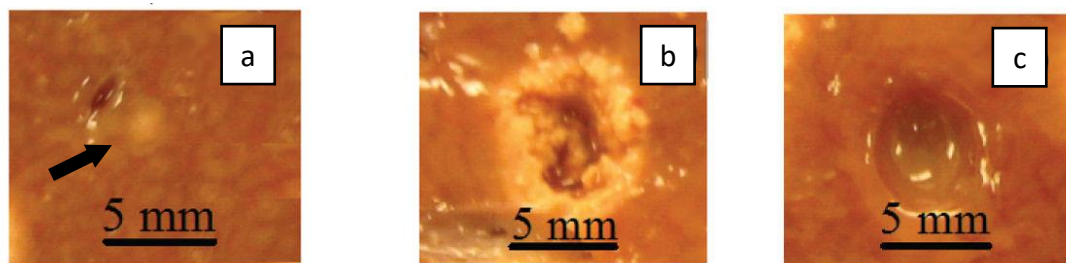


Figure 2.1: (a) A purely thermal lesion with tissue damaged but intact, (b) a thermal lesion with boiling induced showing missing tissue and visible damage to surrounding tissue, (c) a mechanical tissue lesion (boiling or cavitation histotripsy) with no visible evidence of surrounding tissue damage. Image taken from Khokhlova *et al.* [43]. See Appendix A for Copyright.

As an alternative to tissue ablation, ultrasound assisted chemotherapy drug delivery using microbubbles has been explored as a way to deliver drugs to specific tumor locations more effectively. Originally designed as a contrast agent to improve

ultrasound imaging, microbubbles, under sufficient ultrasound intensity, were found to also disrupt the surrounding vasculature allowing pharmaceuticals to enter more readily at the insonified location [44]. The microbubbles themselves can either have the drug incorporated into their design, releasing it at their target location when targeted with ultrasound, or the bubbles can be injected along-side the drug of interest, assisting uptake of the drug by opening pores in the nearby cell walls [45] or opening the junctions between cells for a short time [46].

A common area of research for microbubbles in cancer treatment is opening of the blood-brain barrier, which is known to be relatively impermeable to standard dosages of chemotherapy treatments, and allowing delivery of anti-cancer drugs such as doxorubicin (DOX) and bis-chloroethylnitrosourea (BCNU) more effectively to tumor sites in the brain [47]. Efficacy of DOX delivery has also been improved in a mouse liver model through the destruction of microbubbles bound to hepatic tumor blood vessel walls [48] allowing the drug to enter surrounding tissue. Additionally, microbubbles have been associated with an increased efficacy of HIFU liver ablation treatments in rabbit models which the authors attributed to either additional heating due to US absorption of the bubbles, or cavitation damage due to microbubble implosion [49], as well as improved outcomes for treatment of pancreatic cancer with gemcitabine[50].

Given that each of the above mentioned ultrasound-based techniques have been

used in a variety of cancer treatments on tumor types in both animal models and human clinical trials, it is important to more closely examine the method of action for each treatment, its effect on surrounding tissue, and its targetability to gain a better understanding of when each should be used. In the following section, each treatment technique will be functionally explained in detail, its limitations provided, and a comparison given between each other technique to better understand when and where each may be used.

2.1 Ultrasonic Surgical Aspirator

Ultrasonic surgical aspirators such as the Sonopet (Stryker Corporation, Kalamazoo, MI, USA) or CUSA (Integra LifeSciences Corporation, Princeton NJ, USA), are contact-based mechanical ablation tools with adjustable power and frequency to control how aggressively tissue is removed. The CUSA works by driving an electric coil within the handpiece with a user variable amplitude alternating current at 23 kHz or 36 kHz, depending on the handpiece used, which in turn induces an oscillating magnetic field. The transducer, a nickel laminate alloy, couples with the magnetic field, oscillating at controllable amplitudes up to 355 μm in the CUSA Excel . This oscillating transducer connects directly to the surgical tip of the device, where vibration of the tip is the mechanism through which fragmentation occurs. Multiple tips

are available for various applications. Irrigation fluid flows down around the transducer tip, providing both cooling to the tip and a constant flow of fluid to remove fragmented tissue. [51]

The two frequencies of CUSA (23 and 36 kHz) offer differing levels of ablation, where the 23 kHz device is typically used for fragmenting tougher, fibrous, or calcified material, the 36 kHz handpiece is meant for precision operations requiring a more tactile approach. Adjustment of the tip oscillation amplitude provides additional levels of precision when attempting to avoid damage to surrounding tissue or vasculature.

In cancer treatments, typically, the CUSA is used for rapid debulking of tumors or separation of healthy tissue from cancerous. However, one of the CUSAs major benefits is also a limitation - rapid debulking means extra caution must be kept near, arteries and vasculature as the CUSA can easily damage these, and lacks the ability to then cauterize as it is or after cutting [52]. Due to this lack of specificity, tumors that have grown near to, or around, major blood vessels in the liver can make a tumor inoperable using the CUSA or mechanical resection alone[53]. Additionally, quoted from the work of Brotchi[54], "It must also be remembered that the CUSA does not distinguish between tumor and spinal cord, only the surgeon does." The CUSA, lacking any form of advanced imaging feedback, relies on the surgeon to visually distinguish healthy tissue from sick. Finally, the CUSA must sometimes cut through healthy tissue to get to cancerous tissue. In a liver, colon, or other more robust tissue

this may not be a problem, however, cutting into healthy brain tissue to reach a tumor can leave a patient with cognitive or physical deficits.

2.2 High-Intensity Focused Ultrasound (HIFU)

HIFU is a transdermal ablation technique delivering large amounts of acoustic energy to a focal point where the temperature increase due to acoustic absorption causes hyperthermic tissue necrosis. As shown in Figure 2.2, volumes are commonly ablated in two ways: a single, large HIFU transducer as shown in diagrams a and b can be translated leaving an array of tissue lesions, or using a phased array as seen in Figure 2.2c, made up of multiple smaller transducers, which can be phase delayed with respect to each other to steer the acoustic focus. In both cases, delivery of a thermal dose to a volume is measured in thermal isoeffect dose (TID).

TID is the time required to hold a volume at a fixed temperature to cause cell necrosis. TID is typically expressed in reference to 43 degrees Celsius which, clinically, is considered to have been a successful thermal ablation after 240 minutes, although this is tissue dependent and can reach as low as 20-30 minutes. For temperatures other than 43 degrees Celsius, the relationship

$$t_{43} = R^{T-43} \Delta t$$

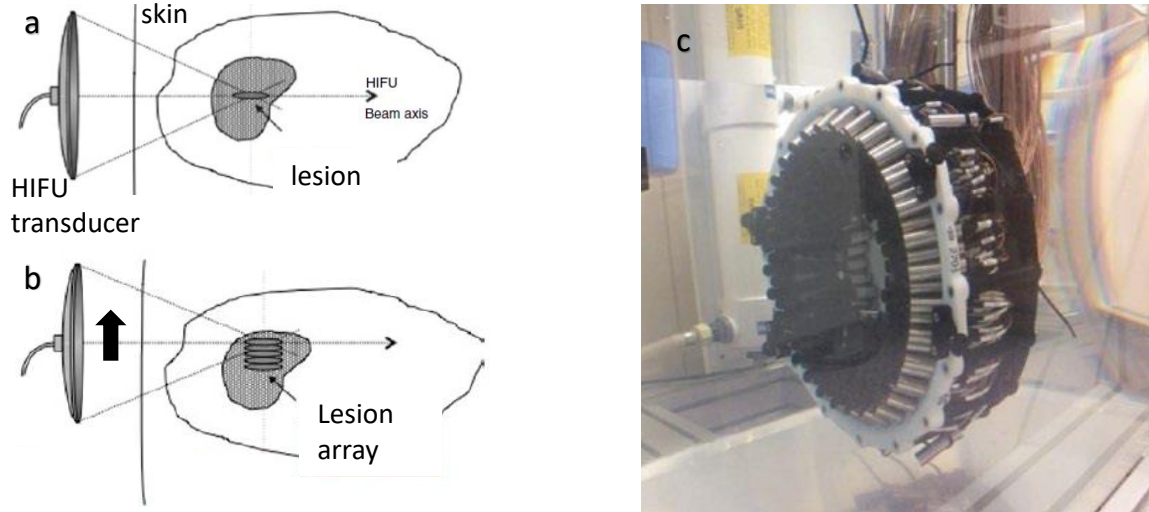


Figure 2.2: (a) To ablate a large area, HIFU devices can be translated to create a lesion of arrays or, (b) a phased array can be used to steer the beam to ablate while holding the transducer fixed in place. Images taken from the book *Therapeutic Ultrasound* [55]. See Appendix A for copyright.

where t_{43} is the TID value, R is a constant, $R = 2$, when temperatures are above 43 degrees Celsius and $4 \leq R \leq 6$ below 42 degrees Celsius, and Δt is the time over which the temperature is held at T [56]. At 50 degrees Celsius, for example, to achieve a TID of 240, the equivalent time is 1 minutes, 52 seconds. For tissues elevated to 60 degrees Celsius, less than one (1) second will generally lead to cell death [11]. The TID for Chinese hamster ovary cells over a range of temperatures was reported in a publication by Dewey [56], where it was shown that even for the small temperature difference from 42 to 44 degrees Celsius cell survival rates can range from a 90% survival rate to less than 1% at a 50 minute exposure.

The wide range of cell survival rates in such a small temperature range illustrates how important temperature monitoring of HIFU treatments is, especially in regions

like the brain where collateral damage could lead to significant neurological or motor deficits, and insufficient ablation could lead to relapse. Additionally, avoiding overheating which is commonly associated with cavitation or boiling is important since these events can be unpredictable if not controlled, and relatively large gas volumes generated through boiling could act to shadow deeper regions from thermal treatment. Areas near to large blood vessels have also been shown to be more difficult to treat with HIFU, due to the heatsink effect of flowing blood in the vessel itself [57, 58] suggesting it is more difficult to reach the desired TID, although, for short high-energy treatments the heatsink effect is minimal [59]. For smaller vessels, research shows HIFU treatments can damage vessels less than 2 mm in diameter [60] and, in fact, Ichihara *et. al.* purposefully used HIFU to induce arterial occlusion in a rabbit model [61].

Location of ablation can be of concern near organ walls where there is potential for collateral damage to adjacent organs when treating tumor sites on the organ periphery [62], or unintended damage to the targeted organ from reflections if treating adjacent to a strong reflector. It is also of note that liver and spleen treatments are sometimes limited due to the rib-cage blocking HIFU, causing rib heating, although this can be solved by avoiding the rib using a phased array transducer and disabling elements with direct line-of-sight between transducer and tumor. When the targeted treatment is within the skull there is unfortunately no way to non-invasively avoid treating through

bone without removing it.

HIFU treatments for GBM were successfully performed through a craniectomy hole as early as 2006 [63], but, it was not until 2014 that transcranial HIFU treatment on a centrally located glioblastoma was first successfully reported [64] using the Insightec ExAblate Neuro, a commercially available system. Prior to this an attempt was made [65] using an earlier model system (Insightec ExAblate 3000) which was incapable of reaching temperature above 55 degrees Celsius, the temperature reportedly required to cause coagulation necrosis [66]. Coagulation necrosis may be preferred as the necrotised tissue remains solid and typically well targeted, whereas below 55 degrees Celsius cells may be more apoptotic, where cells continue to be liquid filled membranes, possibly leading to misshapen ablation sites and cavitation events[67]. Additionally, margins may be larger with lower temperature HIFU as the effects of apoptotic cell death may be delayed[68]. The authors in both transcranial treatment papers admit that glioblastoma multiform is not the ideal candidate for transcranial MRgHIFU due to the dendritic nature of the tumor, and suggest their treatments would be better suited to inoperable metastatic tumors or other tumors with well-defined margins, or benign tumors. They were also limited to centrally located tumors due to the skull limiting the ability to focus peripherally.

2.3 Histotripsy and Boiling Histotripsy

Both histotripsy and boiling histotripsy are mechanical ablation methods with the mechanism of ablation initialization being different for each. Figure 2.3 shows how the pulse sequences for regular and boiling histotripsy differ. Histotripsy (non-boiling) has two methods of action: intrinsic threshold and shock-scatter histotripsy. Intrinsic threshold histotripsy relies on the peak-negative pressure (labelled p_- in Figure 2.3A) generated by the transducer going below the pressure threshold (intrinsic threshold) required in the specific medium or tissue to cause a cavitation event. The number of ultrasound cycles in a pulse is only one or two, lasting in the range of microseconds as is shown in Figure 2.3B, and the pulses are spaced milliseconds up to seconds apart for generation of cavitation. The pressure thresholds that need to be reached vary between tissue types and differ based on pulse rate[69]. At a 1000 Hz histotripsy pulse rate, for example, the intrinsic threshold range is from 13 MPa in fatty tissue to up to 27 MPa in cartilage and has some correlation to the tissue stiffness. Shock-scatter histotripsy, instead of relying on the ultrasound waveform pressure going below the intrinsic threshold in one or two cycles directly, requires that the waveform reflects off of entrained gas bubbles, inverting pressure amplitude in the process, and then constructively interfering with incoming waves to pass the intrinsic threshold. A schematic of shock scatter histotripsy is shown in Figure 2.4.

In Figure 2.4a a shock front is approaching a gas bubble (top) and the pressure is plotted on the bottom. As the shock front passes the bubble in (b), the bubble oscillates in size and the shockwave reflects backward, inverting in amplitude, which is seen in the pressure plot where a strong negative pressure spike appears. This negative pressure spike now passes the intrinsic threshold for water and, in Figure 2.4c, we can see initial bubbles forming in the upper image. This process is now sustained so long as shock waves continue to impinge on the bubble cloud, reflecting and generating new bubbles.

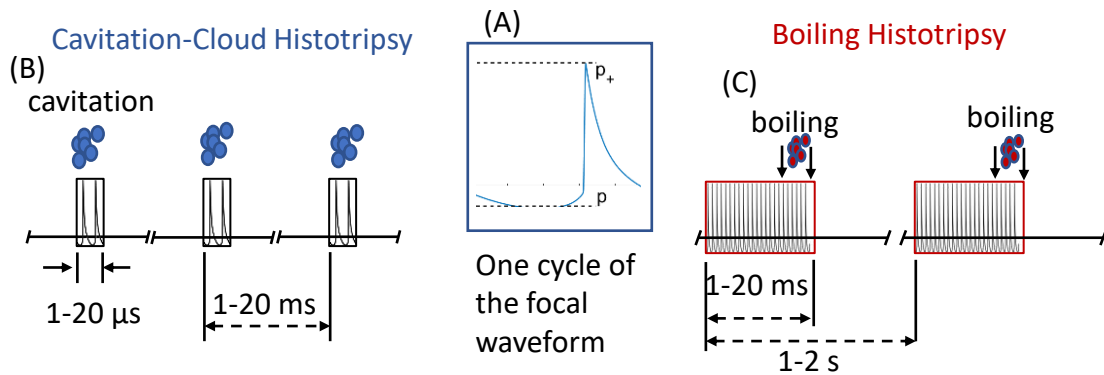


Figure 2.3: (A) A typical asymmetric waveform due to strong nonlinear acoustic behaviour (B) For cavitation cloud histotripsy (intrinsic threshold) one or two cycles reach sufficient negative pressure to cause cavitation (C) Boiling histotripsy uses less intense non-linear pulses over a longer period, relying on rapid heating to quickly boil and cause cavitation. Figure reproduced based on work by Khoklova *et. al.* [37].

To perform shock-scatter histotripsy, multiple cycles of ultrasound are used (usually between 2 and 10), as the first few cycles will help release and expand entrained gas bubbles in the medium, resulting in larger reflectors that the following cycles can interact with and reflect from, inverting their pressure amplitude and reaching

the intrinsic threshold. Shock scatter histotripsy can be achieved when a device is capable of generating positive pressures greater than the magnitude of the intrinsic threshold but negative pressures which do not reach the intrinsic level.

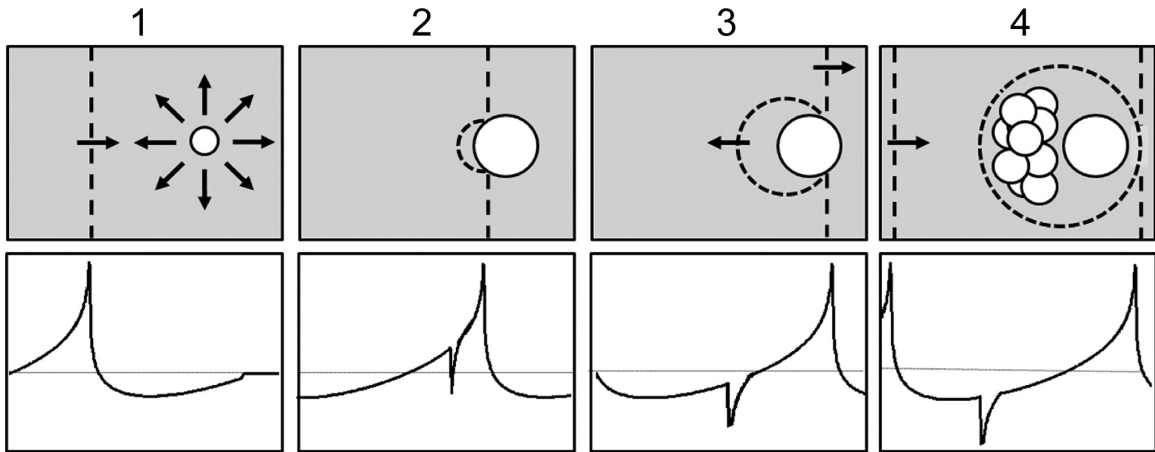


Figure 2.4: A shock front impinges on a gas bubble (1), reflecting and inverting the pressure waveform (2 and 3) which leads to the inverted pressure passing the intrinsic threshold and generating multiple smaller cavitation events (4). Used with permission from [71]. See Appendix A for Copyright.

Boiling histotripsy, at the beginning, looks very much like HIFU. A long train of ultrasonic pulses, seen in Figure 2.3C are delivered to a focal point, raising the temperature. However, the pulse train becomes strongly nonlinear at the center of the focal zone leading to rapid heating and boiling. This process, shown in Figure 2.5, generates a vapor cavity as the focal center raises temperature above 100 degrees Celsius. Once a cavity is formed, it rapidly expands and subsequent ultrasound cycles strike it, causing an acoustic-microfountain within the cavity which mechanically fractionates the tissue surrounding the cavity before it collapses. The idea is that the insonification time period is short, on the order of milliseconds, and the fractionation

occurs much faster than local heating effects can damage the tissue, while additionally the fractionation encompasses a volume greater than that where thermal damage may have started.

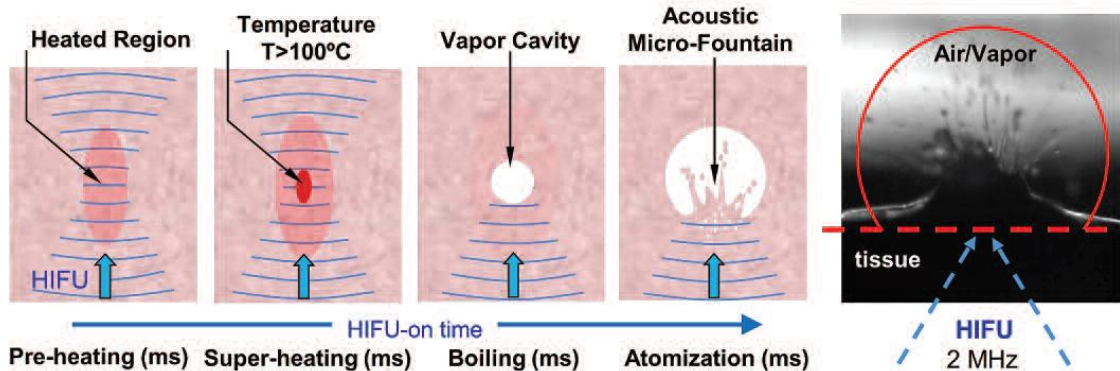


Figure 2.5: Focused ultrasound heats a region of tissue, and at the focal center, nonlinear heating leads to rapid temperature increase and a vapor cavity forming at boiling. This vapor cavity expands, providing a reflector for follow-up acoustic waves to generate an acoustic fountain effect, leading to mechanical ablation of tissue in and around the vapor cavity. [38]. See Appendix A for Copyright Permission.

The controllability of intrinsic threshold histotripsy ablation volume is high, as the ablated volume is limited to where pressure is increased above the intrinsic threshold only, with zero cavitation in the surrounding area. A single pulse is not sufficient to ablate an entire volume, however, so some amount of dwell time is necessary to induce multiple cavitation events to fully ablate the volume[70].

Figure 2.6g-l shows the size of an intrinsic threshold ablation slice as pressure increases. The cavitation events are limited to the volume above the intrinsic threshold. Shock-scatter histotripsy ablation volume still depends on pressure amplitude, however, the extent of the volume is strongly affected by the number of ultrasound

cycles used per pulse [71] as demonstrated in the high-speed camera images presented in Figures 2.6a-e. Figure 2.6a shows the multi-cycle pressure wave progressing with a number of small bubbles visible, but no cloud initiation. The image in Figure 2.6b captures bubble cloud initiation, where a reflected wave reached intrinsic levels, and additional cycles impinging on the cloud successively extend the length of the cloud in images c and d, with the final cloud shown in Figure 2.6e. Each additional cycle grows the cavitation region further toward the ultrasound transducer until, eventually, the cloud itself self-terminates as it blocks further acoustic energy from reaching the initial cavitation events, limiting the maximum extent of the ablation volume.

Both histotripsy and boiling histotripsy have been shown to cause reduced damage to vasculature as the vessel size increases [42, 34], typically destroying vessels measuring below $100\ \mu\text{m}$ and causing no measurable damage to vessels above $300\ \mu\text{m}$. Additionally, non-boiling histotripsy requires no heating to initiate and is therefore relatively immune to heatsink effects of the local environment. It is unclear if boiling histotripsy, which relies on initial tissue heating, is affected by local heatsinking. All forms of histotripsy are visible on standard ultrasound imaging, as the cavitation events are highly echogenic, so once cavitation begins the targetability is high. However, it is not always possible to perfectly predict the initial location of ablation until cavitation is initiated, especially deep in tissue where layers of fat and bone may change the focus and reduce focal pressure[42].

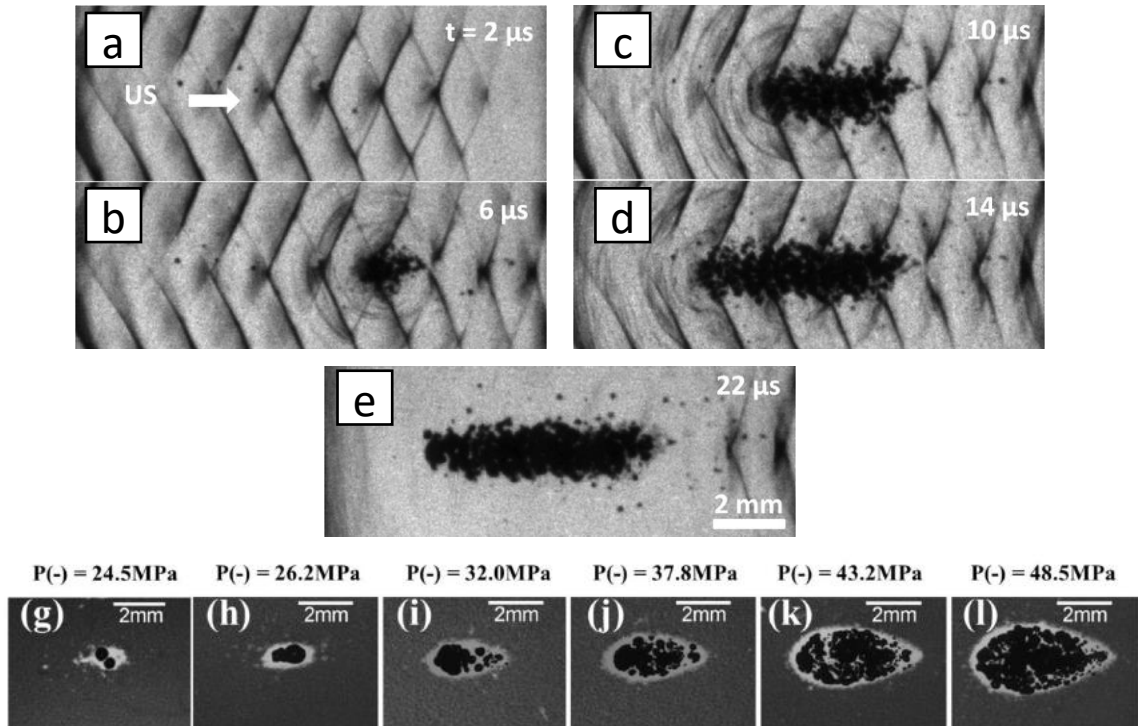


Figure 2.6: (a-e) The progression of cavitation events due to shock-scattering is shown, where cycles impinging on a previous bubble cloud add to the growth. (g-l) As pressure increases, the volume of cavitation events also increases, but is strictly limited to the volume above the intrinsic threshold. [71, 70]. See Appendix A for Copyright Permission.

It should be noted that, for cavitation histotripsy, it is well documented that the cavitation threshold varies based on tissue type and seems to be correlated with stiffness, leading to difficulties in ablating tendon and cartilaginous tissues[69]. It is unclear if this same limitation exists for boiling histotripsy, given the cloud initialization mechanism is not the same. Both forms of histotripsy are limited near tissue such as lung or bowel, as these contain gas-filled cavities and are difficult to either target, or maintain a predictable ultrasound field.

2.4 Microbubbles: Therapeutic Delivery and Ablation Assistance

Microbubbles and their uses warrant discussion as they are currently an active area of study for treatment of brain tumors. Microbubbles themselves are either a lipid, or protein based shells measuring one to seven micrometers in diameter surrounding a gas. The gas is typically fluorine-based to remain inert and relatively water insoluble[72]. Often used to enhance ultrasound imaging or improve resolution, in relation to cancer treatments, however, microbubble oscillation has been found to improve vascular permeability and improve extravasation of cancer therapies[55].

In the brain, the method of action is thought to be the disruption of endothelial tight junctions in microvasculature[73, 46], increasing vesicular transport, as well as alteration of endothelial cell membrane proteins[74]. Microbubbles in the brain are insonified to reach oscillation without destruction, a regime called stable cavitation. Bubble destruction is avoided as it is more likely to lead to endothelial cell damage and extended, or potentially permanent blood-brain barrier opening. A diagram outlining the opening of the blood-brain barrier is shown in Figure 2.7, where microbubbles roughly the size of the vasculature are insonified, expanding and contracting the vessel wall and allowing smaller molecules access to the extravasal space. The blood brain barrier remains open on the order of hours, depending on the vessel size, level of insonification, and microbubble size used.

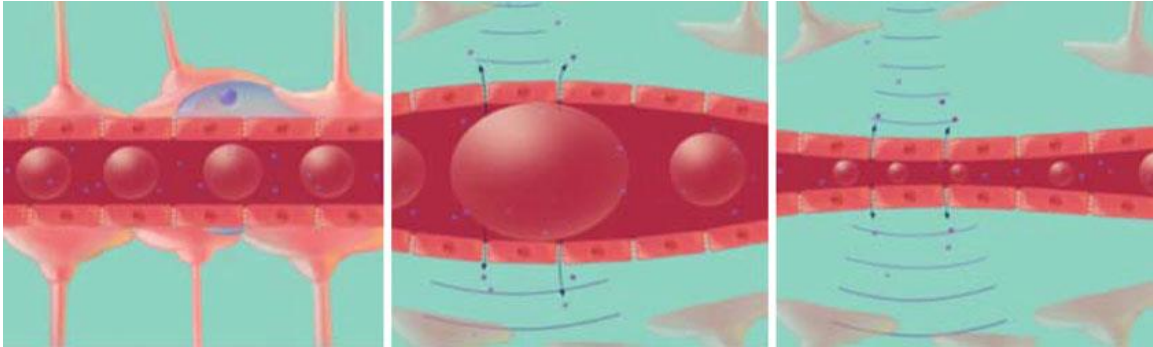


Figure 2.7: As microbubbles pass through comparable sized vasculature, ultrasound insonification causes them to expand and contract, separating cells and opening the tight junctions between them. Used with permission from [55]. See Appendix A for Copyright.

The pressure window to maintain bubbles in the stable cavitation regime is small, where, Choi *et. al.*[75] reported for a range of custom microbubble sizes from 1- $5\mu\text{m}$, a pressure of 0.15 MPa was insufficient to open the blood-brain barrier, while pressures of 0.45 MPa and 0.61 MPa were shown to clearly open the blood-brain barrier. Higher pressures were avoided as to not destroy microbubbles. Monitoring of acoustic feedback from the oscillating microbubbles allows detecting of cavitation levels, which can ensure bubbles remain in the stable state[76].

Outside of the brain, it is less important to maintain a stable cavitation state and, in fact, many treatments involve destruction of the microbubbles to open tissue access to the blood supply, allowing entry of therapeutics. Although the method of action is not entirely clear, it is expected to be a combination of sonoporation, puncturing of the cell wall during bubble collapse, and stretching/collapsing of the tight junctions during bubble oscillation. Figure 2.8 shows the introduction of microbubbles, either

co-injected with a drug, combined with a drug, or modified to target and bind to specific sites in the body, injected into the blood. The first two images of a bubble growing and shrinking show separation of the tight junctions, similar to that seen in BBB opening. The third image, involving liquid jetting, directly damages cells. The targeted microbubbles are of particular interest as some have been modified to bind to targets in rapidly vascularizing tissue, which is common for tumors, such as VEGF receptors and integrins and have been successfully tested for binding in animal tumor models (breast, pancreatic, glioma, and ovarian tumors) as well as successful targeting in some clinical trials for prostate, ovarian and breast cancer[77].

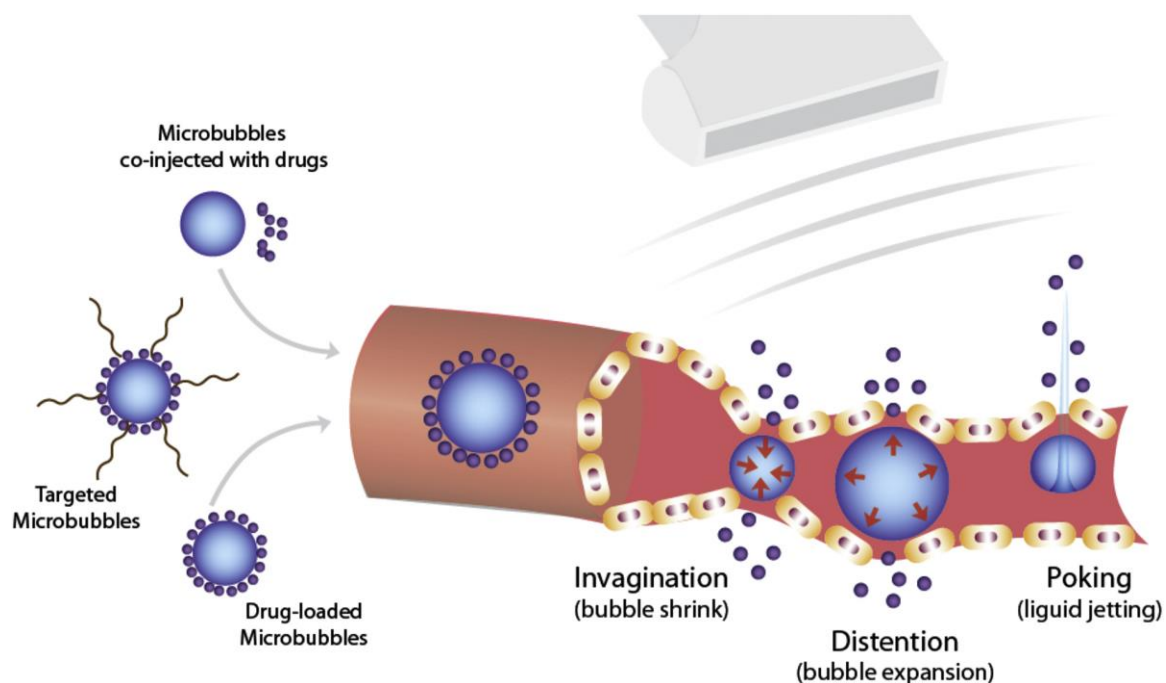


Figure 2.8: Microbubbles can be co-injected with a therapeutic, or the therapeutic can be part of the bubble shell. When injected and insonified, the bubble can allow the drug to pass between the endothelial cells, or liquid jetting upon bubble collapse can break through endothelial cells, allowing the therapeutic (and blood) to enter the extravascular space. Used with permission from [78]. See Appendix A for Copyright.

A summary of microbubble treatments in combination with drug delivery of various murine tumors (brain, liver, breast, pancreatic and melanoma) is provided by Chowdhury *et. al.*[78] where researchers report effects including tumor growth suppression, tumor shrinkage, drug delivery efficacy increasing by two-fold to twelve-fold, and reduced drug accumulation in non-targeted tissue.

Histotripsy Small Animal Models: Mouse and Rat

The mouse model is the most widely used organism for studying disease in humans [79]; however, when it comes to histotripsy there are relatively few rodent studies. Hoogenboom *et. al.*[40] in 2017 performed 3 MHz ablation boiling histotripsy studies on hepatic tissue in a mouse model which resulted in 1.8 mm to 7.5 mm longitudinal length lesions, where lesion size varied based on the type of tumor treated. Vlasisavljevich *et. al.* [80] performed murine hepatic tissue ablation in 2016 using histotripsy at 1 MHz, where a 4 mm by 4 mm grid was ablated with a spacing of 0.5 mm between treatments in the grid. Using the Eker rat model, Schade *et. al.* [41] in 2019 used a 1.5 MHz transducer with a -6 dB level of 7.5 mm by 0.8 mm by 0.8 mm to remove a renal tumor with boiling histotripsy. A longitudinal survival study treating murine hepatic carcinoma by Worlikar *et. al.* in 2020 [81] found full ablation of tumors using a 1 MHz small-animal histotripsy transducer had no recurrence (n = 9) and five out of six cohorts with a partial ablation had no recurrence. Qu *et. al.* [82],

using the same transducer as Worlikar *et. al.*, also in 2020, found mice inoculated in the flank with melanoma or hepatocellular carcinoma showed a drastically increased immune response when the tumor was partially ablated with histotripsy compared to radio-frequency ablation or sham therapies.

At present, the above relatively new studies comprise the bulk of mouse and rat model histotripsy treatments published, and this could be due to the large focal size of current transducers. In a mouse model, for example, the liver is the largest organ by mass, and second only to the lungs in volume [83] where a comparison of organ sizes can be seen in Table 2.1.

Table 2.1: A table of mouse organ sizes shows that the liver is one of the largest, second to only the lungs, where most organs, except for the bowel, are less than half the size of the liver

<i>Organ</i>	<i>Density (g/cm³)</i>	<i>Length (cm)</i>	<i>Width (cm)</i>	<i>Height (cm)</i>	<i>Mass (g)</i>
Liver	1.00	1.54	1.13	0.86	1.050
Spleen	1.00	1.67	0.57	0.20	0.090
Kidneys	1.00	0.83	0.56	0.50	0.265
Lungs	0.26	1.57	1.28	1.22	0.150
Heart	1.00	0.85	0.55	0.50	0.115
Stomach	1.00	1.37	0.91	0.69	0.175
Small bowel	1.00	1.20	1.20	1.00	0.878
Large bowel	1.00	1.50	1.60	0.50	0.332
Thyroid	1.00	0.71	0.57	0.10	0.105
Tumor	1.00	0.36	0.36	0.36	0.024
Pancreas	1.00	0.55	0.32	0.20	0.105
Bone	1.92	1.30	0.20	0.20	0.110
Marrow	1.03	0.90	0.10	0.10	0.009
Carcass	1.00	7.50	2.50	2.50	21.592

Note that the pancreas is one tenth the size of the liver, as is the thyroid and the heart, so given that the -6dB focal size of the 1.5 MHz transducer used by Schade is larger than most of these organs, it might be difficult to ablate small volumes of

them successfully. For this reason, a higher frequency transducer could be used to obtain a tighter focus and therefore improved targetability in smaller organs. We can approximate the lateral resolution of concave focused transducers using the following equation:

$$R_{\text{lat}} = 1.22\lambda \frac{a}{D} = 1.22 \frac{c}{f} \frac{a}{D} \quad (2.1)$$

where λ is the wavelength, c is the wave propagation speed in the medium, f is frequency, and a and D are dimensional quantities of the lens. The lateral resolution is inversely proportional to frequency, so a tighter focus can be achieved by increasing frequency. For the axial resolution,

$$R_{\text{axial}} = 7.2\lambda \left(\frac{a}{D}\right)^2 = 7.2 \frac{c}{f} \left(\frac{a}{D}\right)^2 \quad (2.2)$$

so, similarly, increasing frequency will result in a tighter axial focus.

Immunotherapy Tumor Treatment in Mouse Model

In 2018, Chavez *et. al.* [84] published a paper on the use of immunotherapy (check-point inhibitors) in combination with ultrasound thermal ablation (magneto-resonance guided HIFU). It was found that the combination treatment could reduce the size of implanted tumors, not only at the target ablation site but also at remote tumor sites.

In 2019, Eranki *et. al.* [85] published a similar paper with results showing, again, focused ultrasound (histotripsy) was used to treat small tumor areas of a refractory murine neuroblastoma in combination with two checkpoint inhibitors and found that the 300-day mouse survival rate went from less than 10% under immunotherapy only, to 62% in the combination therapy. Note, that the survival rate of mice without treatment, with histotripsy only, or with either immunotherapy on their own was 0% after 32 days.

The fact that immunologically “cold” tumors in untreated areas also reduce in size suggests that something about the focused ultrasound treatment primes the immune system to then attack all tumor cells of the type treated, especially when used in conjunction with immunotherapy. This response is not dissimilar to the response when treating a tumor with radiation therapy in conjunction with immunotherapy, however, it is possible that histotripsy activates the immune system differently as it mechanically fractionates cells instead of causing them to go through coagulative necrosis, potentially affecting the tumor antigens. With this in mind, a logical step for researchers is to perform immunoassays on histotripsy treated cancer cells of multiple tumor types to better determine what effect histotripsy has on the cells compared to HIFU or radiation therapy, and what specific immunotherapy may maximize the tumor suppressing effect. To perform these kinds of studies, a small animal histotripsy device accessible to all researchers would be ideal.

2.4.1 Discussion on the State of Therapeutic Ultrasound in Tumor

Ablation

In primary tumors (tumors in the tissue in which they initially formed), if the tumor is localized, non-metastatic, and the patient is otherwise healthy, surgical resection provides the best chance for complete tumor removal. A big part of this is the ability to test tumor margins for remaining cancerous cells. Surgeons can debulk a tumor, remove material in a safe margin around the tumor, and then biopsy tissue to be sent to the pathology department for confirmation of healthy or cancerous tissue, in some cases, prior to the patient leaving surgery. This ability to test surroundings is especially important in the brain where chemotherapy is less effective and thus remnants are difficult to treat, which would lead to a relapse. According to recent cancer treatment and survivorship statistics [15], surgical resection without chemotherapy or radiation is the leading treatment for colon, rectal, lung, testicular, bladder, and uterine cancer at Stages 1 and 2. At stage 3, surgical intervention combined with radiation or chemotherapy becomes the leading treatment, although overall surgical interventions do decline at this stage, likely because they are less effective after tumors have metastasized to other areas of the body. In these statistics, chemotherapy includes targeted therapies and gene therapies. Note, that one of the key requirements of the CUSA is tumor access. Tumors deep within the brain, for example, are considered inoperable with the CUSA, as are tumors which border on difficult to repair

vasculature, key functional areas of tissue, or cases where there are multiple cancerous growths throughout an organ (typical of liver cancer as it is rarely discovered early). Additionally, for older patients, or patients who are at high risk of complications in surgery, CUSA usage is less than optimal, which is where transcutaneous options such as HIFU or histotripsy become more appealing.

Transcutaneous treatments require wider margins than surgical resection as it can be difficult to determine where tumor ends and healthy tissue begins. Needle biopsy can help determine the need for additional treatments. In general, however, both histotripsy and HIFU share a number of overlapping applications (liver, spleen, prostate), but, given HIFU has had an almost 20 year head-start it has been more thoroughly explored for many treatment cases, while histotripsy still has to be proven for a wide range of use cases. Often the choice of which treatment to use may come down to location within the organ itself. Histotripsy, with the precision that intrinsic threshold can target, may be the most useful on organ periphery to avoid collateral damage, or in areas near large vasculature which will remain undamaged while essentially 'scraping' the walls clear of cancer cells. The ability of histotripsy to adjust the ablation size based on pressure thresholds and visualize the ablation zone may make it especially appealing for smaller and more precise work, in organs such as the pancreas or in small-animal work. HIFU could be of benefit in areas where the best treatment option is to simply block blood flow to the cancer site, as HIFU

has been shown capable of stopping flow in smaller vasculature, whereas histotripsy would either destroy the vasculature, or leave it fully functional.

There may be benefit in using histotripsy in more palliative capacities, where tumors are pressing on nerves, bones, or organs causing pain. In a canine model, histotripsy was able to debulk prostate tissue and create a drain to the urethra for immediate debulking of the prostate [86] which could reduce pressure on surroundings. In the liver, ablated volumes were shown to be free of edema and granulation tissue (new connective tissue) within 14 days[80].

Shock-scatter histotripsy, and boiling histotripsy, are more difficult to qualify in terms of when to be used in tumor ablation. Although easier to initiate than intrinsic threshold histotripsy as they require less overall pressure, both rely on reflections from one or multiple vapor bubbles which make them reliant on this initial vaporization occurring and prone to back-reflections causing cavitation outside of the targeted volume. For boiling histotripsy, if a vapor cloud does not appear, you are instead left in the HIFU regime and may have inadvertently damaged a larger volume than desired. Additionally, it is possible to create a thermal lesion which partially shields the focal point from boiling, thus resulting in a lack of cavitation lesion[87]. The solution to this shielding lesion is to increase the pulse length of treatment to ensure boiling occurs, however, if boiling still does not occur this leaves a larger thermal lesion than anticipated. For shock-scatter histotripsy, if a bubble cloud does not

occur, then it is obvious that no ablation has occurred as it is an inherently low-power treatment and will not cause a thermal lesion. In both cases, damage can be minimized by increasing ultrasound frequency or focusing the transducer tighter, both of which shrink the ablation zone, however, this comes at the cost of treatable depth.

Microbubbles targeting tumors which are vascularizing seem to have their place already set in ultrasound-based therapies. There may be promise in using a combined approach, with targeted microbubbles delivering chemotherapy to tumor periphery while using HIFU or histotripsy to debulk the core. This may be a particularly attractive combination of therapies in the brain, where GBM tends to be dendritic, spreading in a way that makes identification, imaging and resection difficult.

It might be tempting to combine microbubble therapy with HIFU in areas where it is difficult to achieve sufficient TID values, as it has been shown that microbubbles can increase the efficacy of the HIFU treatment, however, care must be taken as to the microbubble injection site and location of bubbles during therapy as McDannold *et. al.*[88] have shown there can be collateral damage outside of the focus along the ultrasound beam path in continuous wave operations due to beam interactions with microbubbles. This may be especially problematic in the brain, compared to the liver which is more robust against damage. It is recommended that simply increasing acoustic power is the best way to reach TID if necessary, although this may lead to

superficial skin damage, or damage to any organs containing gas (bowel, lung) along the acoustic pathway.

2.4.2 Conclusion

The CUSA and HIFU are both well studied forms of ultrasound-based treatments. The use of HIFU is likely to grow further as more studies show its efficacy in cancer treatment, especially brain treatments, and as more devices reach market. For histotripsy, the field is still in its infancy and as the core groups who perform histotripsy grow and produce new researchers, the uses for histotripsy and histotripsy-based devices have the potential to grow exponentially. Since chemotherapy is used in almost every cancer treatment, microbubble assisted drug delivery also will likely grow in usage cases as well as it proves an effective method to improve drug uptake locally, avoiding toxicity to the rest of the body. Combining histotripsy with all of the above mentioned therapies remains open to researchers wishing to enter the field.

Chapter 3

Ultrasound Transducers

A transducer is a device which either converts a physical quantity (pressure, temperature, brightness, etc.) into a measurable electrical signal, or vice-versa, so an ultrasound transducer is a device that converts energy to and from the acoustic domain in the ultrasonic range (frequencies above the human audible spectrum, so roughly higher than 20 kHz). In the medical field, ultrasound transducers can typically be split into two categories: diagnostic ultrasound, and therapeutic ultrasound. When one thinks of diagnostic ultrasound they often imagine ultrasound images like those seen when examining a baby in-utero, however, diagnostic ultrasound imaging is used to perform an enormous number of tasks, such as imaging many soft tissues; e.g. heart, colon, bladder, and prostate, measuring blood flow via Doppler ultrasound, and measuring the elastic properties of soft tissue using elastography. Diagnostic ultrasound is considered a non-destructive imaging modality as it does not permanently change the tissues under scrutiny. Within the scope of this work, diagnostic ultrasound will be limited to imaging of soft tissue for ablation targeting.

For therapeutic ultrasound, ultrasound waves are directed to a specific area of the body and, unlike diagnostic ultrasound, the intention of therapeutic ultrasound is to effect the body in some way. Some examples of therapeutic ultrasound include: lithotripsy, the break-down of kidney stones; HIFU, tissue hyperthermia through ultrasound absorption [89]; targeted drug delivery, rupturing drug carrying microcapsules at a specific location; cosmetic ultrasound, involving wrinkle reduction and other skin treatments; and histotripsy, a non-thermal cavitation based tissue ablation technique [37].

Although there are a number of ways to generate acoustic waves in the ultrasonic frequency range, the most prevalent is by applying a voltage pulse, or an oscillating voltage signal at the frequency of interest to any material that exhibits the piezoelectric effect, converting the applied electrical signal directly into acoustic waves. Within the scope of this thesis work, the goal in developing a therapeutic device is to deliver a large amount of acoustic energy in a very short bursts to create cavitation events.

3.1 Piezoelectric Effect

The direct piezoelectric effect is key to the operation of most modern ultrasound devices, but first, it makes sense to discuss the inverse piezoelectric effect as it is the method used to generate ultrasound signals. In Figure 3.1, a piezoelectric material in

three states is shown where Figure 3.1a shows the material in equilibrium with zero charge build-up on the upper and lower surface.

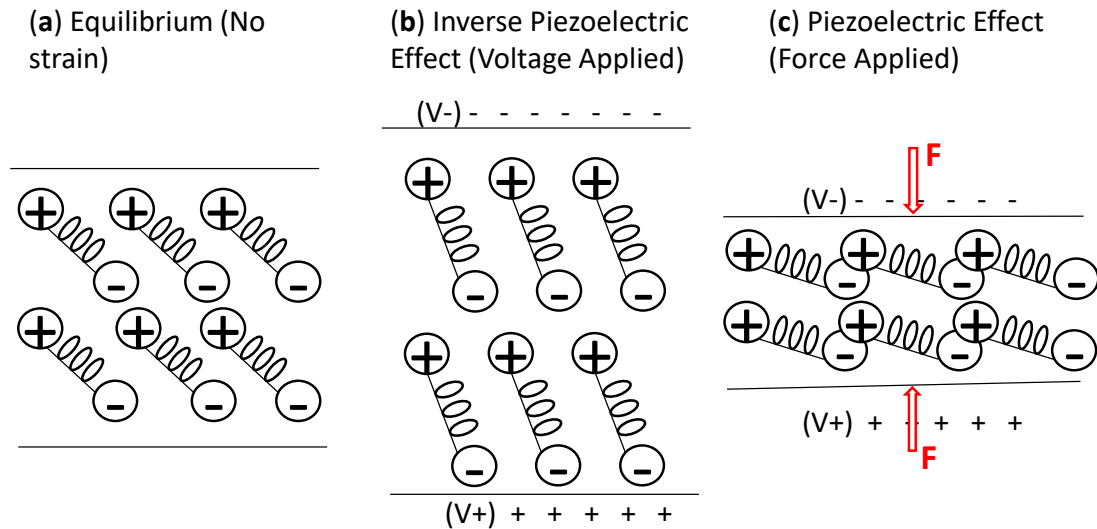


Figure 3.1: (a) A typical piezoelectric medium at rest under no force nor electric field (b) A piezoelectric strains with applied electric field (c) A piezoelectric generates electric field under applied force

Any material exhibiting the inverse piezoelectric effect will expand or contract under the application of an external electric field, where expansion or contraction is dependent on the polarity of the applied electric field. The key to this expansion and contraction is the existence of electrical dipoles tied to the mechanical structure of the piezoelectric material which, when a field is applied, try to orient themselves in the direction of the field, physically deforming the structure. In Figure 3.1b, we see that applying a negative charge to the upper boundary and, therefore, a positive net charge to the bottom boundary of the material results in the dipole rotating to align with these charges, expanding the material.

Conversely, the direct piezoelectric effect is a re-orientation of the dipoles in a piezoelectric through application of a force as shown in Figure 3.1c. The re-oriented dipoles create a net charge on opposite faces of the piezo which can then be measured as a voltage, thus allowing a way to generate an electrical signal from an input force. Since acoustic waves impinging on a surface generate a force, this provides a way to directly measure ultrasonic energy. So, combining both the inverse piezoelectric effect and the piezoelectric effect we have a way to both generate and measure ultrasonic waves.

Some dipoles, in many single-crystal materials for example, arise from the crystal structure being non-symmetric and are the size of the crystal unit cell, while for the more common piezoelectric materials the dipoles are made up of small micron sized clusters of material, sintered together into a ceramic. To take advantage of the inverse piezoelectric effect, one simply has to generate an electric field across the piezo material, which is typically done by depositing an electrode to each side of a piezoelectric and applying an electrical voltage, either constant or varying, to these electrodes. By definition, if a material exhibits the inverse piezoelectric effect, it must also exhibit the direct piezoelectric effect. The piezoelectric effect is the generation of charges on the surface of a piezoelectric material due to an applied force.

Mathematically, the direct piezoelectric effect and inverse piezoelectric effects can be described using the following two equations:

$$D = dT + \epsilon^T E \quad (3.1)$$

$$S = s^E T + dE \quad (3.2)$$

where the electrical variables D : the charge stored per unit area and E : the applied or induced electric field, are related to the mechanical variables, T : a measure of the tension or compression forces in the material, and S : the deformation of the material.

The first equation, 3.1, representing the direct piezoelectric effect, shows the dielectric displacement, D , is related to stress, T and the applied electric field, E through two intrinsic material constants, d : the ratio of stress to charge build-up as in Equation 3.1 or elongation to voltage, as in Equation 3.2, and ϵ : the ratio of applied electric field to charge build-up. The second equation, 3.2, representing the inverse piezoelectric effect, shows the strain, S , is related to stress, T through s : the ratio of the fractional deflection to force applied, and to the applied electric field through d . Note, the superscripts on ϵ and s denote that they are evaluated at constant (typically zero) values of T and E , respectively.

Mathematically, S , T , s and d are tensors, while E , D and ϵ are vectors; however, for present purposes it will be assumed all stress, strain, electric fields, and dielectric displacements occur in the poling direction, making modeling and design of

transducers a 1-dimensional (1D) problem.

A number of piezoelectric materials exist with properties which greatly vary based on the material composition, method of fabrication, and geometry. For a transducer that is intended to generate motion or ultrasound, a high value of d is desired [90].

3.2 Piezoelectric Materials

As mentioned in 3.1, a high value of d for a piezoelectric is desired in applications involving acoustic wave generation; however, there are a number of material properties which need to be considered when choosing a transducer material. One of the most important properties is the electromechanical coupling coefficient, k^2 .

This factor, k^2 , is a measure of how much of the electrical energy applied to a piezoelectric is converted into mechanical energy or, conversely, the amount of mechanical energy that is applied to a piezoelectric which can be converted into electrical energy. The more formal definitions for k^2 are:

$$k^2 = \frac{\text{electrical energy converted to mechanical energy}}{\text{input electrical energy}} \quad (3.3)$$

$$k^2 = \frac{\text{mechanical energy converted to electrical energy}}{\text{input mechanical energy}} \quad (3.4)$$

The remaining input energy which is not converted is simply stored either elastically (as in a spring) for the piezoelectric effect, or electrically (as in a capacitor) for the inverse piezoelectric effect. It should be noted that k^2 only defines the conversion efficiency between energy domains (electrical to mechanical). On its own, k^2 does not quantify the energy lost in either of the domains. Typically, a specification sheet provided by a piezoelectric supplier, for example CTS [91], will provide, along with k^2 , the Q and $\tan\delta_e$ which are metrics for the loss to heat in the mechanical and electrical domains respectively.

From a practical perspective, for a high transmit power device it is desired that a piezoelectric material have a high d , and high k^2 and low losses to avoid heating, so low Q and $\tan\delta_e$; however, as histotripsy is a high pulsed-power application, with low time-averaged power, the loss factors are less relevant as the device is not expected to dissipate enough power for a significant temperature increase. It should be noted that, although the definition of k^2 shows it to be related to energy domain conversions, a version of k^2 can also be expressed through resonance and anti-resonance frequencies of the transducer if measured un-loaded using,

$$k_t^2 = \frac{\pi\omega_s}{2\omega_p} \tan\left(\frac{\pi(\omega_p - \omega_s)}{2\omega_p}\right) \quad (3.5)$$

where the thickness mode mechanical resonance, or parallel resonance, is ω_p , the minimum electrical impedance point, or series resonance, is ω_s , and the transversely clamped electromechanical coupling factor k_t is used instead of k^2 when the acoustic element is laterally much larger than the acoustic wavelength, a common occurrence in ultrasound devices. The values of ω_p and ω_s can be measured using an electrical impedance analyzer attached to an unloaded piezoelectric material. Figure 3.2 provides a representative example of what a measured electrical impedance magnitude curve may look like and identifies the series resonance frequency occurring at the lowest impedance magnitude point, while the parallel resonance frequency occurs at the maximum impedance magnitude point. Note, these resonances are local occurrences and it is possible for both higher and lower impedance magnitude values to occur at much lower and higher frequencies. The peak impedance at ω_p is heavily affected by the damping of the piezo element.

The parallel resonance is also a calculable number defined as,

$$\omega_p = 2\pi f_p = \frac{\pi c_0}{l} \quad (3.6)$$

where the wave speed in the ceramic, c_0 , would be supplied by the material manufacturer, l is chosen based on the desired device frequency, and the f_p is another way of writing ω_p but measured in Hertz (Hz) instead of radians per second. With

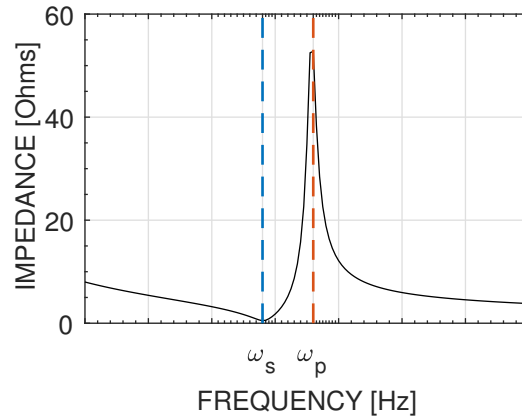


Figure 3.2: A representative electrical impedance magnitude measurement of a piezoelectric material is shown here to illustrate the series and parallel resonances where the series resonance, ω_s , is labeled and indicated by the blue dashed line, while the parallel resonance, ω_p , is labeled and indicated by the red dashed line.

the calculated value for ω_p and knowledge of k_t from a specification sheet the series resonance frequency ω_s can be calculated and this value is typically the operating frequency of the ultrasound device.

When comparing electromechanical coupling values, k_t is always lower than k^2 ; however k^2 does provide an upper theoretical limit to the value of k_t a piezoelectric element can have, and, if the transverse clamping of an element can be released interally, then k_t can be increased. To release the transverse clamping, a piezoelectric composite can be created. These composites not only benefit from higher k_t but, also a tuneable acoustic impedance which allows improved transfer of acoustic energy between media.

3.3 Piezoelectric-Polymer Composites

Much has been written on piezoelectric composites, with the works by Gururaja *et. al.* [92], Gururaja *et. al.* [93] and Smith and Auld [94] being some of the earliest and most comprehensive collection of piezoelectric composite fundamentals to date. A common composite type and the one used in this work is a 1-3 composite, the fabrication steps of which are shown in Figure 3.3 as a simplified schematic. The 1-3 designation of the composite provides the connectivity of the materials, in this case piezoelectric-epoxy (1-3). The connectivity of the piezoelectric material is one (1) as it only connects with itself vertically in one dimension, but not laterally. On the other hand, the epoxy connectivity of three (3) is due to the epoxy being fully connected to itself in three directions, one vertical and two lateral.

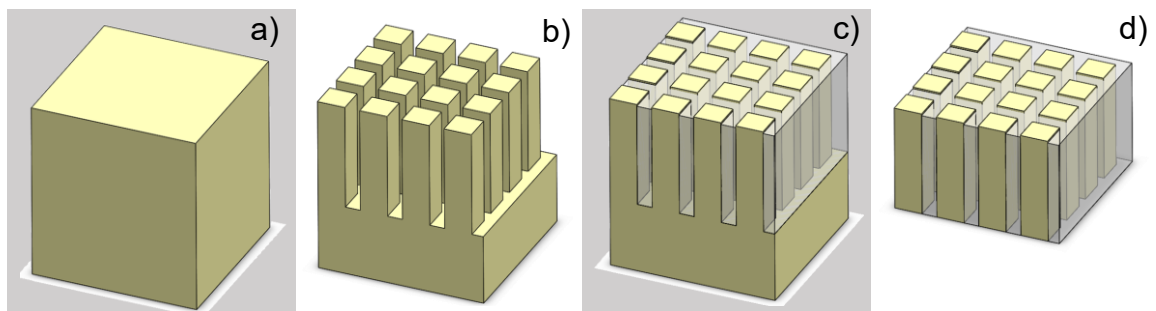


Figure 3.3: a) A 1-3 piezoelectric-epoxy composite starts with a solid piece of piezoelectric material. b) After two sets of perpendicular cuts are made, a matrix of pillars is left with a solid piezoelectric base. c) The space between pillars is filled with epoxy which can be sanded, machined, or lapped down to the top surface of the pillars. d) The solid base is removed through lapping or grinding, leaving a matrix of pillars embedded in epoxy.

The simplest fabrication method for a 1-3 composite starts with a solid piece of

piezoelectric (Figure 3.3a) which is cut through using a dicing saw, or other method for ceramic material removal at multiple parallel and orthogonal lines in the material called kerfs (Figure 3.3b). The cuts are often, but not necessarily, evenly spaced. The depth of cut for these kerfs depends on the desired operating frequency of the composite and is chosen to be deeper than the designed final thickness of the composite. This extra depth of cut allows for variation in the material removal process and avoids rounding of the pillars at the kerf bottoms due to blade taper. Once cut, the kerfs are filled with epoxy which is lapped or ground to the top of the pillars (Figure 3.3c) and then the remaining bulk piezo is removed leaving a matrix of pillars embedded in an epoxy matrix as seen in Figure 3.3d. An electrode can be applied to both faces of the composite after step (d), or one face can have the electrode applied after step (c), and then the other face after step (d).

By carefully choosing the spacing and size of the kerfs, the composite designer changes the volume of material that is ceramic and the volume that is epoxy which allows one to tune the speed of sound, acoustic impedance, and k_t . Note, the kerf spacing and size must be chosen to avoid shear waves and lateral modes in the composite periodic structure which could couple into the thickness-mode vibration, reducing the overall acoustic output[92]. The composite volume fraction is typically reported as the amount of ceramic, in either percent or amount by volume scaled between 0 to 1, in the composite and, in Figure 3.4, the effect a changing volume fraction can

have on the composite coupling coefficient, \bar{k}_t , the composite speed of sound, \bar{c}_0 , and the composite acoustic impedance \bar{Z} is illustrated using calculations with the ceramic PZT-5H and Spurr epoxy fill using properties listed in the work by Smith and Auld [94]. The acoustic impedance is also calculable using,

$$\bar{Z} = \bar{\rho}\bar{c} \quad (3.7)$$

with $\bar{\rho}$ being the composite density, a linear combination of the epoxy and piezo densities based on volume fraction, and \bar{c} being the composite speed of sound, a quantity measurable on the impedance analyzer using Equation 3.6 but practically difficult to calculate as many epoxy properties are unreported.

The large plateau in \bar{k}_t allows composites to have a wide volume fraction range with relatively efficient energy transfer and the value of \bar{Z} can be tuned for almost any value between that of the epoxy and ceramic, however, missing from this explanation is the electrical impedance. Figure 3.2 provided an example electrical impedance measurement for a transducer with the minimum impedance occurring at ω_s . Under air-backed and front-matched (matching covered in Subsection 3.4) conditions, the electrical impedance magnitude at frequency ω_s is a calculable number by using a

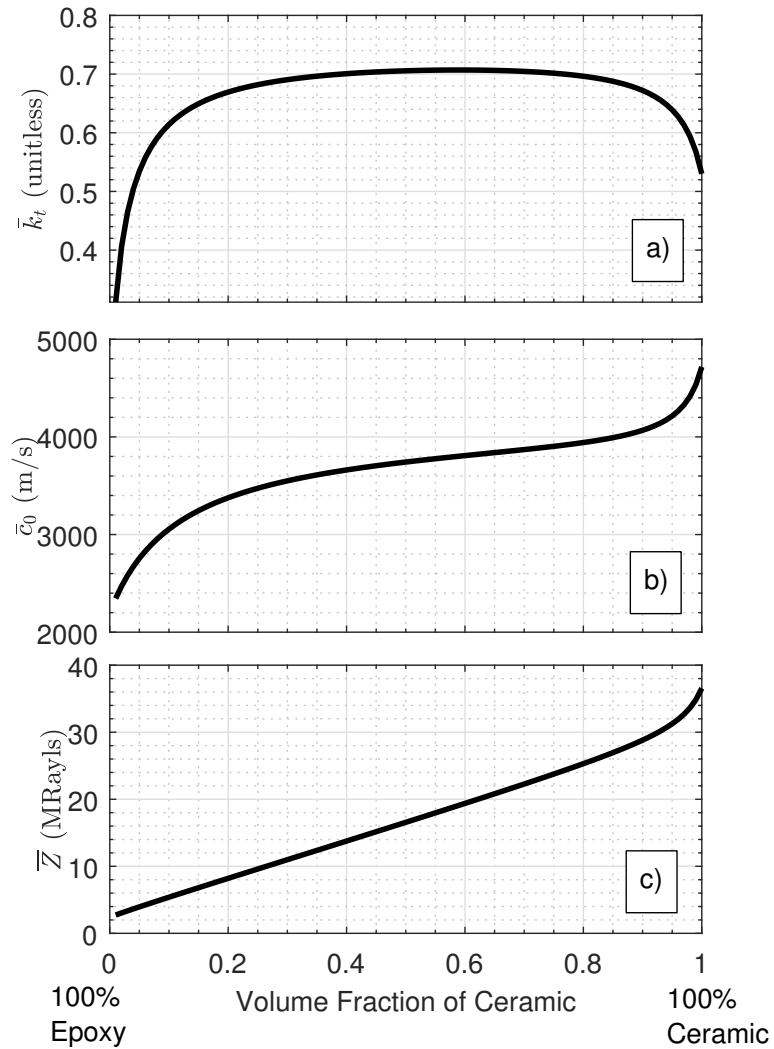


Figure 3.4: For PZT-5H and Spurr Epoxy, a) the value of \bar{k}_t plateaus and stays above k_t for the solid ceramic above volume fractions of 5%. b) The speed of sound for the composite varies non-linearly between the value for the epoxy alone and the value for the ceramic alone. c) The acoustic impedance, \bar{Z} , increases linearly from the value for Spurr epoxy at 0% volume fraction to 90% where the slope changes to reach a final value of 36.5 MRayl.

resistive load of electrical resistance,

$$R_{f0} = \frac{2(k_t)^2}{\pi^2 f_0 C_0} \quad (3.8)$$

called the radiation resistance, placed in series with a capacitor of capacitance value C_0 , known as the clamped capacitance. The clamped capacitance is calculated by,

$$C_0 = A\bar{\epsilon}^S/l \quad (3.9)$$

with A being the composite surface area, $\bar{\epsilon}^S$ being the clamped dielectric constant of the composite, and l being the composite thickness. For both the series resistance R_{f0} and the capacitor value, the electrical impedance is proportional to the inverse of C_0 . The value of $\bar{\epsilon}^S$ increases linearly with volume fraction from approximately 0 to the value ϵ_S of the ceramic in use, resulting in an increasing C_0 and, thus, a decreasing electrical impedance with volume fraction. All things being equal, the ratio of pressure generated by two devices at equivalent voltage drive level and frequency should be proportional to the square-root of the ratio of their impedance magnitudes at that drive frequency, meaning a higher C_0 results in a higher focal pressure. Of course, not all things are equal and the value of \bar{k}_t as well as the ability to electrically match cabling and acoustically match to a given medium need to be considered; nevertheless,

the idea that a higher clamped capacitance device should draw more electrical power and, thus, generate higher pressure has led to the choice of soft ceramics in this work, especially given the reduction in C_0 when making a composite. Additionally, the choice to try to maintain a high \bar{k}_t while also having an acoustic impedance which will allow for impedance match to either a focusing lens or a matching layer is important.

3.4 Acoustic Matching Layers

Acoustic matching layers allow transmission of acoustic energy between media without a significant loss of intensity. For acoustic waves at normal incidence to a surface between two media, the transmitted acoustic energy is governed by material acoustic impedances where,

$$T_I = \frac{Z_i Z_f}{(Z_i + Z_f)^2} \quad (3.10)$$

T_I is the transmission coefficient defined as the fraction of transmitted acoustic energy to the final medium, Z_i is the acoustic impedance of the initial medium, and Z_f is the acoustic impedance of the final medium. So, for two contacting media the transmitted energy is maximized if they are the same medium, and otherwise drops as the media impedances vary from each other. To combat this loss of intensity a matching layer, a

relatively thin layer of material, is placed between the initial and final media as shown in Figure 3.5, where the intensity transmission between media i and f is governed by the equation,

$$T_I = \frac{4Z_i Z_f}{(Z_i + Z_f)^2 \cos^2(\theta) + (Z_m + Z_i Z_f / Z_m)^2 \sin^2(\theta)} \quad (3.11)$$

$$\theta = \frac{2\pi l}{\lambda} \quad (3.12)$$

Z_m is the matching layer acoustic impedance, l the matching layer thickness, and λ is the wavelength which is being matched. Note, the inclusion of λ in Equation 3.11 means that a single matching layer cannot work for all frequencies of ultrasound. To demonstrate how the transmission coefficient between the initial and final medium is affected by the matching layer thickness and acoustic impedance, Figure 3.6 provides a number of curves of T_I versus wavelength fractional thickness of the matching layer, l/λ , where for each curve the value of Z_m ranges from Z_i , a value of 33.6 MRayl, through Z_f set to be 1.5 MRayl, numbers representative of solid PZT-5H and water, respectively.

For this case, the maximum acoustic transmission occurs when the matching layer thickness is $1/4$ or $3/4$ of the desired wavelength and T_i increases from 0.16 to 1.0 between 1.5 MRayl and 7.1 MRayl, then falls back to 0.16 at 33.6 MRayl. Intuitively,

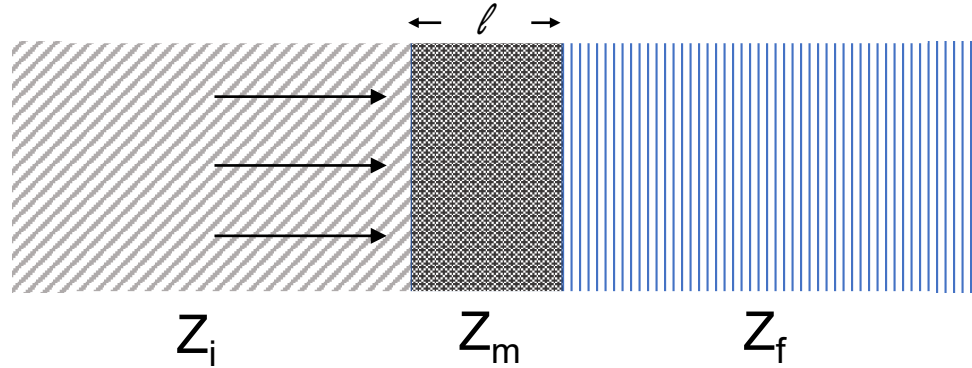


Figure 3.5: A single matching layer, acoustic impedance Z_m and thickness l , is placed between an initial and final acoustic medium to improve acoustic intensity transmission.

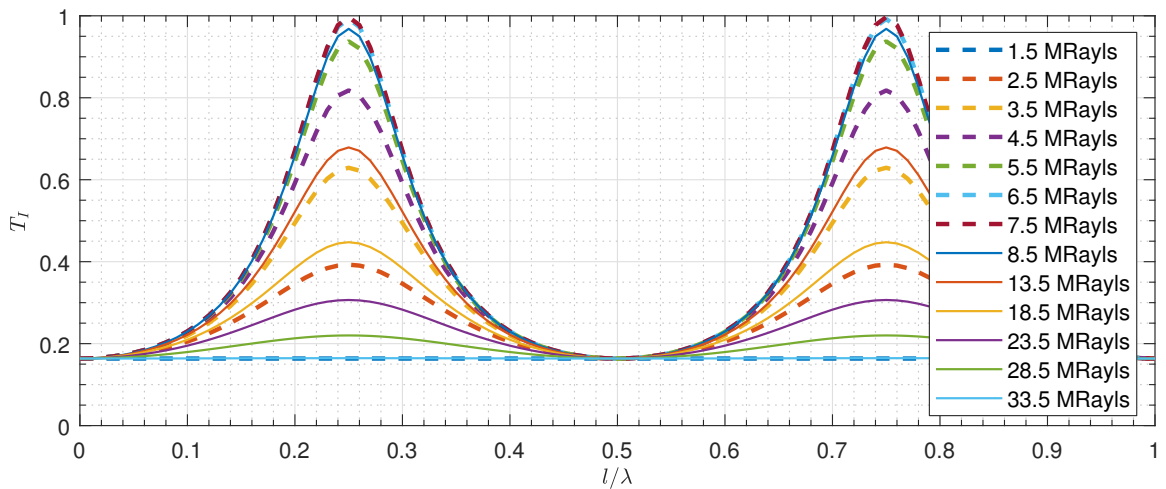


Figure 3.6: The transmitted acoustic intensity through a matching layer as a function of layer thickness which is given as a fraction of the acoustic wavelength is presented here. In this example, the initial medium has an acoustic impedance of 33.6 MRayl, and the final medium has an acoustic impedance of 1.5 MRayl. Multiple plots show how the transmission improves as the matching layer impedance increases from 1.5 to 7.1, and then drops again up to 33.5 MRayl.

a matching layer of 1.5 MRayl acoustic impedance is just an extension of the first medium, and similarly when $Z_m = 33.6$ MRayl the matching layer is an extension of the final medium so they represent a situation of only two mediums in contact and should have the same transmission coefficient, which can be calculated using Equation 3.10.

In practice, using a single matching layer is not always possible due to difficulty in finding materials with the appropriate acoustic impedance due to a large impedance mismatch between the acoustic element and medium of interest. There are published works which demonstrate the use of dual or multiple matching layer techniques to help with a large element to medium mismatch, such as the mass-spring matching layer technique by Brown *et. al.* [95], but they are not used in this work and are therefore outside of the scope.

3.5 Transducer Focusing

Focusing of an ultrasound transducer can be done, primarily, in three ways: through the use of a lens, through curving of the transducer itself to be naturally focused, or through beamforming - a process in which the transducer electrode, and sometimes substrate, is split into elements which can be pulsed at different times, leading to a dynamic focus.

Simple Lens

Design of an acoustic lens can be performed using Fermat's Principle of Least Time,

$$\frac{1}{v_l}d_l + \frac{1}{v_m}d_m = \frac{1}{v_l}s_l + \frac{1}{v_m}s_m \quad (3.13)$$

where v_m and v_l are the longitudinal wave speeds in the target medium and lens, respectively, and d_x and s_x , where $x = l, m$, correspond to distances in their respective media from Figure 3.7.

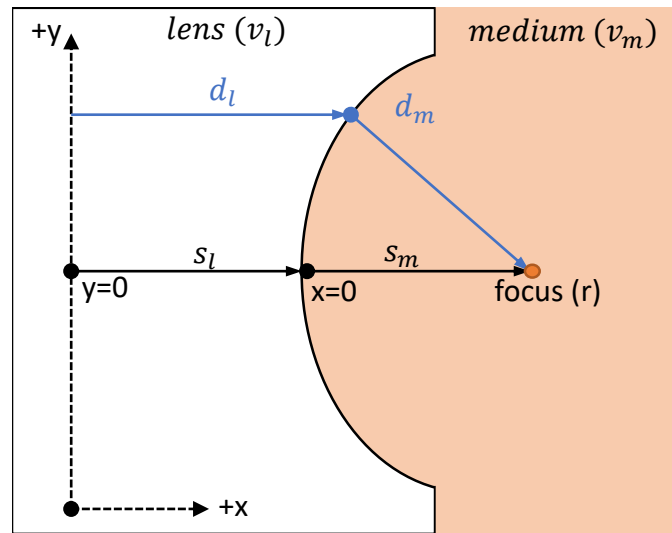


Figure 3.7: Fermat's Principle states that, to achieve lens focus, the time of flight for a plane wave traveling path $d_l + d_m$ must equal the time of flight for a wave on path $s_l + s_m$, where s and d are distances, and v_l and v_m are sound velocities in the lens and medium, respectively

Starting with Equation 3.13 and using trigonometry, the shape of the lens in Cartesian coordinates can then be calculated to be:

$$y^2 = x^2 \left(\left(\frac{v_m}{v_l} \right)^2 + 1 \right) + 2r_f x \left(1 - \frac{v_m}{v_l} \right) \quad (3.14)$$

where y and x are Cartesian coordinates for the curve, and r is the focal distance from the center of the lens curvature ($x = 0$ and $y = 0$), or focal radius. This form of the equation was derived, assuming that, again, all sound approaches the lens curvature as a plane wave. The shape described in Equation 3.14 is an ellipse, causing d_m to vary depending on the position along the curve, which leads to fabrication difficulties as the curvature cannot be simply described using a fixed radius. The shape itself can be made using computer controlled mills or lathes, but tolerances must be tight.

Fresnel Lens

A Fresnel lens is a modified version of the simple lens described in Section 3.5 which reduces the overall curvature of the lens while maintaining the same focal position. The process of designing a Fresnel lens is shown in Figure 3.8 in a series of three sub-figures.

Figure 3.8a shows a number of lens curve, all following Equation 3.14 and focusing at the same location, 8 mm, labeled as a circle in the figure. Note, each curve needs its focal distance adjusted by a distance D_f , the offset between each curve. This distance is calculated as,

$$D_f = N_f \frac{v_m v_l}{v_l - v_m} \frac{1}{f} \quad (3.15)$$

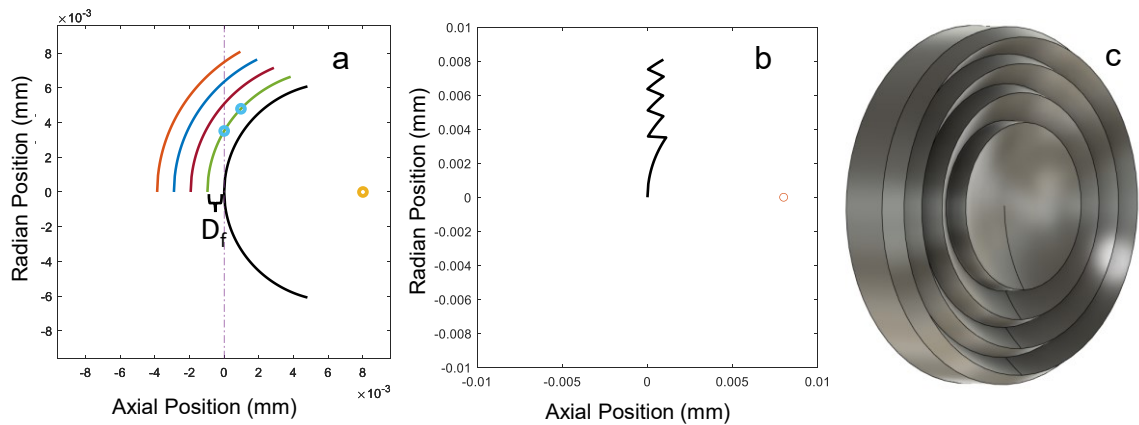


Figure 3.8: a) Multiple lens curves offset by a distance D_f share a focus at 8 mm. b) Linking the curves and trimming them outside the linked areas leads to the shape seen here, and revolving this curve around the focal axis gives a lens c) which can be machined.

where f is the operating frequency and N_f is the number of cycles delay at that frequency between waves arriving at the focus from each curve. Offsetting each ring by D_f ensures the pulse each ring emits is delayed by N_f cycles at the focus and, therefore, constructively interferes. This means the lens will only focus properly at the design frequency and its harmonics, and is designed specifically for one medium.

Recall that it was assumed the sound wave approaching the simple and Fresnel lens curvatures was planar, suggesting a flat ultrasonic element would be bonded to the back of the lens. Instead of a flat element, it is possible to have a curved element without a lens, the benefits of which could be: no machining (curvature is constant), easier modeling (ultrasonic element coupled directly to medium without lens), and the ability to fabricate using equipment commonly available to transducer labs.

Curved Composites

Almost no literature exists on methods for fabricating curved composite transducers, although a number of companies offer curved composite products. To curve a composite, the easiest method is to heat the composite and press it into a mould relying on the epoxy matrix to take on the desired shape. A curved composite for the work presented in this thesis has the benefit of a spherical curvature so the machining of the mould is relatively easy.

After manufacturing a curved composite transducer, presented at the International Ultrasonics Symposium 2016 in Tours, France [96], one of the biggest difficulties encountered was a low success rate during curvature. A few examples of failed composites can be seen in Figure 3.9, where the failures here range from damage during composite curving (1-3) to failures during initial composite development when substrates were too thin (5).

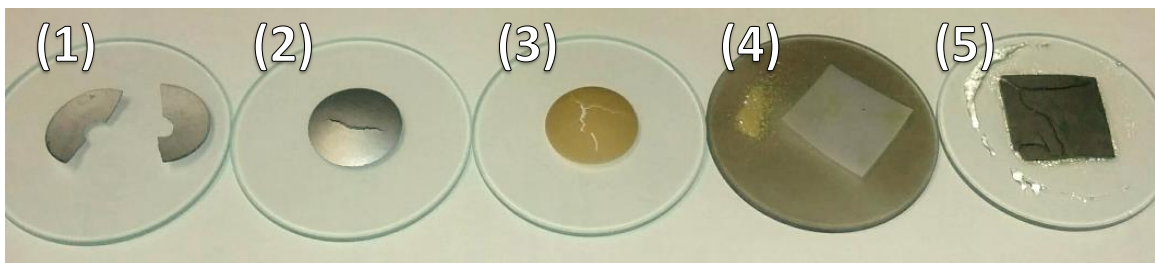


Figure 3.9: Composites one through three (1-3) failed during attempts to curve them, where four (4) failed during ultrasonic cleaning and five (5) failed during bonding due to the substrate being too thin

Even once the composite fabrication process had become reproducible, curving

of composites failed 75% of the time or more, making the whole process very time consuming. It is because of this, that spherically curving composites is not likely to be a cost-effective method for focusing histotripsy transducer without significant investment in engineering process improvement.

Transmit Beamforming

Transmit beamforming is a process where multiple piezoelectric elements are pulsed at different times so that the acoustic energy from each element arrives at the desired focus at the same time. The benefit of transmit beamforming is that the focus can be moved and, therefore, provides a wider range of targetability and depth for a fixed transducer size / shape. For the purposes of this project, an annular phased array holds some promise in providing a focus as it allows us to exploit radial symmetry in reducing number of elements and maximizing pressure. A schematic of an annular array is shown in Figure 3.10. The annular phased array, shown with a top and cross-section view on the left, is a set of concentric electrodes on piezoelectric material that, when pulsed electrically, sends out an acoustic wave with radial symmetry from the piezo area under the electrode only. The image on the right shows a focused pulsing scheme where the outer elements are pulsed earlier than the inner, as acoustic energy from the outer elements takes longer to reach the focus. Modification of the pulse delays can move the focus closer to or further from the array.

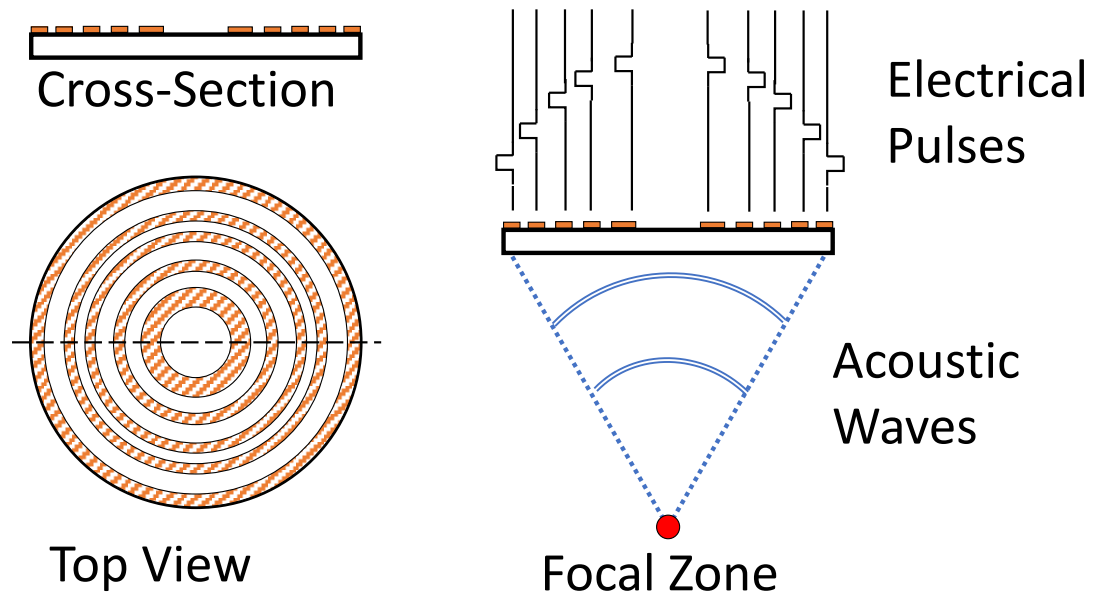


Figure 3.10: A cross-section and top view of an annular array are shown here, where the electrodes are crosshatched orange, showing distinct separations between each element. On the right, electrical pulses are sent to each element with a delay, where the outer element receives the pulses earliest as sound emitted from these elements must travel further to reach the focal zone

As a method of focusing, beamforming does have drawbacks. First, beamforming means additional electronics complexity as each element typically requires a dedicated circuit to pulse the element. Second, element directivity now comes into play as the element size has to be kept small limiting either the number of elements, or requiring more pulsers to drive the elements if a large array is required. Additionally, due to the directivity of the elements, they are each unable to deliver their full acoustic power at large angles so, for devices like those considered here with a tight focus, elements that are further from the focus may not fully contribute to reaching cavitation pressures.

3.5.1 Focusing Summary

Although the work presented in this thesis focuses on lens-based devices, spherically curved composites were demonstrated to be a functional histotripsy option [96] and could lead to a low-cost easy to make histotripsy device if the failure rate could be reduced; however, reducing the failure rate is expected to be a more industrial pursuit than academic. For small form-factor devices, using transmit beamforming either linearly or with an annular array is outside of the scope of this work, but has been demonstrated to be capable of steerable tissue ablation by Mallay *et. al.* for both a linear array [97] and an annular array device [98], and thus warrants further examination.

3.6 Transducer Modeling

To model an ultrasound transducer, it is common to use either one of or a combination of, three different modeling techniques: Krimholtz, Leedom, and Matthae (KLM) Method, the finite-element method FEM, or the spatial impulse response method. The KLM method, which is the least computationally intensive, simplifies a transducer down to a 1-dimensional linear matrix model and provides information about the mechanical composition, the electrical characteristics, and the acoustic pressure at the transducer face, but provides no detailed information about the acoustic field.

FEM can be a 1D, 2D, or 3D model of the electrical, mechanical, and acoustic properties of a device, as well as the medium the device is operating in; however, the models themselves are the most complex, and require the longest time to create, verify, and compute. The spatial impulse response method provides no information about the transducer mechanical or electrical properties, but is quick and efficient at providing the acoustic field that a transducer might generate.

In this work, since using a lens to focus is expected to lead to the highest possible focal pressure, KLM models will mainly be used in simulating transducer properties for fabrication. KLM will allow for the most rapid iteration in transducer designs due to its bi-directional nature where a model-based transducer can be designed based on best estimates of properties, followed by building the device and measuring properties which do not perfectly match the model, then iterating on the model and optimizing based on measured properties. An updated transducer can then be simulated and built based on new model outputs. FEM will be performed to confirm some pressure field measurements.

Krimholtz, Leedom and Matthaei (KLM) Model

The KLM model was first developed and introduced in a series of two (2) papers by Krimholtz, Leedom, and Matthaei [99, 100]. The KLM transducer model treats the transducer as a set of one-dimensional linear circuit elements, each of which can be

represented by a 2-by-2 matrix defining the input-output relationship of the element.

If the matrices are multiplied together as shown in Figure 3.11, they then relate the input-output of each object sequentially, leading to an input-output relationship for the entire transducer. For a piezoelectric transducer, the physical model shown in

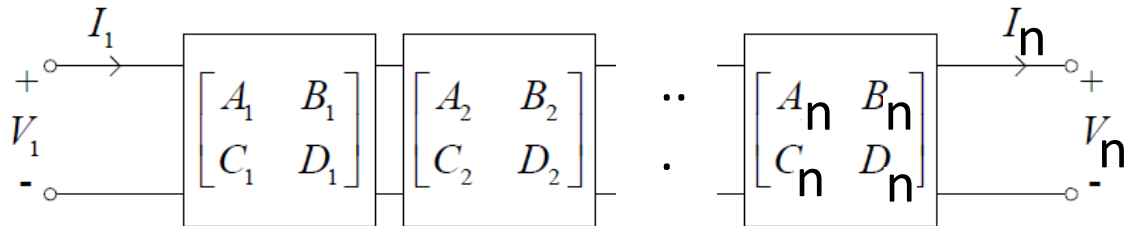


Figure 3.11: Generic KLM matrices multiplied together can relate any number of input-output relationships together. Here, the ABCD elements vary for each matrix

Figure 3.12 can be broken down into seven matrices, one for each of the outlined objects: C_o and C' are capacitances on the electrical side of the transducer, ϕ is the transformer ratio which describes the conversion of energy from the electrical to the mechanical domain, the two terms containing Z , c_0 and l are acoustic transmission lines, and the acoustic ports are the acoustic load where ultrasound energy is deposited. The equation for C_0 is given by Equation 3.9, ω_p by Equation 3.6 and the other circuit parameters by:

$$Z_a = AZ_0 = Ac_0\rho_0 \quad (3.16)$$

$$C' = \frac{-C_0}{k_t^2} \frac{\pi\omega/\omega_0}{\sin(\pi\omega/\omega_0)} \quad (3.17)$$

$$\Phi = k_t \sqrt{\frac{\pi}{\omega_0 C_0 Z_a} \frac{\sin(\pi\omega/2\omega_0)}{\pi\omega/2\omega_0}} \quad (3.18)$$

The front and back acoustic ports in Figure 3.12 can be coupled to additional media by creating an additional matrix in the model using the Z , c_0 and l parameters of the medium. All of these properties of materials are typically available in specification sheets or online for piezoelectrics; however, when using a piezoelectric-epoxy composite the bulk properties of the composite are used as plotted in Figure 3.4 of Section 3.3. These values sometimes cannot be found in available literature and must be measured directly, or by adjusting the KLM output to match measured values.

After fabricating a new composite the electrical impedance can be measured and the physical properties such as density, speed of sound, thickness, and acoustic impedance can all be determined and entered into the KLM model. Properties such as k_t , and the loss-factors Q , and $\tan\delta_e$ can then be left as free parameters and adjusted in the model to provide the best fit to the measured data. Once all of these intrinsic properties are known, rather than having to build a new transducer each time you wish to adjust a parameter, every variable can be adjusted in KLM to

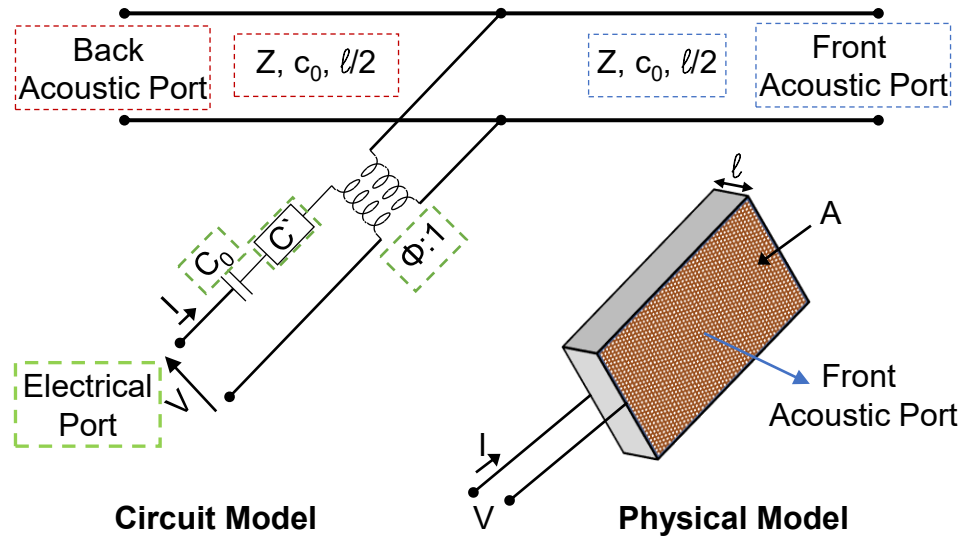


Figure 3.12: The model used for KLM simulations of a single-element piezoelectric transducer, where each outlined variable or set of variables is a single, 2×2 matrix in the KLM model or, in the case of the ports, an input/output.

determine how it would affect transducer output. The KLM model can be used to determine not only electrical impedance, but input electrical power, output acoustic power, and the device response to any electrical input, resulting in simulated one-way or two-way pulse bandwidths. For a lens-based device such as examined in this work, a single KLM simulation will not be able to capture the behavior of the lens curvature, but breaking up the device into multiple KLM elements as shown in Figure 3.13 can lead to electrical impedance data and pulse shapes which closely match the measured values.

The side view of an aluminum lens based device shown in Figure 3.13 has a piezo composite epoxied to an aluminum lens with a matching layer between the lens and water. To simulate this device in KLM, it is broken into concentric rings and each

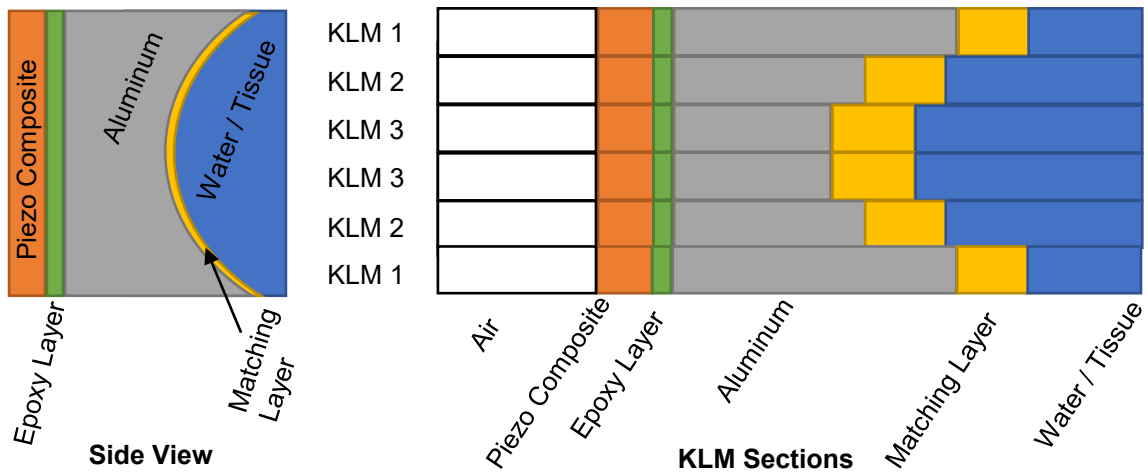


Figure 3.13: The thickness of a lens varies with position along the curvature, so multiple KLM models must be used. Here, the smooth curve of a lens is discretized into multiple separate 1-D models.

ring becomes a separate simulation placed in parallel with each other ring to ensure the device is properly loaded.

FEM Acoustic Field Simulations

Simulating the acoustic field of a lens-based device can be done through a number software packages, but to capture the behavior of complex acoustic fields in situations which involve multiple materials (e.g. piezo transitioning to aluminum transitioning to water / tissue) while also avoiding the inclusion of simplifying assumptions, FEM should be used as it calculates pressure, particle velocity, and other system properties by modeling sets of coupled differential equations capturing the physics of the system. In this work, FEM modeling will be performed using the free MATLAB Toolbox kWave [101] and COMSOL Multiphysics.

FEM simulations start by representing the geometry of the system which, for complex shapes, often involves a CAD model. This CAD model is then broken into a mesh - a series of connected points where the physics at each point can be calculated based on a set of differential equations coupling each point to its neighbors. An example cross-section of one of these meshes taken from the work in Chapter 5 is shown in Figure 3.14, where the yellow grid points have been assigned the properties of aluminum, and the blue have been assigned the properties of water. The red line was used as a pressure source generating a continuous-wave pulse to determine the steady-state pressure field.

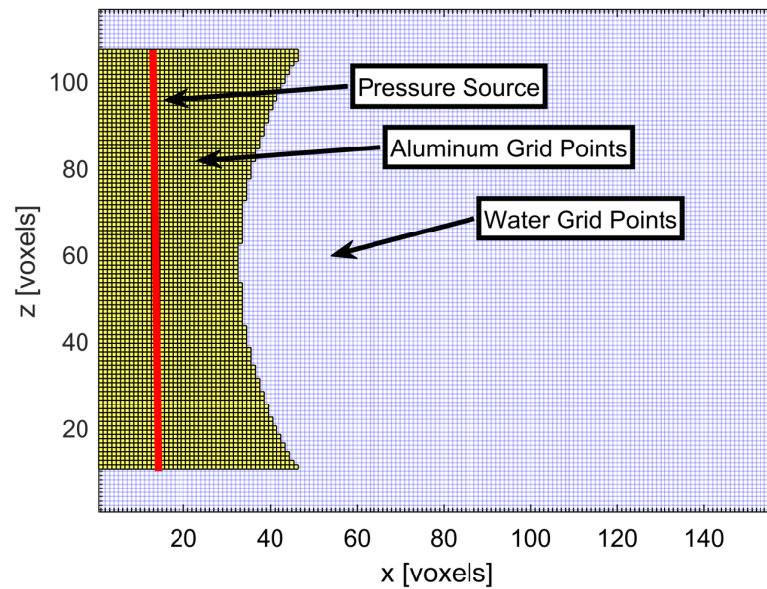


Figure 3.14: A grid of points in an FEM model, where the lens material is labeled in yellow, the water medium in blue, and a red-line represents the pressure source.

The kWave simulations performed for the work in Chapter 5 used a 3D grid and modelled the full lens since the lens was square, while the COMSOL simulations

from Chapter 6 used a 2D axisymmetric simulation since the lens was cylindrically symmetric.

Chapter 4

A Low-Cost Miniature Histotripsy Transducer for Precision Tissue Ablation

Preamble

Chapter 4 presents work on creating a 10 mm aperture, co-registered imaging and histotripsy ablation transducer using an aluminum lens for focusing of the histotripsy with a hole in the lens center to allow space for an imaging array. The work for this has been published in IEEE Transactions on Ultrasonics, Ferroelectrics, and Frequency Control[102] and is presented mainly here in the form in which it was published. Some introductory content from Chapter 4 may exist within Chapters 2 and 3 of this thesis, however, it was kept here as well to maintain context of the specific work presented herein.

©2018 IEEE. Reprinted, with permission, from Jeffrey K. Woodacre, Thomas G. Landry, Jeremy A. Brown, A Low-Cost Miniature Histotripsy Transducer for Precision Tissue Ablation, IEEE Transactions on Ultrasonics, Ferroelectrics, and Frequency Control, Nov. 2018.

In reference to IEEE copyrighted material which is used with permission in this thesis, the IEEE does not endorse any of Dalhousie University's products or services. Internal or personal use of this material is permitted. If interested in reprinting/re-publishing IEEE copyrighted material for advertising or promotional purposes or for creating new collective works for resale or redistribution, please go to http://www.ieee.org/publications_standards/publications/rights/rights_link.html to learn how to obtain a License from RightsLink.

4.1 Introduction

It has been shown for a number of surgical procedures that a minimally invasive surgery (MIS) approach, when compared to open surgery, can offer improved patient outcomes including: less blood loss, fewer complications, faster recovery time, and a reduced chance of infection[1, 2, 3, 103]. These outcomes have led to a surgical trend of avoiding open surgery in favor of MIS, when possible [5, 6]. To allow more procedures to be performed as minimally invasive, it's important to develop new tools to add to a surgeon's repertoire, with the logical extension being if MIS procedures are good for patient outcomes, then fully non-invasive procedures should be better still, assuming the same surgical goal can be achieved. Currently, two ultrasound based non-invasive surgical techniques are available: high-intensity focused ultrasound ablation, often referred to simply as thermal HIFU or HIFU, and histotripsy.

Where thermal HIFU typically uses an extracorporeal focused ultrasound transducer to cause tissue necrosis through sustained ultrasound absorption resulting in cell hyperthermia near the focal zone[104], histotripsy, often using a similar transducer design, causes tissue fractionation through short, powerful cavitation-inducing ultrasound bursts where the destruction is caused by cavitation bubbles collapsing [31]. HIFU has been used to treat tumors in the prostate, breast and liver, among other organs with, in many cases, reported successes in tumor reduction and/or pain relief [105]. Histotripsy, being a relatively new area of ablation research, has yet to have a human clinical trial completed; however, a number of animal trials have published reporting on the efficacy of treating benign prostatic hyperplasia on a canine model [106, 33], hepatocellular carcinoma on a porcine model [107], and thrombolysis in a porcine model [108]. Note, there are HIFU devices which are not extracorporeal such as two commercial systems: one produced by Sonacare Medical (Sonacare Medical LLC, Charlotte NC, USA) and one by Edap TMS (Edap TMS, Vaulx-en-Velin, France), both for trans-rectal prostate treatments. Additionally, a laparoscopic HIFU probe for kidney ablation was presented by Tavakkoli *et. al.* in 2001[109]. In general, however, many HIFU transducers in literature are physically too large for anything other than transdermal treatments and, for histotripsy, the authors could find no publications on transducers meant for intracorporeal use.

One of the first histotripsy transducers in publication was presented by Roberts

et. al. in 2006 as a transcutaneous, 750 kHz 18 element annular array transducer with a diameter of 145 mm and a 100 mm focal length [110]. The transducer was co-registered with a commercial diagnostic 2.5 MHz imaging probe for simultaneous imaging and ablation. Histotripsy ablation studies have also been performed using a 100 mm aperture curved bowl with a 90 mm focus operating at 1 MHz [111], a 500 kHz, 32-element 150 mm focus transducer [70], and four 50 mm aperture, 70 mm focus, 1 MHz transducers directed to the same focus [112]. Histotripsy as high as 3 MHz has been demonstrated using a piezoelectric multi-element, dual-beam technique [113] and as low as 345 kHz [114] for another piezo-based multi-element transducer. Recently, high frequency (greater than 10 MHz) free-field acoustic cavitation in water has been demonstrated using laser-generated focused ultrasound (LGFU) with both a dual-beam method [115] as well as a single-beam method using a tightly focused lens [116]. Furthermore, a 15 mm aperture LGFU device has been shown capable of ablating gel-phantoms and small volumes ($<1 \text{ mm}^3$) of bulk tissue [117]. These LGFU devices coat a focused lens with an optically absorptive material having good optoacoustic conversion efficiency, carbon nanotube based coatings for example, which then generates an intense ultrasound pulse through the photoacoustic effect when hit by a short laser burst. The laser required for this work is typically costly, and the devices would possibly require an imaging array to monitor the process within tissue;

nonetheless, LGFU has potential to be commercially viable within the area of cavitation ultrasound treatments. It should be pointed out that high-intensity ultrasound pulses aren't necessarily a requirement for cavitation treatments as has been shown by Kim *et. al.*, who have used a low frequency ($< 1\text{MHz}$), moderate power transducer in combination with microbubble contrast agent to perform sonothrombolysis using the microbubbles as cavitation nuclei [118].

With the exception of Kim *et. al.* [118], the multi-element nature and/or overall transducer size of the piezoelectric devices mentioned above limits treatments to extra-corporeal use which, for many cases, is beneficial in that it allows histotripsy to be a completely non-invasive treatment method for tumor resection. For neurosurgery, however, extra-corporeal histotripsy is very difficult, as the skull strongly attenuates and reflects ultrasound energy making it difficult to not only reach the cavitation threshold, but also to monitor the treatment using ultrasound. Sukovich *et. al.* [119] demonstrated that a 30 cm aperture, 500 kHz, 256-element phased ultrasound array could reach the cavitation threshold through a skull-cap to ablate red blood cell (RBC) phantoms, showing promise for through the skull histotripsy, but imaging feedback may still be desired to ensure precise targeting.

Currently, one of the most common methods of tumor resection in the brain is the use of burr-hole surgery, in which a hole is made in the skull and, using visual guidance as well as pre-operative MRI images, a cavitation ultrasonic surgical aspiration

(CUSA) device is used to ablate the tumor tissue. This CUSA treatment is a contact ablation where the device cavitates and ablates tissue adjacent to the tip and the liquified tissue is then pulled away via suction. Although effective, the surgeon cannot visualize below the surface and ablate at the same time using this method; therefore, it is proposed that if a histotripsy device could be made which both images and ablates and this device could additionally be made small enough to enter a burr hole, that such a device could potentially be used as a replacement to the CUSA tool. Some other potential surgical applications for a small co-registered histotripsy ablation device include: spinal surgery, and intracardiac surgery, although these have yet to be explored in literature.

In this Chapter a small, 10 mm aperture histotripsy transducer was characterized, shown to be capable of free-field cavitation and, following characterization, the device was modified to include a co-linear, co-registered 40 MHz imaging device to allow both imaging and ablation in real-time with a 10 mm aperture. This device is a first step in creating a hand-held tool small enough to be used in neurosurgery, as well as other endoscopic surgery requiring high-resolution imaging and highly targetable, tightly focused ablation zones such as spinal surgery, cardiac surgery, and thrombolysis.

In Section 4.2, the transducer fabrication steps are provided followed by characterization of the device impedance and pressure output in Section 4.3. In Section 4.4, the device is modified to allow co-registration with an endoscope and results focusing

on what is important for co-registered imaging and ablation are shown. Section 4.5 outlines some potential future paths research with this device may follow.

4.2 Design and Fabrication

The ultrasound ablation transducer consists of an air-backed piezoelectric composite bound to an aluminum lens using epoxy, where the aluminum lens has a quarter wavelength matching layer on the front face matching to water. A cross-sectional view of the device design is shown in Figure 4.1. Note that for the co-registered version a 4 mm x 4 mm square hole is machined through the center of the lens and composite to allow an endoscope to pass through. No other changes are needed for co-registration.

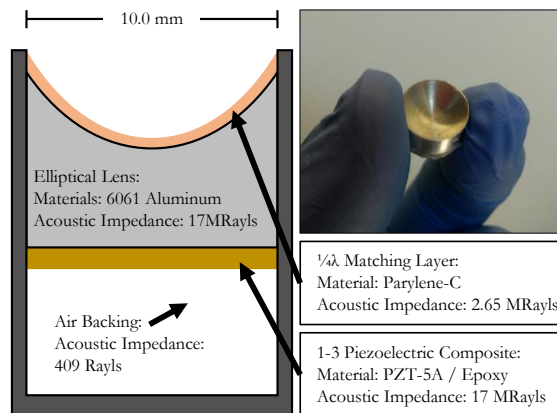


Figure 4.1: A cross-sectional view of the transducer design shows an air-backed piezoelectric composite with an aluminum lens and parylene matching layer. The lens-piezo stack can be seen in the picture.

The piezoelectric composite was designed to provide maximum output power near

5 MHz with the composite itself being a 1-3 PZT-5A-polymer dice-and-fill design. PZT-5A was chosen over PZT-4 or PZT-8 for its high clamped dielectric constant, resulting in a lower impedance and more overall power per volt, its high electro-mechanical coupling coefficient, increasing bandwidth so maximum output can be reached in fewer cycles, and relatively high coercive field compared to other PZT-5's. The composite was modeled using in-house Krimholtz-Leedom-Matthaei (KLM) [99] code. The KLM method treats a composite as a bulk material with effective properties and has been successfully used to model piezoelectric composites [120, 121] as well as multi-layer piezoelectric devices [95]. It is understood that KLM may not be as accurate as a full 3D FEA model, however, KLM was used as a starting point for transducer fabrication as it is quick to run the code and tune parameters, provides reasonable estimates of the electrical impedance, transducer electrical power input and acoustic power output, and there was minimal software cost associated with the code development. A finite-element model could be developed in the future if further refinement is needed.

The KLM code provided a design thickness of 303 μm and a pillar geometry resulting in a characteristic acoustic impedance of approximately 17 MRayls, matching closely to the characteristic impedance of 6061-T6 series aluminum. Cost for materials and fabrication of a 63 mm x 63 mm piece of composite with the final design properties was \$558 USD, allowing the creation of 36 transducers after accounting for

waste, thereby using \$15.50 USD worth of composite per device. The composite was attached to the aluminum lens using a thin film of Epotek 301 epoxy resin (Epoxy Technology Inc.) at negligible additional material cost per device.

Our KLM code shows the epoxy film thickness and properties modify the overall transducer output where simulations show increasing film thickness, while ensuring the film is still much thinner than the operating wavelength, seems to establish a new resonant cavity which could improve acoustic power output for a given input voltage but at the cost of reduced bandwidth, as well as a frequency shift of the resonance. A similar frequency shift and slight increase in transducer surface velocity when adding thin glue layers was found in simulations by Dang in a 2001 thesis[122] while studying the bonding of transducers for non-destructive testing to a wear plate, however, a one-to-one comparison is not possible as the transducer in question was not a composite and was backed. We believe this frequency shift suggests the effect of adding an epoxy layer may be different from simply introducing a mismatch between composite and lens, which would add a resonance but would largely maintain the resonance frequency of the composite itself. The authors propose that the material selection and thickness of this layer adds an additional tuning factor to device fabrication and, although not explored in this work, could lead to further study to determine the trade-offs between different layer compositions and thicknesses; however, further examination of these factors was outside of the scope of this work as the epoxy layer effect was merely

discovered as an outcome of manufacturing.

For this device, KLM models show that a film thickness of 20 μm was introduced during manufacturing, shifting the maximum output frequency from 5 MHz for bare composite to 6.8 MHz for the composite-epoxy-lens stack. This frequency shift can be seen in Figure 4.2 where the model shows adding a lens directly to composite reduced the peak efficiency frequency to 4.5 MHz compared to pure composite, while adding the 20 μm epoxy layer moves this peak efficiency point to 6.8 MHz.

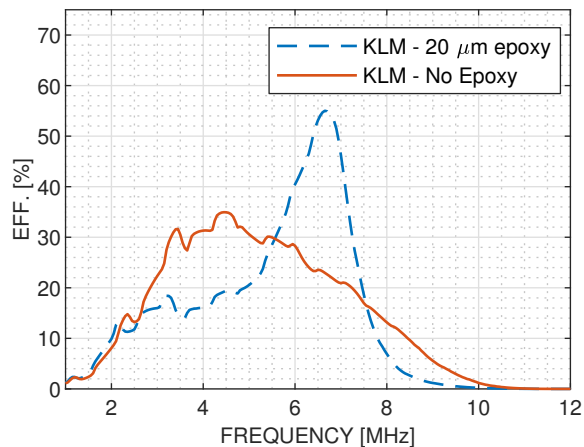


Figure 4.2: From the KLM model, the addition of a 20 μm epoxy layer shifts the output efficiency of the composite-lens-matching layer device from peaking at 4.5 MHz to 6.8 MHz, while also improving upon overall efficiency.

The aluminum lens was fabricated using a CNC milling process and designed to focus at a 7 mm depth from the bottom of the lens curvature, resulting in a 3.7 mm focal distance from the lens face. The curvature of the lens is elliptical and can be

described using the following equation, derived from Fermat's principle of least time:

$$y^2 = x^2 \left(\left(\frac{v_m}{v_l} \right)^2 + 1 \right) + 2r_f x \left(1 - \frac{v_m}{v_l} \right) \quad (4.1)$$

where y and x are cartesian coordinates for the curve, v_m and v_l are the longitudinal wave speed in the ablation medium and lens, respectively, and r_f is the focal distance from the center of the lens curvature ($x = 0$ and $y = 0$), or focal radius. The elliptical lens shape ensures no spherical aberrations in the lens, which are especially important to avoid when the lens focus is smaller than the aperture. Note, the cost of each lens was \$51.50 USD for a low quantity, and could be reduced when ordering in larger numbers.

On the lens face a quarter wavelength parylene matching layer was deposited using the Specialty Coating Systems PDS-2010 Parylene Coater (Specialty Coating Systems Inc., Indiana USA). Parylene has a longitudinal speed of sound of 2135 m/s with an acoustic impedance of 2.75 MRayls [123], so a layer thickness of 78.2 μm was deposited to match at 6.82 MHz. The cost of parylene deposition depends on the number of devices being treated, but could be reduced to less than \$10 USD per device in small batches of at least five (5). The purpose of the matching layer is two-fold: to increase bandwidth, and to reduce acoustic losses in the transducer stack by minimizing the magnitude of reflections back into the device.

A basic casing for the transducer was made using the Formlabs Form 2 3D SLA printer (Formlabs, Inc., Somerville, MA USA) where the finished transducer was installed and sealed with Epotek 301. The total resin cost for this casing was below \$15 USD based on the amount of resin used.

Overall, the major material costs of one of these transducers come from the composite, lens, parylene, and casing costs which total \$92 USD. This cost could be further reduced when fabricated in bulk. Additionally, assembly time is limited by curing of epoxy and parylene deposition but requires one person only a few hours of work over four days.

4.3 Characterization: No Co-registration

Characterization of the non-coregistered transducer was done through electrical impedance measurements both before and after lens bonding, a pressure field map near the transducer focus, a measure of the peak minimum focal pressure versus drive voltage, and imaging of a single-cycle pulse generated bubble cloud. As mentioned, in-house created KLM code was used to model the transducer electrical impedance, efficiency, and power output. This KLM code was able to model, not only a bare piezoelectric composite but also, the full transducer stack which included an epoxy bonding layer and aluminum lens. To include the lens in the KLM model, the composite-lens stack was divided into a set of concentric rings of equal area, each with equal backing,

composite, epoxy and parylene layers, but with aluminum layer of varying height to account for the lens curvature varying as a function of radius. For example, at the center of the lens, a ring would be modeled as having a 2 mm aluminum layer as part of the lens, while a ring at the outer edge would be modeled with a 4.4 mm aluminum layer as the lens curvature is larger at the outer edge. Once each ring was modeled in KLM separately, the electrical impedances for each ring were combined in parallel to reconstruct the true device impedance. A similar method for transducer modeling was presented by Marçal *et. al.* in 2007 [124] where they used concentric rings in KLM modeling of a lens while, additionally, modeling angle-dependent reflections at mating surfaces.

The experimental electrical impedance, measured using an Agilent 4294A Precision Impedance Analyzer (Agilent Technologies, Santa Clara, USA), and the KLM derived electrical impedance are shown in Figure 4.3 for a 10 mm diameter disc of air backed and air loaded composite prior to attaching a lens.

For the KLM model to match impedance measurements, measured properties such as composite thickness, volume fraction, density, and effective electro-mechanical coupling factor were measured and entered into the model while damping coefficient, clamped capacitance, and acoustic impedance were adjustable parameters. Adjustment of the model acoustic impedance to match measurements was guided with knowledge of the volume fraction and composition of the composite, and more accurately

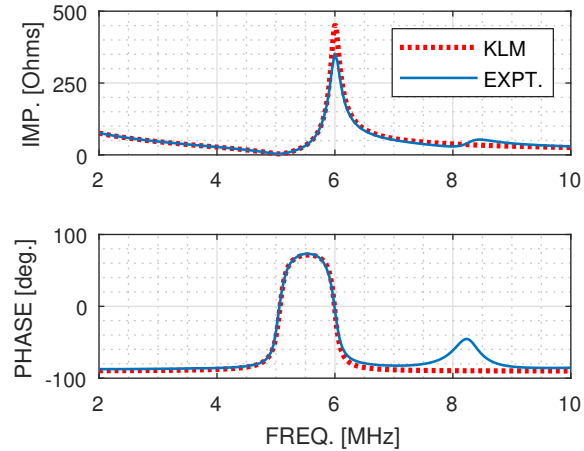


Figure 4.3: The electrical impedance of a bare piece of 10 mm diameter composite is shown here, with a KLM model closely matching. This measurement was performed with air backing and an air load on the composite.

determined by comparing the position of the impedance minimum and maximum.

Since the composite density was known, modifying impedance changed the composite speed of sound and thus the resonance and anti-resonance peaks in the model. By

matching KLM with the measured electrical impedance, it was determined that the composite acoustic impedance was 13.8 MRayls, not the 17 MRayls designed for. The

damping coefficient had a strong effect on the shape of the phase plot so adjustment of this to match between model and experiment was straightforward. Similarly, the

clamped capacitance had a significant effect on the the model resonance and anti-resonance heights, as well as the impedance slope before and after these points, so

a value which brought the curves into close match could be chosen without effecting other parameters. Full KLM values used for the composite are provided in Table 4.1,

with additional data for the lens, matching layer and epoxy bonding layer which are

used in KLM modeling of the composite-epoxy-lens stack. Note, that near 8 MHz in the experimental impedance curve of Figure 4.3 is a second resonance feature corresponding to a lateral mode of the composite which is not captured in KLM, as KLM is inherently a one-dimensional model. This one-dimensional limitation also leads to difficulties in matching KLM output to the full transducer electrical impedance when a lens is introduced which is discussed later.

The discovered mismatch between the initial 17 MRayl design acoustic impedance, which matched aluminum, and the 13.8 MRayls simulated composite impedance suggests increasing the volume fraction of future composite designs is needed; however, it was assumed there would be direct contact between the composite and lens and, for

Table 4.1: The bulk properties used for each KLM layer

KLM Property	Composite	Lens	Parylene	Epotek 301
Acoustic Impedance (MRayls)	13.84	17	2.75	3.05
Speed of Sound (m/s)	3650	6320	2135	2649
Attenuation Coeff. (Nepers/m)	190.2	0	0	0
Thickness (μm)	303	Varied	75	20
Clamped Dielectric (1)	424.0	-	-	-
Effective Coupling Factor	0.573	-	-	-

this 13.8 MRayl composite, the transmitted power to the lens would be 98.9% based on the acoustic impedance mismatch. Matching of measured impedances to KLM shows this to not be the case and, in fact, simulations show the epoxy layer introduced a resonance-antiresonance feature in the measured and simulated impedance curves in the 5 MHz to 7 MHz range, as visible in Figure 4.4.

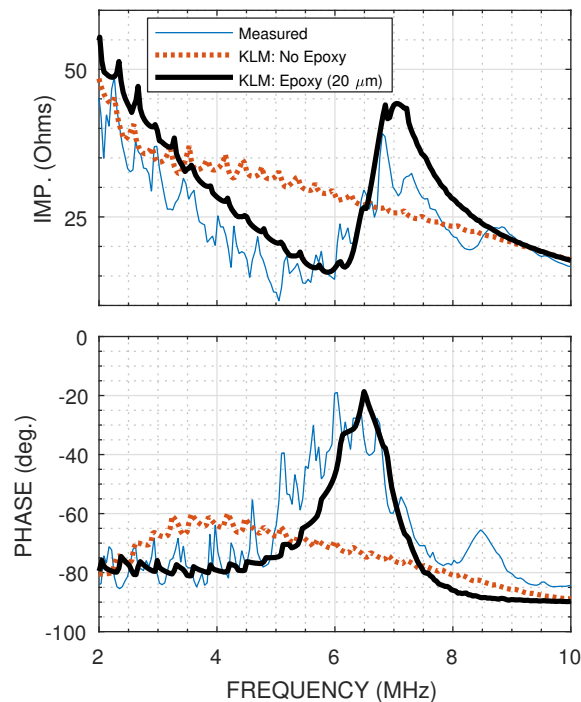


Figure 4.4: The upper plot shows the electrical impedance magnitude of a composite-lens stack along with KLM models both with and without the bonding epoxy between composite and lens. Modeling the bonding epoxy is necessary to ensure the KLM resonance matches the measured resonance. Discrepancies are likely due to the inability of KLM to model internal lens reflections. The lower plot shows the electrical impedance phase where, again, the addition of 20 μm of epoxy allows KLM to more closely match the phase characteristics.

The measured impedance magnitude (thin solid line) in Figure 4.4 (top) shows a resonance near 5 MHz and an anti-resonance between 6.5 and 7.0 MHz; however, a KLM model with composite in direct contact to the lens (dotted line) shows only a

decreasing impedance magnitude with increasing frequency. The addition of a 20 μm epoxy layer (thick solid line) is therefore necessary to capture the measured system behavior in the model. Also of note are a number of small, 5-10 Ohm peak-to-peak amplitude oscillatory features between 2 MHz and 7 MHz that are visible in the measured impedance, and 10 - 20 degree peak-to-peak oscillations in the phase. These variations are likely caused by internal reflections from the face and sides of the lens back to the composite. A smaller version of the variation is captured by the KLM models which can be seen in the KLM model plots. The difference in magnitude of these smaller resonances is likely caused by the model assuming reflections are 1-dimensional only and, therefore, cannot travel laterally between the concentric rings in the sectioned KLM model, whereas in the real system these reflections would be normal to the lens surface and travel in many directions within the lens.

The impedance phase curve in Figure 4.4 also shows the importance of an epoxy layer where the 20 μm epoxy layer moves the maximum phase point from 4 MHz to 6.5 MHz and increasing the value from -60 degrees to -20 degrees, again, more closely matching to the measured electrical impedance. Experimentally, we've found maximum pressure output closer to 6.8 MHz, the maximum efficiency point as shown in Section 4.2 using KLM. Knowing the shift in output adding a lens creates, we can calculate the focal pressure increase of adding the lens to composite by comparing the focal pressure of the composite only, assumed to be a piston transducer, to the

lens-composite stack, assumed to be a loaded concave radiator. Given a constant, continuous wave drive voltage, we find that the surface velocity of the lens-composite stack is 2.53 times smaller than the composite acting as a piston device due to damping from the lens and, additionally, is shifted to 6.8 MHz. Using these peak surface velocities, the axial pressure field for both the planar composite and the focused lens-composite stack[125] was calculated. We find that the addition of the lens provides a total pressure increase of 10.2 when compared to the composite itself due to the high focal gain of the lens. With the frequency shift and pressure gain in mind, a measure of the pressure field at maximum output drive frequency near the focus was performed using a 0.04 mm needle hydrophone (Precision Acoustics Ltd., Dorchester, UK) with a 7 MHz sensitivity of 5 nV/Pa. This pressure field is shown in Figure 4.5.

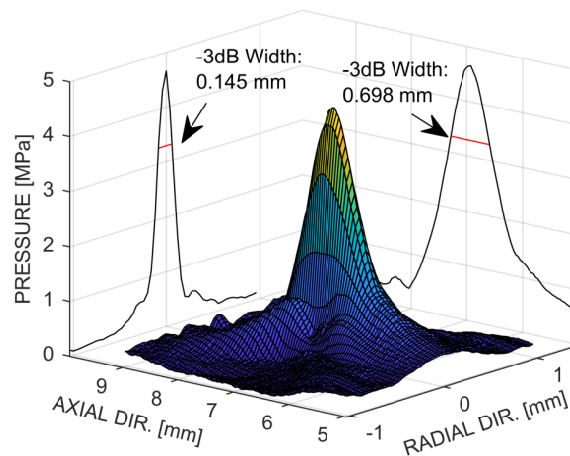


Figure 4.5: The transducer pressure field was measured centered at the focus, where the transducer was driven at 20 V with a 6.8 MHz, 20 cycle pulse. The acoustic waves are propagating in the axial direction. The focal -3 dB width in the radial direction is show as measuring 0.145 mm, while the axial -3 dB length is 0.698 mm.

The pressure field was measured in a 5 mm x 2 mm plane intersecting the transducer focus where the plane normal vector is perpendicular to the direction of acoustic propagation. Using an XYZ-stage capable of micron accuracy and repeatability, the 0.04 mm needle hydrophone was scanned through the pressure field, where an oscilloscope recorded the peak-negative pressure while the transducer was driven using a low-cost (<\$100 USD) pulser based on the design by Brown and Lockwood [126] with a 20 cycle, 20 V, 6.8 MHz pulse. The -3 dB width in the radial direction is 0.145 mm, or 0.207 mm full-width at half-maximum (FWHM), closely matching to the theoretical FWHM for a focused concave transducer of $1.4\lambda f = 0.222\text{mm}$ [125], where λ is the wavelength at 6.8 MHz in water, and f is the f-number, 0.7, of the transducer. In the axial direction, the -3 dB length measures 0.698 mm, deviating from the theoretical -3 dB approximation of $7.2\lambda(f)^2 = 0.799\text{mm}$ [125] by 13%. Deviations between FWHM and -3 dB axial beam length theory and measurement can be potentially be attributed to imperfect machining of the lens as well as the lens being elliptical and not a constant radius of curvature as assumed in the calculations. Note, that these beam measurements have shown that there is a single, sharp focus for this transducer and no secondary lobes are high enough pressure to cause ablation in tissue.

With the pressure field mapped, focal pressure as a function of drive voltage was measured at steady-state using a 20 cycle, 6.8 MHz pulse to confirm the possibility of

reaching the intrinsic cavitation threshold needed for histotripsy (26.1-27.9 MPa at 3 MHz in water [114]). Figure 4.6 shows the results of this measurement between 0 and 25 V, with an inset plot of a representative one-way single-cycle pulse response as measured at the hydrophone to provide device bandwidth. Within the inset, temporal ringing following the main pulse is likely a result of reverberation within the lens, and potentially also ringing within the hydrophone which could not be uncoupled from the measurement.

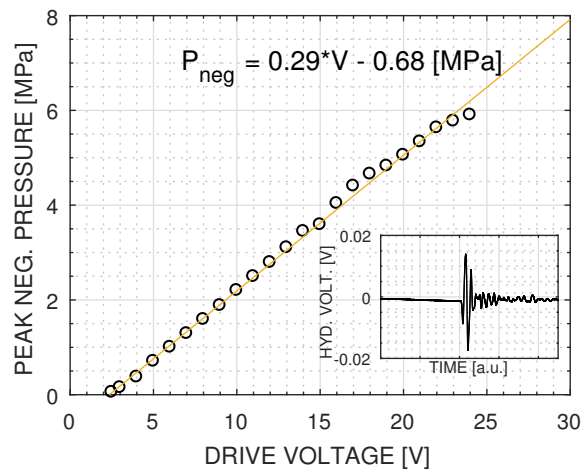


Figure 4.6: The 10 mm diameter transducer focal pressure as a function of drive voltage was measured at steady-state using a hydrophone. A linear relationship between pressure and drive voltage is seen from 2.5 V up to 17 V. Above 17 V, initial evidence of cavitation at the hydrophone tip was seen as noise in the oscilloscope signal. At 25 V, cavitation at the hydrophone tip made pressure measurements inconsistent and, therefore, measurements were stopped. The inset plot shows a one-way, single-cycle pulse response as measured with the hydrophone. The ringing after the initial pulse is likely due to reverberations within the lens. The pulse bandwidth is 59%.

The transducer was driven with a 20 cycle pulse train to ensure steady-state was reached at 6.8 MHz with a pulse-repetition frequency of 100 Hz. A minimum drive voltage of 2.3 V was needed for the drive circuit to power the transducer, after which

point the pressure follows a linear trend of 0.29 MPa / V up to 25 V. Following a linear extrapolation, to reach the water intrinsic threshold a drive voltage of greater than 90 V should be needed for a multi-cycle pulse. In reality, the pressure will fall off due to non-linear acoustic effects and, additionally, the pressure must exceed the intrinsic threshold by a few MPa before cavitation probability reaches 100% [127], and further still for consistent bubble cloud formation. After characterizing the steady-state behaviour, additional experiments with cavitation were then performed using single-cycle pulses in an attempt to create the smallest, most precise bubble cloud possible while staying in the intrinsic threshold regime. A representative single-cycle pulse, as measured at the hydrophone, is shown inset into Figure 4.6 where the pulse has a fractional bandwidth of 59%. In initial single-cycle pulse experiments, a cavitation bubble cloud in water wasn't observed until reaching a minimum drive voltage of 173 V, which is due a single-cycle pulse not reaching the same peak amplitude as the 20 cycle pulse train as well as non-linear acoustic effects and reaching the 100% cavitation probability pressure threshold. A single-cycle generated bubble cloud can be seen in Figure 4.7.

This bubble cloud was generated in degassed, deionized water with a 6.8 MHz single-cycle, single-ended 173 V pulse at a 50 Hz repetition rate. A 26 gauge needle, nominal diameter 464 μm , can be seen in the image to provide scale for the bubble cloud which measures 124 μm diameter with a length of 263 μm . Imaging was

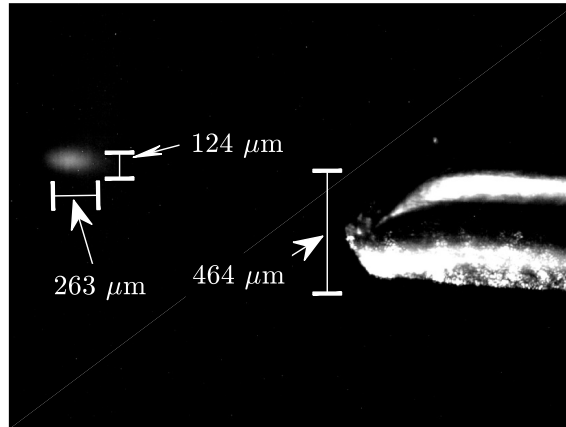


Figure 4.7: A cavitation bubble cloud is shown as a white spot here due to averaging of multiple camera frames to produce an image. The bubble cloud measures approximately $263\ \mu\text{m}$ in length, and $124\ \mu\text{m}$ in diameter. A 26 gauge needle with a nominal $464\ \mu\text{m}$ diameter is seen on the right for scale.

performed using a Zeiss Discovery.V20 Stereo Microscope and a Zeiss Axiocam ERc 5s digital camera (Carl Zeiss Microscopy GmbH, Jena, Germany) where the bubble cloud was illuminated perpendicular to the direction of imaging, and a camera exposure time of 400 ms was used for a single image, and 30 images averaged to recreate the full bubble cloud shape. Length and width were determined by a thresholding method, where the maximum brightness value measured at a representative area of background only was used as the threshold and pixels above this brightness in the bubble-cloud region were considered to be part of the bubble cloud. The widest possible values above this threshold along the x and y axes were used for bubble cloud dimensions. This imaging is easy to do while cavitation occurs in water; however, in tissue, visual imaging would be impossible at-depth, so the tool presented here can instead be modified with the addition of a central hole, allowing an ultrasound probe

through the center to image while ablation is being performed. We have created such a co-registered ultrasound device and present some initial results for this device in Section 4.4.

4.4 Co-registered Ablation and Imaging

To create a co-registered imaging and ablation tool, the focusing lens, which was shown in Figure 4.1, was modified to add a 4 mm x 4 mm hole through the center allowing an imaging tool to image the ablation area. In this work the imaging device, developed in-house, was a 40 MHz, 64-element phased-array transducer packaged in a 2.5 x 3.1 mm endoscopic form factor. This endoscopic phased array was fully characterized by Bezanson *et. al.* in 2014[12]. The imaging beamformer used was a sub-nyquist, variable sampling, high-frequency phased array beamformer presented by Samson *et. al.* in 2017 [13]. Figure 4.8 shows the ultrasound endoscope with a machined lens positioned at the end as was used during co-registered ablation.

For surgical applications, the device is mounted at the end of a hand-held tool for fast user guidance so that ablation points can be targeted on-the-fly if desired. Additionally, the tight lens focus and small ablation spot-size as well as the high-resolution endoscope imaging window means the device has potential for use in small animal studies where internal ablation, or highly targeted neural ablation with minimal tissue heating, may be desired. Figure 4.8 provides an idea of the orientation of

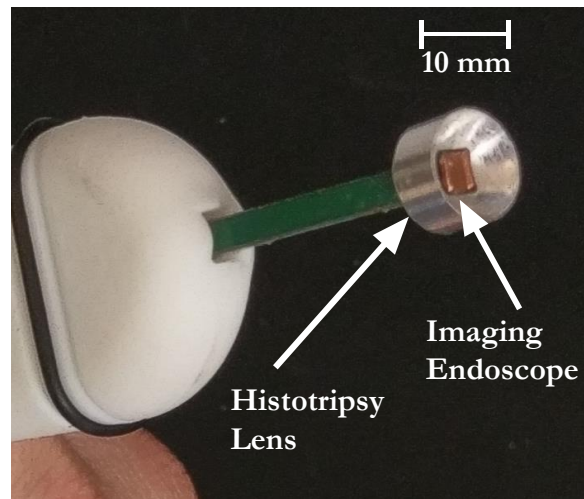


Figure 4.8: The histotripsy ablation lens here has a center-hole to allow an imaging tool to visualize the area in real-time during ablation. This particular endoscope is a 64-element, 40 MHz phased array endoscope designed and fabricated in-house[12].

the ablation lens relative to the endoscope. The final device design has the endoscope tip slightly recessed from the lens curvature so that the endoscope does not occlude the ablation tool while still having the ablation zone centered in the imaging window, and the lens-composite stack is encased to ensure the composite remains air-backed. Preliminary testing of the co-registered device found that, with the current drive electronics and the missing lens area needed to accommodate the imaging probe, a higher voltage was needed to consistently cavitate. Figure 4.9 demonstrates this need for a higher drive voltage with a plot of pressure vs drive voltage for the transducer with a hole in the center.

Similar to previous measurements, the transducer was driven with a 20 cycle pulse train at 6.8 MHz using a pulse-repetition frequency of 50 Hz. For the non co-registered transducer characterized in Section 4.3, pressure increased at a rate of 0.29 MPa /

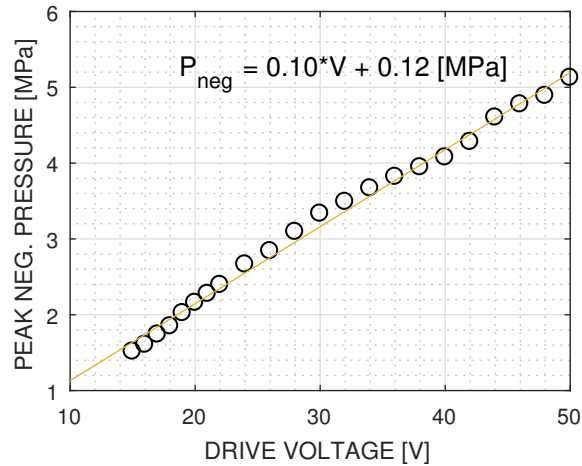


Figure 4.9: Using a hydrophone, the 10 mm, co-registered ablation transducer focal pressure was measured as a function of drive voltage. A linear relationship between pressure and drive voltage is seen from 15 V up to 50 V. At 50 V, initial evidence of cavitation at the hydrophone tip was seen and measurements were stopped.

Volt whereas for this co-registered device the pressure increases at a rate of 0.1 MPa / Volt. In practice, this made it difficult to cavitate in water for the co-registered device as the pressure is reduced by a factor of 2.9. This pressure reduction is large when considering the area lost by adding a 4 mm by 4 mm hole is only 20%; however, we believe much of the additional loss in pressure is due to energy lost into side lobes which are visible in the radial cross-section of Figure 4.11 as well as, potentially, error in machining of the lens curvature. Despite the loss in pressure, since the shock scattering cavitation threshold in fatty tissue (13.26 MPa at 1000 HZ pulse-repetition frequency [128]) is lower than the intrinsic threshold in water, this device is still a good candidate for targeted neural ablation since it can reach the shock scattering threshold for fatty tissue and the brain consists of a high percentage of fatty tissue. To test this, histotripsy cavitation was performed in ex-vivo chinchilla cerebral tissue

submerged in degassed, de-ionized water, the results of which are shown in Figure 4.10.

In Figure 4.10a, the highly specular tissue is the cerebellum granular layer, the large dark regions are the molecular layer, and within the granular layer can be seen thin dark tracts which are white matter. The ability to identify these regions using ultrasound is important for targeting specific parts of the brain. In Figure 4.10b, histotripsy ablation is in progress where the bright circular region between 7 mm and 8 mm depth is the bubble cloud in the process of ablating. In this case, ablation is performed by driving the transducer with a 6.8 MHz, 400 V, single-ended 10 cycle pulse train at a pulse-repetition frequency (PRF) of 1000 Hz. Above the bubble cloud, a channel can be seen from the cerebellum surface down to the ablation zone, where cavitation was initiated at the surface and then plunged into the tissue. The bright streaks in the image are electronic noise from the histotripsy pulser and can be removed by synchronizing the histotripsy pulses to occur between image lines. Using this device, ablations were repeatably performed on three separate brain samples, in both the cerebral cortex and cerebellum, ablating line cuts from the surface such as those seen in Figure 4.10, as well sub-surface volume removal such as those demonstrated in previous work using a 20 mm aperture co-registered device [96]. The total count of ablations was not recorded, but was in excess of two for line cuts to a depth of greater than 3 mm per brain sample, and in excess of five for sub-surface

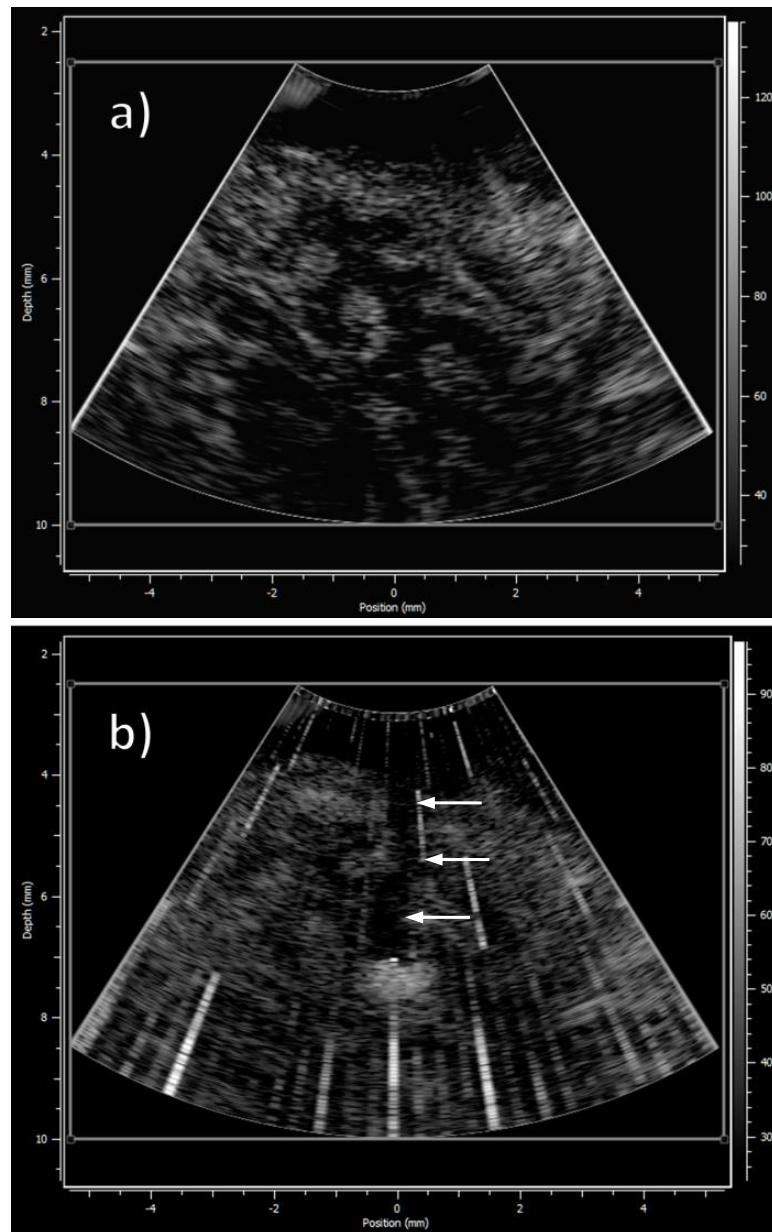


Figure 4.10: In the upper image (a), a Chinchilla cerebellum is imaged showing the molecular layer (dark layer), the granular layer (highly specular), and white matter tracts (thin dark lines in granular layer). In the lower image (b) which is of the same tissue slice, a histotripsy bubble cloud, visible as a highly specular region near the image center, has been plunged into the cerebellum. Both images were collected in real-time using a co-registered 40 MHz endoscopic phased array. The arrows in (b) point out the track followed by the bubble cloud, with the upper arrow pointing to the ablation entrance.

ablations per sample. In Figure 4.10b, ablation occurs only where targeted; however, at higher pressures it is possible that side lobes could reach cavitation pressures as well. To check for side lobes, the transducer pressure field was measured and is plotted in Figure 4.11 showing a map of the transducer pressure field with visible side lobes at ± 0.2 mm, 10 dB below the peak in the radial direction.

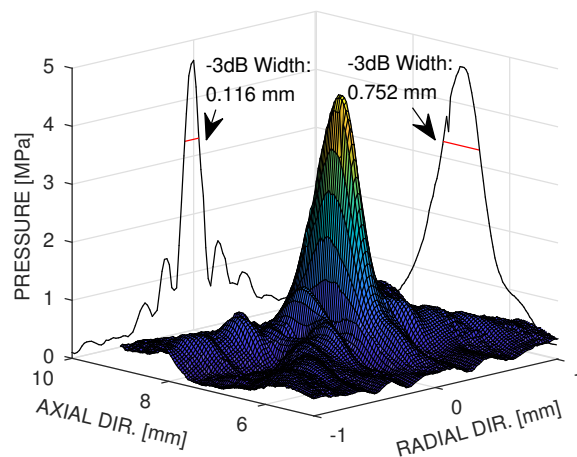


Figure 4.11: The co-registered transducer pressure field was measured centered at the focus, where the transducer was driven at 40 V with a 6.8 MHz, 20 cycle pulse. The acoustic waves are propagating in the axial direction. The focal -3dB width in the radial direction measures 0.116 mm, while the axial -3dB length is 0.752 mm.

It is important to keep these lobes below the pressure required to cavitate so, for this device, peak pressure should be less than three times the shock scattering threshold in the treated tissue. The -3dB radial beam width is measured at 0.116 mm and the focal length, or -3dB axial beam width, is 0.752 mm.

4.5 Future Work

The successful creation of this tool opens many future avenues of research. Future goals include further reduction in device size and optimization of the histotripsy transducer output as well as improvement of the driving electronics and measurements of the pressure field at higher drive voltages using a fiber optic hydrophone. The authors plan to begin small animal studies to determine ability of the device to be used in a hand-held manner, and additionally to evaluate the efficacy of using such a device in the treatment of tumor tissue in the brain. Examination of the KLM model results and potentially the creation of a finite-element model is further necessary to determine the cause of a 5 MHz composite having maximum power output at 6.8 MHz when assembled as described in Section 4.2.

4.6 Conclusion

This study has shown the design and testing of a small, 10 mm aperture ablation device which can create a histotripsy bubble cloud of sub-millimeter size. Furthermore, a co-registered imaging and ablation device has been presented which is capable of real-time tissue imaging and ablation. The simplicity of these devices allow the creation of multiple tools with minimum time and cost, while the demonstration of cavitation in water at a drive voltage of 173 V suggests driving the tool directly without matching circuitry or a transformer can keep the cost of the drive electronics low

as well. The material cost was estimated at \$92 USD for the transducer, and less than \$100 USD for the pulser, keeping the cost below \$200 USD excluding power supplies and function generator. Side lobes on the non-coregistered device are close to -20 dB and of -10 dB on the co-registered device suggest the probability of cavitation outside the focus is low, however it should be considered under high power applications. Additionally, a measured 59% one-way bandwidth for the non-coregistered device allows the device to operate with a single-cycle or two-cycle pulse, maintaining a tight focus. Overall, this work presents devices which show promise as a first step toward a fully endoscopic imaging and ablation histotripsy tool and can be easily fabricated by anyone who wishes to have a small, hand-held ablation ready device.

Chapter 5

Fabrication and Characterization of a 5 mm x 5mm

Aluminum Lens Based Histotripsy Transducer

Preamble

Chapter 5 presents work on creating a 5 mm by 5 mm aperture, histotripsy ablation transducer using an aluminum lens for focusing of the histotripsy. The work for this has been accepted for publication [129] in IEEE Transactions on Ultrasonics, Ferroelectrics, and Frequency Control and is presented here in the form in which it was submitted.

©2022 IEEE. Reprinted, with permission, from Jeffrey K. Woodacre, Thomas G. Landry, Jeremy A. Brown, Fabrication and Characterization of a 5 mm × 5 mm Aluminum Lens-Based Histotripsy Transducer, IEEE Transactions on Ultrasonics, Ferroelectrics, and Frequency Control, April 2022.

In reference to IEEE copyrighted material which is used with permission in this thesis, the IEEE does not endorse any of Dalhousie University's products or services.

Internal or personal use of this material is permitted. If interested in reprinting/re-publishing IEEE copyrighted material for advertising or promotional purposes or for creating new collective works for resale or redistribution, please go to http://www.ieee.org/publications_standards/publications/rights/rights_link.html to learn how to obtain a License from RightsLink.

5.1 Introduction

The development of new and novel surgical treatments can be a long and involved process often taking decades from initial investigation to inter-operative implementation. Histotripsy for example, despite immense promise in revolutionizing ablative non-invasive surgeries, has only recently reached clinical trials as a treatment for benign prostatic hyperplasia, liver cancer, and calcified aortic stenosis [130]. Since one of its earliest investigations being a 2004 study of cavitation ultrasound ablation of ex vivo porcine and in vivo canine tissues [8], research in the Histotripsy field has led to, over the almost two decades since, the creation of an extensive body of fundamental research into the use of histotripsy including the use of a range of transducers operating at 345 kHz [114], 500 kHz [70], 750 kHz, [9], 1 MHz [112], and 3 MHz [113], the consideration of transducer f-number and medium O_2 saturation on ablation shape and cavitation probability [114, 127], and a detailed examination cavitation initiation

pressure thresholds characterized by tissue elasticity [69]. In parallel to the fundamental work, a number of animal studies have been published, some of which include reporting on the efficacy of treating benign prostatic hyperplasia on a canine model [32, 33], treatment of hepatocellular carcinoma in a porcine model [34], thrombolysis in a porcine model [35], trans-cranial histotripsy through an excised skull cap [119] and porcine cerebral ablations through craniectomy window [36]. The above is only a sampling of studies and, despite the breadth of work already done, there is still a great deal of research and development potential within the histotripsy space. For neurosurgeons, the ability to ablate brain tissue in either a non or minimally invasive fashion is certainly of interest; however, there may also be some advantages in providing an endoscopic form-factor tool. Such a tool would resemble the hand-held tools, such as the Integra CUSA or the Stryker SONOPET, already used in the operating room as well as the tools attached to stereotactic robot system for targeted positioning. The CUSA and Sonopet are contact-based ultrasonic aspirators reliant on optical guidance for targeting and ablation. This reliance on optical guidance and having to ablate through healthy tissue can leave surgeons unable or unwilling to risk resections when tumors are intertwined with vasculature, or when a lack of precision may compromise functional areas of the brain. The motivation for this work is to demonstrate a device which could, with further refinement, be of clinical use by providing non-contact ablation at locations normally considered unresectable, especially

if co-registered with ultrasound imaging. Overall, we believe there is the potential for a range of histotripsy devices capable of operating over a number of frequencies, and in various sizes, powers, and depths to displace either the CUSA or Sonopet as the sole option for many tumor debulking scenarios.

Having a device capable of non-contact ablation while also having the ability to target small volumes of tissue with a high-precision could be the difference between ablating tumor and damaging sensitive tissue. Lin *et. al.* [113] were able to show that in the intrinsic histotripsy regime, where a one or two cycle pulse reaches the peak-negative pressure needed to generate cavitation events [131], sub-millimeter ablation was possible using a 3 MHz focused transducer. To ablate at even finer spacial scale it may be feasible to use a higher frequency device. However, the ablation rate and frequency-dependent absorption could make cavitation initiation difficult. Operating in the shock-scatter histotripsy regime, where cavitation occurs by reflected inversion of a non-linear multi-cycle pulse reaching pressures below the cavitation threshold [71], would lead to cavitation at a lower pressure due to the low stiffness of tissue in the brain, mitigating some of the difficulties in high frequency operation. Shock-scatter also benefits from a larger axial spot size by increasing the cycle number. It has been shown that cavitation initiation requires non-linearly higher drive levels as f-number increases from 0.5 toward 0.89 and, transducer dependent, can be difficult to achieve as f-number increases further [127]. With an endoscopic device, it is therefore

a design challenge to achieve an f-number with the ablation zone sufficiently outside of the aperture to be useful, but not so far away that non-linear acoustic effects make cavitation impossible. Having a lens made of a high speed of sound material, such as aluminum, could allow the curvature to be less drastic compared to plastics or epoxies, ensuring a smaller f-number comparatively. An aluminum lens would have an acoustic impedance of 17 MRayl which can match a properly designed PZT-5A-epoxy 1-3 composite where matching of composite to aluminum lens has proven an effective design in developing 10 mm diameter histotripsy devices [102]. At the endoscopic size, being able to deliver more power per unit of drive voltage may prove useful if some pressure overhead is needed, so a homogeneous porous ceramic designated Pz39 from Meggitt Ferroperm, having an acoustic impedance of 18 MRayl and a relatively high dielectric constant, is also being examined. Hard ceramics are not being considered as their dielectric constants are typically low, requiring higher voltage levels than soft ceramics to generate equivalent pressures while, additionally, the benefits from their high Q are mitigated by the epoxy fill in a 1-3 composite.

With the above in mind, the work presented in this article shows that the fabrication of a high-frequency 5 mm by 5 mm aluminum-lens based histotripsy device with a 6 mm focus is possible, and that the device can be capable of both cavitation free-field in water while also performing sub-surface neural ablation of rat tissue in vivo. Section 5.2.1 describes the materials and equipment used in fabrication and assembly

for each device with electrical impedance measurements after assembly. Section 5.3.2 provides data on the pressure per volt for each device as well and their measured pressure fields and comparison with simulated results. Section 5.3.3 examines pulse settings used for cavitation in free-field as well as in vivo, and presents preliminary results of an in vivo rat ablation experiment. Section 5.4 discusses the results presented and future directions for the work while Section 5.5 summarizes the presented work.

5.2 Methods

5.2.1 Fabrication and Assembly

A cross-sectional schematic of the final 5 mm x 5 mm square lens histotripsy device assembly is shown in Figure 5.1 along with a photograph of the aluminum lens on a finger tip.

The lens is machined on a computer-numerically controlled mill with an elliptical curvature instead of a spherical curvature to avoid potential spherical aberrations at low f-number, a situation that can occur when tightly focusing a spherical lens where all points on the lens surface do not focus to the same location. Thus, the use of an elliptical curvature ensures acoustic plane waves emitted from the piezoelectric element arrive at the focus with zero phase delay across the entire wave. The focal distance is designed to be 6 mm from the deepest point on the lens curve, giving a

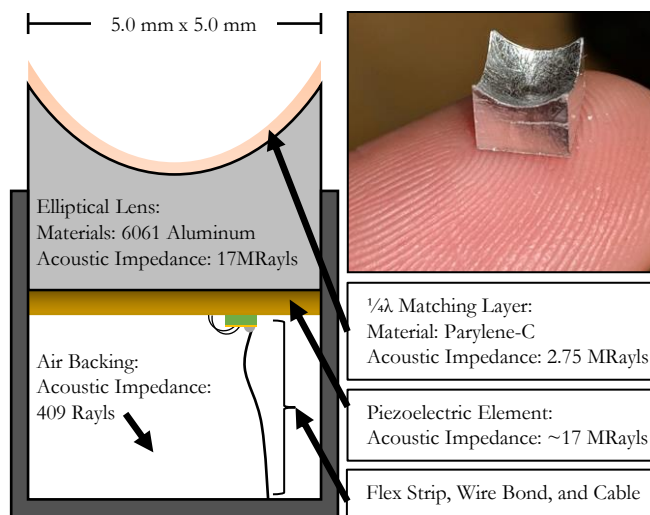


Figure 5.1: On the left, a transducer schematic cross-section shows an air-backed piezoelectric element, in this case either a 1-3 PZT-5A-epoxy composite or Pz-39, with an elliptically machined aluminum lens topped with a quarter-wavelength parylene-C matching layer. A 1.0 mm x 0.5 mm piece of flexible circuit board is adhered to the back with cyanoacrylate glue and electrically connected to the piezo via wirebonds. A wire is soldered to the piece of flexible circuit for external connection. Ideally, the piezoelectric element would have an acoustic impedance matching that of aluminum - 17 MRayl. The inset image seen top-right is of the final machined lens on a finger-tip for scale.

focal distance from the top of the lens of 4.36 mm. The f-number is calculated to be $6/5 = 1.2$. The lens material, 6061-T6 aluminum, was chosen so that a piezoelectric element could be made to match the lens acoustic impedance, ensuring complete transfer of energy from the element into the lens on each cycle. For this work, two piezoelectric materials with a close acoustic impedance to aluminum are compared: a 1-3 composite of PZT-5A with a 40% volume fraction and measured 14 MRays acoustic impedance (Smart Material Corp., USA), and Ferroperm Pz-39 - a reported 18 MRayl porous structure ceramic (Meggitt A/S, Denmark). The dimensions, mass,

and anti-resonance frequency of a representative piece of Pz-39 are measured to calculate the actual acoustic impedance for the received batch of material.

On the face of the lens is a quarter wavelength matching layer of Parylene-C deposited using a Specialty Coating Systems Labcoter 2 Parylene Deposition System. Parylene-C was chosen as its acoustic impedance of 2.75 MRayl [132] matches reasonably between aluminum lens and water. To find the matching layer thickness, one must first consider that previous work has shown that after bonding composite to lens, the maximum acoustic output occurs at a higher frequency when compared to the composite resonance [102]. This optimal output frequency is partially fabrication dependent and changes based on how thin the epoxy bonding layer is between the piezoelectric element and lens material and, in general, the maximum acoustic output frequency shifts back to the composite design frequency as the epoxy bonding layer thickens. For this device, the optimal output frequency was found to be 5.8 MHz, and therefore the desired quarter wavelength matching layer thickness for Parylene-C is 92 micrometers. The final thickness was measured to be 89 micrometers.

Assembled 5 mm x 5 mm lens devices can be seen in Figure 5.2 where the lens is on the top, a casing designed and printed using the Formlabs Form 2 3-D SLA printer (Formlabs, Inc., Somerville, MA, USA) houses the transducer, and an SMA connector on the bottom allows cabling to the pulser. Internally, a small strip of copper electroded flexible circuit board measuring 1.0 by 0.5 mm square (2% of the

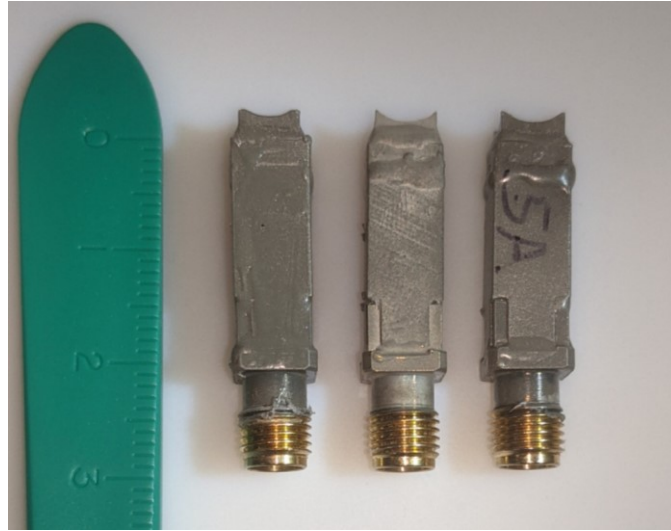


Figure 5.2: Two devices fabricated using Pz-39 (left, center) and one using PZT-5A composite (right). An SMA connector on the rear allows cabling connection to a pulser.

total piezo surface area) is adhered to the air-backed side of the piezo element using cyanoacrylate glue, wirebonded to the element electrode using a wedge bonder and 20 μm aluminum wire. The circuit board is attached to the SMA connector high-voltage pin via a solid wire soldered between the two. This technique of wirebonding to the piezo was preferred over soldering to avoid damage to the electrode and local depoling of the piezo. The lens is grounded via a sputtered electrode over the entire outer surface of the device up to the SMA connector, a method which maintains a small form-factor by avoiding any mechanical or solder connections on the side of the lens while allowing batch processing of multiple devices at once. Overall, the device measures 30 mm long and, has a cross-section of 6.6 mm, larger than the 5 mm lens due to the casing and epoxy sealant.

Once assembled, the electrical connectivity and quality of bonding between the piezoelectric and lens is confirmed through electrical impedance measurements in the range of 2 MHz to 10 MHz.

5.2.2 Acoustic Field Characterization

For a histotripsy transducer, a comparison of focal pressure as a function of drive voltage, in this case as measured at the supply, for different devices can help to estimate the lowest possible drive level needed to reach cavitation pressures. Using a Onda HGL-0085 capsule hydrophone (Onda Corp, Sunnyvale, USA) with a 5.8 MHz sensitivity of 32.86 mV / MPa, the peak-to-peak output focal pressure as a function of drive voltage was measured for the PZT-5A and Pz-39 transducers. The peak-to-peak pressure data was collected by pulsing each transducer to steady state with a negative uni-polar square-wave 10 cycle, 5.8 MHz pulse at a 1 kHz pulse-repetition rate (PRF) resulting in a duty-cycle of 0.17%. The data was averaged over 200 repetitions and drive voltage ramped from -0.5 V to -10 V in 0.5 V increments.

Using the same Onda capsule hydrophone and an XYZ positioning stage, with the transducer transmitting along the Z motion axis, the steady-state pressure field normal to the transmission axis and through the focal plane was measured by positioning the hydrophone at focus and stepping the transducer in the X and Y directions over a 2 mm by 2 mm focus-centered grid with a grid spacing of 25 μm . Additionally, the

transducer steady-state pressure field was measured in a line along the transmission axis through the focus by placing the hydrophone at the focus and then moving along a focal-centered path measuring 4 mm in length in $25 \mu\text{m}$ increments and collecting peak pressure measurements at each step.

Both the pressure field in the focal-intersection plane and the axial pressure plot are compared to simulated pressure fields produced using the k-Wave Toolbox [101] in MATLAB 2020b [133]. The simulated pressure field was generated by defining parts of the kWave grid representing the lens as aluminum and the rest as water. The grid spacing was $25 \mu\text{m}$, and a continuous-plane wave pressure source was generated on the back of the lens at 5.8 MHz. The simulation time step was 10 ns.

Nonlinear acoustic simulations were also performed using HITU Simulator v2.0, an open-source high-intensity therapeutic ultrasound MATLAB package developed at the United States Food and Drug Administration [134]. These simulations were intended to confirm that the field becomes highly nonlinear - a requisite of shock-scatter histotripsy. The simulation is 2D circularly symmetric, so the square lens transducer is approximated as a curved bowl with an aperture area of 25 mm^2 , and a geometric focus of 6.0 mm. The transmit power level in the simulation is determined by equating measured transducer focal pressures for the Pz-39 device at low, known drive voltages to simulation focal pressures. The simulated transducer was pulsed at 5.8 MHz continuous-wave with output power equivalent to drive levels of: 10 V, 30 V,

50 V, 70 V, 90 V, and 110 V. Above 110 V the simulated pressure field shows unstable results, and computer hardware had insufficient memory to expand the computational grid. Only the Pz-39 device was simulated as the identical geometries between the PZT-5A and Pz-39 devices ensures their simulation results would be scaled versions of each other.

5.2.3 Drive Settings and In Vivo Ablation

Drive settings to induce cavitation in water were determined experimentally by ramping the pulser voltage until free-field cavitation could be visually observed. In brain tissue, ultrasound imaging feedback was used to determine if cavitation was occurring.

For the in vivo experiment, a young adult male Wistar rat was used. The procedure was approved by the Dalhousie University Committee on Laboratory Animals. The rat was anesthetized with isoflurane in O₂ flowing at 1.5 L/min (4% induction, ~2% maintenance) and the head was fixed in a stereotaxic frame with ear bars. Local analgesic (0.25% bupivacaine, ~0.6 ml) was injected into the scalp, and atropine sulfate was given (0.06 mg/kg) to reduce airway secretions. Body temperature was maintained at 37°C with a homeothermic heat pad, and breathing rate was monitored by the signal from a cantilevered bimorph piezoelectric actuator under the chest.

The scalp was incised and a 13 mm circular craniectomy was performed, centered on midline and bregma -4.1 mm, and extending down the side of the skull several mm.

The dura mater was left intact. The histotripsy device and an ultrasound imaging probe were clamped to a stereotaxic micromanipulator and positioned orthogonally to each other. The position of each was first adjusted in water during imaging and cavitation to ensure the bubble cloud was positioned in the center of the image window. The manipulator was then moved to place the co-registered devices over the brain. A schematic of the overall setup is shown in Figure 5.3. Ultrasound gel was used as an acoustic coupling medium. A rat brain atlas was used as an anatomical guide [135] with the final treatment position being roughly bregma -6 mm. After histotripsy testing was finished, the rat was immediately sacrificed with an overdose of sodium pentobarbital.

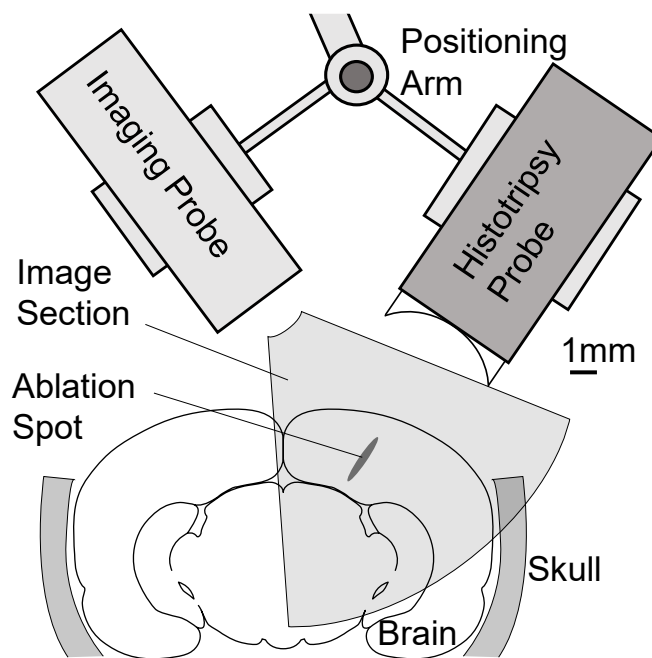


Figure 5.3: A schematic of the in vivo experiment shows the imaging probe and histotripsy probe co-registered and targeted through the craniectomy opening. The devices are attached to a motorized positioning arm for targeting.

The ultrasound probe which provided real-time imaging of the histotripsy treatment was a 30 MHz 64-element phased array probe fabricated as published by Bezanon *et. al.* [12] connected to an in-house developed beamformer system detailed in Samson *et. al.*[13] which was modified to trigger histotripsy pulses only between image lines at a PRF of ~ 1 kHz. Ablation was targeted at a depth of 3 mm and maintained for 12 seconds until the bubble cloud size visibly reached steady-state. Custom Power Doppler firmware, as presented by Landry *et. al.* [136], was used on the beamformer to show blood-flow within the brain, and to provide improved cavitation feedback compared to a standard B-mode image [137] by temporally detecting rapid changes in speckle and applying a color map overlay based on these changes.

5.3 Results

5.3.1 Fabrication and Assembly

It has been shown previously [102] through KLM simulations and device measurements that if the bonding layer between piezo and aluminum lens is thin then the typical single resonance-antiresonance behavior seen in impedance measurements of unloaded piezo elements is lost, and instead replaced with a heavily damped oscillatory impedance magnitude and phase which shows little or no response around the original resonance. This multimodal response is due to the curved geometry of the lens bonded to the piezo element. As the bonding layer between piezo and lens grows

in thickness, is uneven, or the piezo is partially delaminated from the lens, the electrical impedance tends to return to the typical undamped behavior. Figure 5.4 shows the electrical impedance measurements for the 5 mm x 5 mm lens devices where a lack of single mode resonance-antiresonance behavior in the PZT-5A (solid-black) and the Pz-39 curves (dashed-red) suggest bonding was successful.

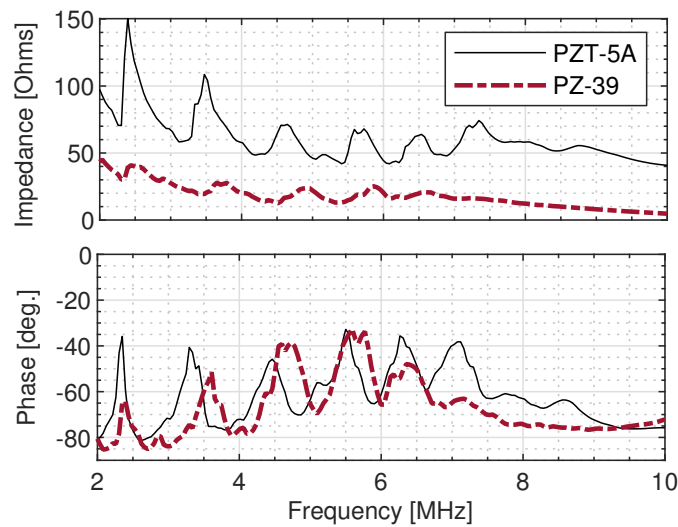


Figure 5.4: The electrical magnitude and phase for a PZT-5A transducer (black solid lines) and a Pz-39 transducer (maroon dashed line) are shown after the lens and piezo are bonded which adds a number of damped resonances.

For the batch of Pz-39 used in this work, a piece with a resonance peak at 1.1825 MHz, measuring 15.78 by 15.80 by 1.532 mm with a mass of 2.57 g was calculated to have an acoustic impedance 24 ± 0.1 MRayls using the formula $Z = \rho c = \rho(2tf_p)$ where t is the thickness, and f_p is the peak resonance frequency and ρ is the density.

5.3.2 Acoustic Field Characterization

The peak-to-peak pressure versus voltage data for the Pz-39 and PZT-5A devices is plotted in Figure 5.5.

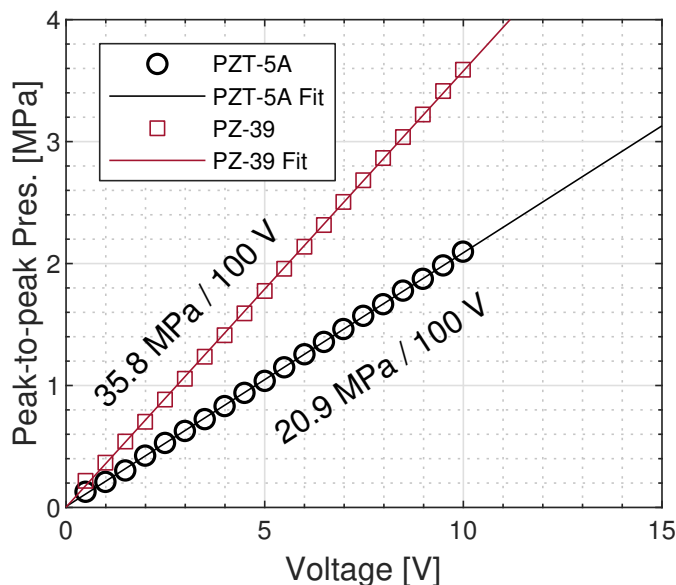


Figure 5.5: The peak-to-peak focal pressure vs drive voltage for a 5 mm x 5 mm lens PZT-5A composite transducer is plotted in black with a linear fit, showing a pressure increase of 20.9 MPa / 100 V in the low-voltage regime. For the Pz-39 transducer, plotted in red, a linear fit shows a pressure increase of 35.8 MPa / 100 V.

It was found that the peak-to-peak pressure increased at a rate of 20.9 MPa / 100 V for the PZT-5A device and 35.8 MPa / 100 V for the Pz-39-based transducer. The ratio of these pressure curve slopes is 1.71. Extrapolating the pressure curve and assuming symmetric pressure fields, a drive voltage of ~ 145 V for the Pz39 device, and 250 V for the PZT-5A device should be needed to reach a peak-negative pressure of 26.1 to 27.9 MPa, the reported intrinsic threshold of water at 3 MHz [114]. This a linear voltage extrapolation provides a starting point for finding cavitation drive

level.

Focal pressure field scan data presented in Figure 5.6 shows the -3 dB width is 0.31 mm in both the X and Y directions, while the full-width at half-maximum (FWHM) measures 0.43 mm in each axis. Additionally, side lobes are symmetrically positioned about the focal peaks in the X and Y planes measuring no more than 20% of the peak pressure. Note, the lack of full circular symmetry for the side-lobes, visible in the surface map as dips in pressure out of the X and Y focal planes, is caused by the square lens aperture. The FWHM for the simulated data is 0.42 mm and the overall shape matches closely to measured values with notable deviations of between 4 and 5 dB in the side lobe amplitudes.

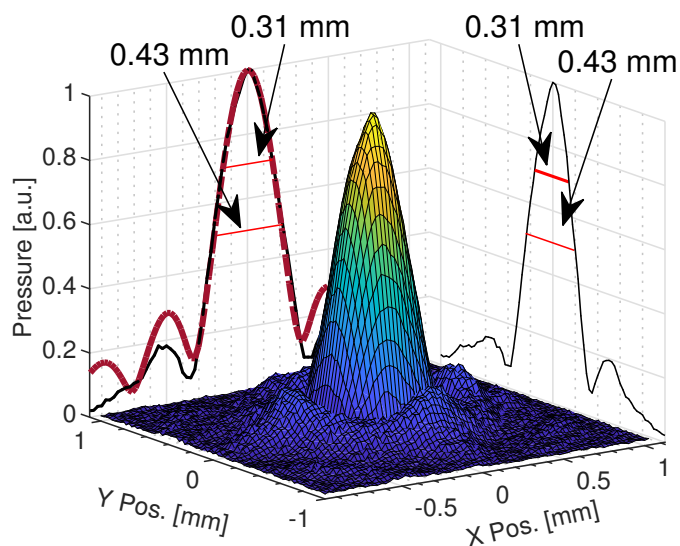


Figure 5.6: A surface plot of the measured pressure field in a focal-intersection plane normal to the direction of acoustic propagation shows a -3 dB width of 0.31 mm and a FWHM of 0.43 mm in both the x-direction and y-direction. Side lobes are seen symmetrically positioned about the peak which measure, at most, 20% of the peak pressure. The red dashed line plotted along the x-position versus pressure axis shows a kWave simulated pressure measurement, where the FWHM is found to be 0.42 mm in both the x and y-directions.

The axial pressure along the direction of acoustic propagation intersecting the focus, both measured and simulated, is presented in Figure 5.7.

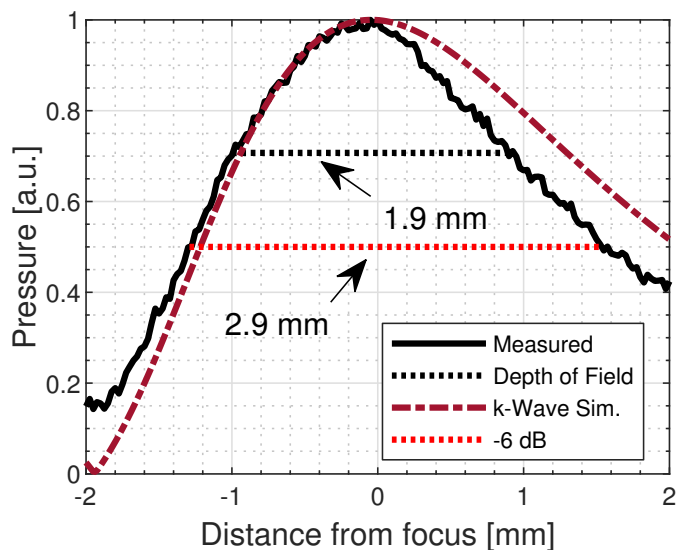


Figure 5.7: The normalized pressure measured along the symmetry axis of the transducer through the focus, along with a k-Wave simulated pressure along the same axis. The measured -3 dB depth of field for our transducer was found to be 1.9 mm, while the simulated -3 dB depth of field is 2.1 mm. Measured -6 dB beam length was 2.9 mm.

Along the central transducer axis, the normalized pressure plotted as a function of distance from focus shows that the -3 dB pressure drop ranges from -1 mm, which is closest to the lens, to 0.9 mm further out in the pressure field for a depth of field length measured to be 1.9 mm. The measured -6 dB beam length was 2.9 mm. Given the depth of field is larger than the beam width, it is expected that ablation with this transducer will also produce tissue damage in an axially elongated shape if allowed to ablate for a long enough period. The simulated k-Wave pressure along the focal axis is plotted as a dashed red line and has a -3 dB length of 2.1 mm - 0.2 mm larger

than the measured value.

The simulated nonlinear peak positive and peak negative pressure curves in Figure 5.8 show a progression from a relatively symmetric pressure field at the 10 V drive level, where the peak positive pressure is 1.86 MPa and the peak negative is -1.7 MPa, to a highly asymmetric pressure field where the peak positive pressure measures 46.2 MPa and the peak negative pressure is -13.8 MPa.

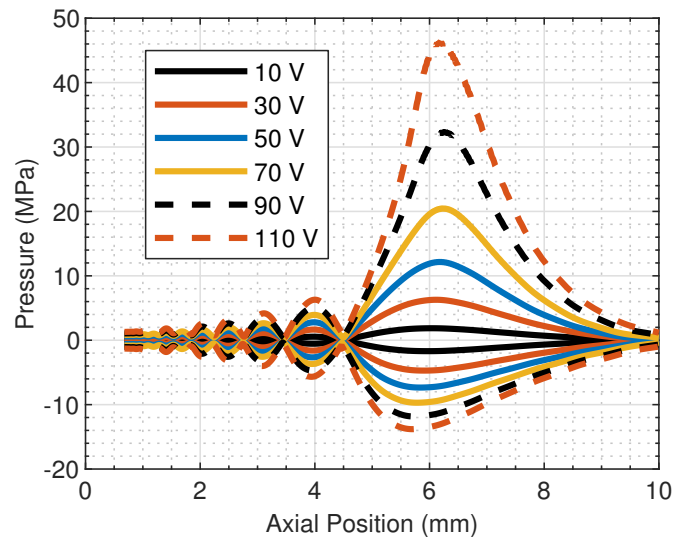


Figure 5.8: The axial peak positive and negative pressures for a 6 mm focused transducer at simulated drive levels of 10, 30, 50, 70, 90 and 110 V show the progression of pressure asymmetry as the field becomes nonlinear.

5.3.3 Drive Settings and In Vivo Ablation

For the PZT-5A device, no drive level resulted in free-field cavitation in degassed water. Using the pulse settings described in Section 5.2.2, the PZT-5A transducer was pulsed directly up to a drive level of 500 V, the maximum level of the pulser, without observing a bubble-cloud. Previous work found that using a 5 m length of

50 ohm RG174/U coaxial cable could act as a series tuning element for the 5 mm by 5 mm PZT-5a device, effectively boosting the drive voltage across the piezoelectric by a factor of 1.6 [138]. Using this 5 m cable, the drive voltage on the transducer was increased to 600 V; however, no cavitation event was observed and afterward the device was no longer capable of cavitation against a solid surface. After pulsing at 600 V, a change in the device impedance was measured - shown in Figure 5.9 with the magnitude shifting upward by 20 to 25 ohms and notable peaks appearing at 6.4 and 7.2 MHz.

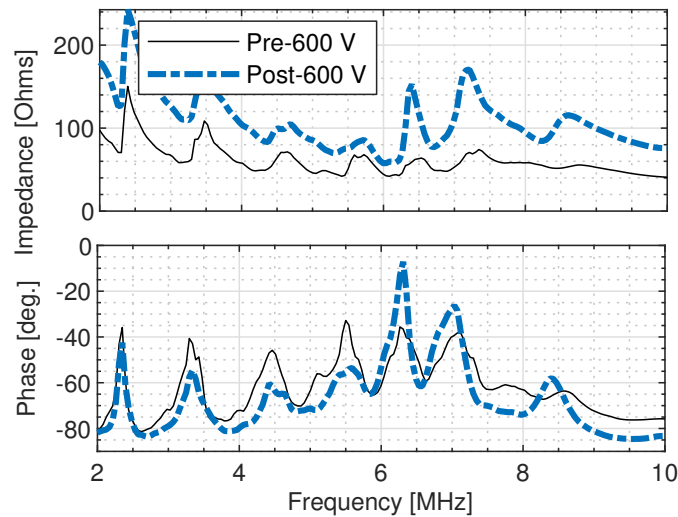


Figure 5.9: After driving the PZT-5A device to 600 V some resonance behaviour seen as a spike in phase at 6.2 MHz is observed, while a shift in the impedance magnitude suggests a drop in the clamped dielectric as a whole.

For the Pz-39 based device, a drive level of 220 V and the same settings as above resulted in free-field cavitation in degassed water. Given the results presented in Figure 5.5 it was expected that a drive level 1.71 times greater than that of Pz-39 - i.e. 372 V - would be needed for the PZT-5A device to reach the cavitation threshold.

Since the PZT-5A based device was unable to cavitate free-field, no attempt was made to use it on a live subject. For in vivo treatment, ablation settings were as used in the degassed water, however, drive voltage had to be increased to 280 V for ablation to occur. An example B-mode image from the experiment is shown in Figure 5.10 where the B-mode image shows the right side of the brain near bregma -6.0 mm during ablation with the cortex, midbrain, and midline labeled.

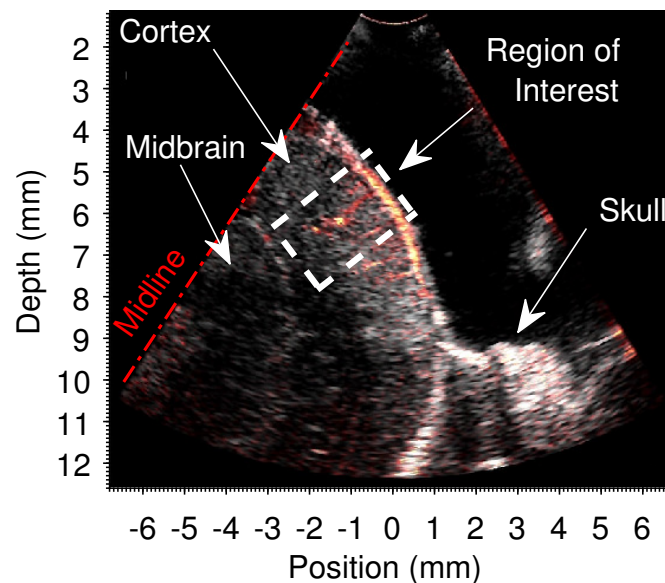


Figure 5.10: A B-mode image taken on the right side of the brain near Bregma-6.0 mm during histotripsy treatment shows the bubble cloud as a small bright spot within the labeled region of interest. The brain midline, cortex, midbrain, and edge of the skull are all indicated.

Power Doppler provides imaging of blood flow from the brain surface inward toward the cortex through a number of small vessels. The bubble cloud can be seen as a bright point centered within the region of interest, marked by a dashed-line box. To examine how the ablation progresses with time, Figure 5.11 provides a pre-ablation

through post-ablation time-series of B-mode image frames with Doppler overlay rotated and expanded from the region of interest in Figure 5.10. The frame times are individually labeled and referenced with respect to the start of ablation at time zero (0).

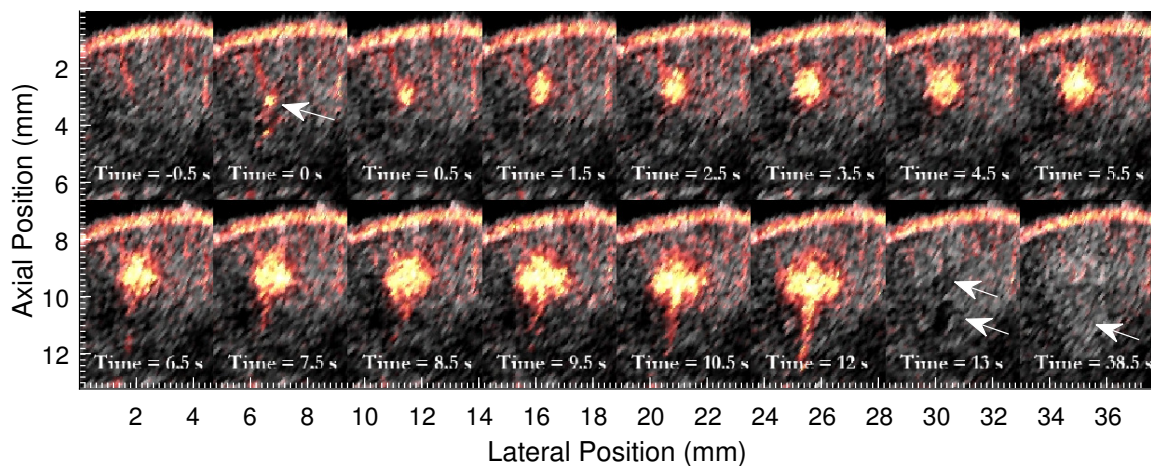


Figure 5.11: A temporal progression of B-mode images with Power Doppler overlay focused on the ablation region from Figure 5.10 shows that from time $t = 0$ s, when ablation is initiated, to time $t = 12$ s, just prior to ablation cessation, the ablation zone grows, leaving an anechoic region indicated in frame $t = 13$ s. At time $t = 38.5$ s, 25.5 s after stopping treatment, the anechoic region has regained specularity.

In the time $t = 0$ s frame a white arrow indicates the initial bubble cloud site location, measuring 0.4 mm both laterally and axially, which appears bright in the Power Doppler image. The ablation size progresses with a visual asymmetry in size starting near $t = 6.5$ s and reaching a maximum of 1.9 mm laterally and 3.4 mm axially at time $t = 12$ s just prior to the end of treatment. After treatment an anechoic region is observed which, by time $t = 38.5$ s, has filled in with a specular fluid.

5.4 Discussion

The impedance curves after bonding show that the piezo and lens were well bonded, and it is believed a relative estimate of the pressures between devices can be extracted from the impedance data presented in Figure 5.4. To first approximation, one can guess that the Pz-39 based device will deliver more pressure strictly due to its lower overall impedance magnitude, but, this does not account for power factor or how much real power is delivered to the device itself. For a numerical estimate of the pressure ratio, in-house Krimholtz-Leedom-Matthaei (KLM) [139] code previously developed for work on 10 mm aluminum histotripsy lenses [102] was used. With KLM code, which can simulate the composite, monolithic piezoelectric, and lens as a bulk material with effective properties [120, 121], it was found that at the maximum pressure output frequency of 5.8 MHz the Pz-39 device generated 1.78 times more pressure than the PZT-5A composite-based device. Interestingly, by comparison the ratio of the measured pressure curve slopes in Figure 5.5 is 1.71 - a less than 4% difference from the estimated pressure ratio based on KLM modeling. This result could be useful for determining pressure output of future devices and should be tested across multiple devices and piezo materials to better confirm accuracy of such an estimate.

Even with the pressure gained by the use of Pz-39, a device at this size, frequency,

and f-number seems to push the limits on fabrication and materials where small variations can be the difference between reaching the cavitation threshold. One simple change to improve pressure output would be to address the mismatch of acoustic impedances between lens and piezo elements. The lens, composite, and porous materials have impedances of 17, 14, and 24 MRayls respectively, resulting in pressure transmission coefficients of 0.90 between the composite and lens and 0.83 between porous material and lens. It is not expected that achieving a transmission coefficient of 1.0 would directly gain 10% and 17% in pressure for each material respectively, but modeling through either KLM or FEM could be used to determine if the output pressure is significantly improved. The composite mismatch could be addressed by increasing the volume fraction, but the porous material would need the purchase of a batch more closely matching the reported acoustic impedance of 18 MRayls.

Some differences between measured and simulated pressure fields were noted in Figures 5.6 and 5.7. Within the k-Wave simulation it was found that a discrepancy of the magnitude seen in Figure 5.7 would require an alignment error of 5° between the transducer and the motion stage Z-axis, but this would have been a noticeable misalignment it is not believed to have been the sole contributor. Instead, discrepancies between simulation and measurement for both Figures can likely be explained by a combination of imperfect machining of the lens, internal reflections in the lens influencing the pressure field, and partially through a mis-alignment of the transducer

which would amplify errors in the axial direction as the axial -6dB length measures 6.7 larger than the radial FWHM. The side-lobe pressures remained relatively low and may not be of concern during ablation as it is well below the cavitation threshold. Still, it was important to quantify these off-axis pressures to ensure there would be no off-target bubble clouds generated outside the desired treatment zone.

The non-linear pressure field simulations could not cover the drive levels required for cavitation due to computational memory limitations in creating a fine enough grid to avoid aliasing of spatial and temporal harmonics, but the results of Figure 5.8 do confirm a strong pressure asymmetry exists well below the 220 V level needed for cavitation. It is unclear from the simulation if peak-negative pressures needed for intrinsic threshold histotripsy could be reached. It is recommended that future work measures the transducer pressure field with a hydrophone capable of operating at much higher pressures to provide a comparison between simulation and experiment in the non-linear regime.

In practice, the intrinsic threshold needs to be exceeded to consistently produce a bubble cloud, and a linear approximation does not account for non-linear acoustic effects which present themselves at higher pressures and for f-number devices even in the 0.5 to 1 range [127], so it was not expected that the linear extrapolation of data from Figure 5.5 would provide an accurate cavitation drive level. Nevertheless, the 5 mm by 5 mm PZT-5A device being unable to cavitate in water was unexpected

as extrapolation of the data in Figure 5.5 suggests drive levels of 370 V should have provided a pressure equivalent to the Pz-39 at 220 V. The PZT-5A device was pushed to 500 V successfully, but when driven to 600 V could no longer cavitate against a solid surface - something this device was, and most histotripsy devices are capable of at drive levels well below the free-field cavitation threshold. This initial inability to cavitate at drive levels up to 500 V could have been caused by non-linear properties of soft ceramics or saturation of the piezoelectric, although, partial delamination of the matching layer from lens cannot be ruled out. We are confident, given no change in electrical impedance after cavitation testing up to 500 V drive levels that the cause was not due to delamination of the piezoelectric from the lens at that point, however, after pushing the device to 600 V an impedance change, seen in Figure 5.9 was noted. The shift upward indicates a reduction in the clamped dielectric, and the inclusion of a phase spike at 6.2 Mhz indicates some initial delamination of piezo from lens. The authors believe a more rigorous study and breakdown of multiple devices driven to destruction could lead to insight as to the exact failure mode, however, this study is outside the scope of the current work.

Despite issues with the PZT-5A device, the ability of the Pz-39 device to cavitate both free-field and in vivo shows promise for the material itself and the overall transducer design. However, it can not be over-stated how much the material properties of the piezoelectric, the pulse characteristics, and the machining quality of the lenses

play a role in the device success. In previous work a composite of CTS 3257HD, a high-dielectric material, was made and tested on a 5 mm by 5 mm lens[140]. It was abandoned as a material for histotripsy due to rapid degradation of the transducers when driving at cavitation voltages. A similar behavior was observed for Pz-39 based devices when driven single-ended above 300 V, as some transducers could lose their ability to free-field cavitate after only operating for minutes. The cause seems to be breakdown of the ceramic material and, whether electrical or mechanical, this requires further investigation to determine if solutions such as driving the device bi-polar to avoid electrical breakdown, backing to reduce internal stresses, or reducing overall Pz-39 drive voltage by attaching a separate pump transducer to boost pressure such as was done by Mallay *et. al.*[141], may avoid damage to the piezo element.

To account for the difference between the free-field cavitation threshold in water and the increase to 280 V needed for consistent cavitation in brain, the acoustic properties of the tissue must be considered. Unfortunately, the neurological tissue cavitation threshold has not reported in rodent models. The cavitation threshold in a sheep brain was found to be lower than degassed water, with 22 MPa guaranteed to cavitate at 660 kHz[142]. The threshold for some tissues was found to increase by a few MPa as frequency increases from 500 kHz to 3 MHz [114], so we will assume the threshold in brain is somewhere in the range of 24 to 26 MPa, slightly below but very close to that of water. The best attenuation coefficient estimate we could find is for

mouse brain, measuring 30 Np/m, or 0.26 dB/mm at 6 MHz [143]. Ablating 3 mm subsurface would then lead to a 9.4% pressure drop in tissue. With our upper estimate of brain cavitation threshold, a 240 V drive level should have caused cavitation in the brain since 220 V was the free-field drive level needed in water. The additional 40 V drive increase required could be caused by reflection at the gel-brain interface or from non-linear absorption, meaning higher harmonics which would normally contribute to shock-scatter histotripsy are being preferentially attenuated due to the attenuation coefficients linear frequency dependence. Though we did check for visible bubbles with a surgical microscope prior to device placement, there is also the possibility that small bubbles in the coupling gel caused a reduction in focal pressure due to scattering.

After ablation, an arrow lower than the center of the power doppler signal from previous frames indicates an anechoic region in the $t = 13$ s frame of Figure 5.11. Previous work on imaging ex vivo tissue with high-frequency ultrasound during ablation has shown this anechoic region to be where tissue has been liquified[98, 102] and the region remained anechoic indefinitely. For this in vivo experiment the anechoic region becomes specular between $t = 13$ s and $t = 38.5$ s - potentially as the volume is flooded with blood. Prior to this change conservative visual estimates of where the tissue transitions from specular to anechoic measure it to be 1.0 mm axially and 0.5 mm laterally. Note, this is smaller than the largest power doppler cloud size seen in

the $t = 12$ s frame suggesting power doppler may overestimate ablation size. Overall, the change from anechoic to specular and the apparent mis-match between power doppler and ablation locations suggests it is necessary to perform a more in-depth multi-animal study with sectioned and stained histology slides to compare how power doppler signal correlates to ablation in the brain and what the ablated volume cellular contents are post-treatment. This future study will be especially important given the need for precise and accurate ablations.

Successful in vivo treatment with this device means it could quickly and easily be adapted to a number of pre-clinical experiments where tight, precisely targeted ablations are needed and a co-registered imaging device can be utilized as a feedback mechanism. For use as a surgical tool, additional work on examining the effects of ablation parameters including PRF, pulse number, and applied time need to be performed in conjunction with sectioning and staining of the ablated area to ensure targeting was accurate and collateral damage was minimal. It may be possible to consistently provide sub-millimeter ablations without using ultrasound feedback if a stereotactic surgical robot can position the transducer accurately, provided improved treatment timing estimates can be established.

5.5 Conclusion

In this work, a 5 mm by 5 mm aluminum lens based device operating at 5.8 MHz using Pz-39 as the active element was demonstrated to perform shock-scatter histotripsy both free-field in water and in vivo within a rat model. Monitoring of bubble cloud initiation and continued cavitation could be accomplished using power Doppler and, post ablation, treated volume could be estimated and observed real-time with B-mode imaging of an anechoic zone. Overall, the successful in vivo ablation of tissue provides a stepping stone for a number of further studies on not only pulsing parameters for ablation size and shape, but specific treatments in animal and eventually human models.

Chapter 6

A Fresnel-based High Frequency Histotripsy Transducer for Pre-Clinical Applications

Preamble

Much of the previous work has focused on minimizing a transducer for neurosurgery, specifically treatment of cancer, but, testing of cancer treatments often begin in pre-clinical in-vivo or ex-vivo trials. Chapter 6 presents work on a gel-coupled flat-aperture 15 mm diameter histotripsy device with co-registered imaging. The work is formatted for publication and, as such, has some repeated content from the background with project specific details.

6.1 Introduction

Using animal models to bridge the gap between bench-top experiments and human trials is commonplace in today's medical research. Some examples of animals used in cancer treatment include, pig models for intestinal cancer [144], canine models for soft tissue sarcomas, osteosarcomas, and lymphomas [145], and the VX2 rabbit

model for hepatocellular carcinoma [146] among others. However, by far the most used animal model in modern science is the mouse. Whether due to their low cost, ease of handling or relatively simple ability to introduce genetic modification, the murine model is often the starting point for researchers moving past the petri dish or the ex-vivo regime to in-vivo experiments.

Histotripsy - a non-thermal ultrasound tissue ablation technique, has been explored in animal models for years with treatments such as ex-vivo renal ablations in rabbits [32], in-vivo ablation of benign prostatic hyperplasia in a canine model [32, 33] and hepatocellular carcinoma on a porcine model [34], thrombolysis in a porcine model [35], as well as boiling histotripsy (BH) ablation of in-vivo porcine liver and kidney tissue [42] to name a few. A number of experiments on murine models have also been performed including treatment of subcutaneous tumor models using BH [40], BH treatment of renal cell carcinoma[41], histotripsy on hepatocellular carcinoma [81], and immunotherapy enhancement through combination with histotripsy [82]. However, the relative number of studies currently in literature does not seem commensurate to the potential of histotripsy, suggesting there may be some barrier to entry into the field. One potential barrier may be the due to the complexity of and inability to source low-cost histotripsy devices, requiring them to be fabricated in-house. It is believed that a device which can be gel-coupled to tissue and is as

simple to operate as a standard clinical ultrasound would reduce this barrier to entry in histotripsy work, allowing researchers around the world to explore histotripsy as a treatment option for numerous conditions. With the above in mind, this work presents a single-element 15 mm flat-aperture, 6.0 MHz histotripsy device designed with hand-held applications in mind.

An operating frequency of 6.0 MHz was chosen to achieve a tight focal spot, potentially allowing ablation of smaller murine organs such as the kidney, pancreas, or thyroid whose dimensions only measure on the order of millimeters [83]. To avoid the need for, but not necessarily exclude the possibility of, using a water-bath to couple devices to animals a flat-aperture design allows coupling with standard ultrasound gel. A water-bladder on the transducer face was also avoided to ensure air-bubbles and the potential for leaks was a non-issue, instead relying on an epoxy-fill of the transducer curvature which has been reduced substantially using a Fresnel-based lens design. Characterization of the device is performed using a combination of simulation, hydrophone measurements, and bubble-cloud images under microscope magnification. A version of the device with a central hole for future addition of a co-registered imaging probe was also tested for cavitation potential. The reduced curvature of a Fresnel lens may be preferred for co-axial co-registration to avoid significant attenuation of the imaging array output due to epoxy fill, while also avoiding having the endoscope protrude well into the lens curvature.

Section 6.2 of this work details the design and fabrication steps used for this lens-based device while Section 6.3 provides information on the experimental characterization setup and equipment. In Section 6.4.1 both measured and simulated data for the full-aperture device and the device with a central hole are presented and compared, and a discussion of the presented results can be found in Section 6.5. Section 6.6 concludes the work with a brief summary and some future direction for this research.

6.2 Design and Fabrication

Design of the transducer stack follows the methodology of Woodacre *et. al.* [102] with a device consisting of an 6061-T6 aluminum lens, an air-backed piezoelectric material with an acoustic impedance closely matching that of the lens, a thin epoxy bonding layer between lens and piezoelectric, a parylene-C matching layer on the lens surface, and a casing designed and printed using the Formlabs Form 2 3-D SLA printer (Formlabs, Inc., Somerville, MA, USA) housing each transducer. The key difference in this device is the use of a Fresnel lens to avoid the deep curvature of previous lens designs.

Figure 6.1 shows that the Fresnel lens is designed by combining multiple curves (black) all focused to the marked axial location at 8 mm (X) and axially offset from

each other by a distance D_f , calculated as,

$$D_f = N_f \frac{v_m v_l}{v_l - v_m} \frac{1}{f} \quad (6.1)$$

where f is the operating frequency and N_f is the number cycles delay between waves arriving to the focus at that frequency from each curve, v_l is the acoustic wave velocity in the lens, and v_m is the wave velocity in the medium of interest. Equation 6.1 is derived by assuming a plane wave impinges on the back of the lens and that the time-of-flight from each Fresnel ring arrives at the focus delayed from its neighbours by an integer number of wavelengths.

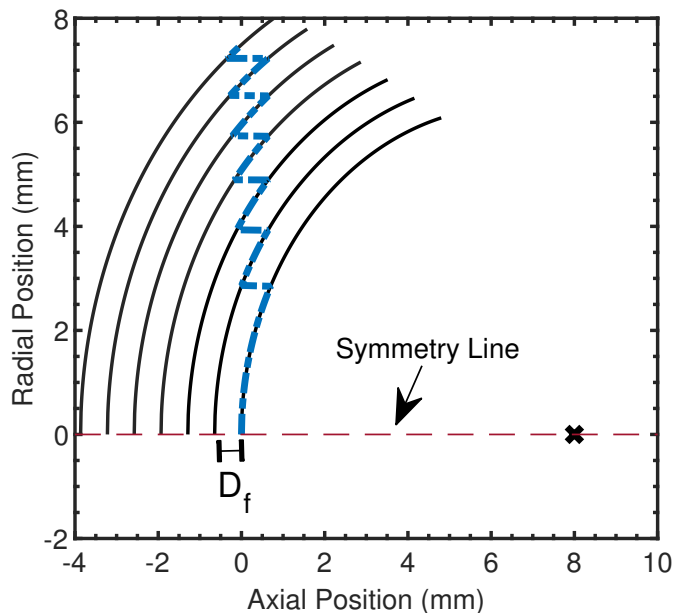


Figure 6.1: Multiple curves (black) all focused to the marked axial location at 8 mm (X) and offset from each other by a distance D_f form the basis of the Fresnel lens. For this work, moving along each curve and stepping back to the next curve once the axial position reaches 0.64 mm creates the blue dashed line which can be revolved about the symmetry axis to form the Fresnel lens surface shape.

In this specific case, $D_f = 0.644$ mm where the values used to calculate D_f are provided in Table 6.1 and the lens and medium are aluminum and water, respectively. Note, the lines stepping between curves in Figure 6.1 need not only travel axially, nor do they need to be equal length (they are not in this case). For ease of machining, N_f was chosen to be two (2) which results in seven emitting surfaces for a 15 mm diameter device. A value of one (1) for N_f would lead to 13 surfaces, the outer few of which would have dimensions difficult to achieve in CNC fabrication.

Table 6.1: Properties Used For Fresnel Lens Design

Property	N_f (unitless)	v_m (m/s)	v_l (m/s)	f (MHz)
Numerical Value	2	1480	6320	6.0

Revolving the Fresnel curve from Figure 6.1 about the symmetry line and adding 2 mm of material to the lens for additional rigidity results in the final lens design shown Figure 6.2 with CAD renderings of the front, side, and cross-section views, as well as a picture of the final machined lens itself (bottom-left) and the lens if used in a co-registered imaging device with a 5.7 mm diameter central hole (bottom-right). A cross-section view shows that the inner surface as well as five (5) rings have been machined, while the outer-most ring was not fully machined and does not contribute acoustically as it is occluded by the next innermost ring.

Two piezoelectric materials were used: a 5 MHz 1-3 PZT-5A-polymer dice-and-fill composite with an acoustic impedance calculated to be approximately 14 MRayls



Figure 6.2: Top, side, and cross-section renderings of the final lens design are shown along the top, where the cross-section shows six separate surfaces. The bottom left and right images show the final machined Fresnel lens, both without and with a hole for co-registered imaging.

(Smart Material Corp., USA), and a porous piezoelectric material, Meggitt PZ-39, with an acoustic impedance reported to be 18 MRayls (Meggitt A/S, Denmark). Both materials match closely enough to the aluminum lens that reflections at the piezo-lens boundary are minimized. The porous material was chosen for the co-registered device to provide more focal pressure at a given drive voltage, as demonstrated in Chapter 5.

On the face of the lens is a quarter wavelength matching layer of Parylene-C deposited using a Specialty Coating Systems Labcoter 2 Parylene Deposition System.

Parylene-C was chosen as its acoustic impedance of 2.75 MRayl [132] matches reasonably between aluminum lens and water and the acoustic wave propagation speed is known at 2135 m/s. For this device, given the lens is designed to operate at 6 MHz the desired quarter wavelength matching layer thickness for Parylene-C is 89 micrometers. Once Parylene coated, the lens curvature was filled with Precision Acoustics Aptflex F7 encapsulation material (Precision Acoustics Ltd., Dorchester UK) - a water-matching epoxy with an attenuation coefficient of ~ 3 dB/mm at 6.0 MHz.

Electrical connectivity was provided by two small strips of flex circuit board measuring less than 1mm by 2 mm attached to the piezo element face and lens using cyanoacrylate adhesive with wire bonds connecting the flex circuit to the acoustic element. Micro-coaxial cables are soldered to the flex strips and run to a connector, allowing the device to be driven using a pulser similar to the one described in Brown and Lockwood [147] modified to run single-ended.

6.3 Methods

6.3.1 Full-Aperture Transducer

Validation of the full-aperture transducer design was performed through hydrophone measurements compared with FEM simulations, as well as through visual cavitation confirmation. Using a Onda HGL-0085 capsule hydrophone (Onda Corp, Sunnyvale,

USA) with a known calibration, the substitution method was used to calibrate a Precision Acoustics Fibre-optic hydrophone (FOH) system which was used for all acoustic measurements due to its higher pressure rating. FOH sensitivity was found to be 0.18 V/MPa at 6.0 MHz and all measurements for pressure field and focal pressure versus drive voltage were performed at steady-state.

Prior to applying a parylene-C matching layer, the full aperture PZT5A device was pulsed to confirm the lens was machined based on design parameters. The pressure was measured at the focus for the transducer pulsed with one (1), two (2), three (3), and five (5) cycles at 6.0 MHz, the design frequency, and compared to simulated results from COMSOL Multiphysics. Also before applying parylene, the steady-state peak focal pressure versus frequency was measured. The device was pulsed with a negative uni-polar -8.0 V 25-cycle square pulse with the frequency ramped from 5.8 MHz to 6.5 MHz in 0.5 MHz increments.

The steady-state focal pressure was measured at 6.1 MHz before parylene application, after parylene application, and after filling the Fresnel lens curvature with epoxy to determine how the parylene and epoxy fill affect focal pressure. The transducer was again driven with a negative uni-polar -8.0 V 25-cycle square pulse.

Radial and axial pressure field measurements for the transducer were generated by translating it using an in-house XYZ motion stage setup with Thorlabs TDC001

motor drivers and MTS50 motion stages (Thorlabs Inc., Newton, NJ, USA) and collecting steady-state pressure measurements over a focal-centered 1 mm by 1 mm plane normal to the transmission axis . COMSOL Multiphysics was used to perform 2-D axysymmetric finite-element method FEM simulations of the pressure field generated by the lens itself.

Optical images of the bubble cloud were captured using a Zeiss Discovery.V20 Stereo Microscope with a Canon Rebel T1i EOS digital camera with the bubble cloud was illuminated perpendicular to the direction of imaging, and a camera exposure time of 1/60 s was used for a single image, with multiple images combined using a median filter to generate cloud images at a single drive level. The clouds were generated with a 17 cycle negative uni-polar pulse at 6.0 MHz drive frequency.

6.3.2 Removed Center Element Transducer

For the device with the central element machined out, a relative pressure-per-volt measurement was made with respect to the full-aperture device where each transducer was driven with a negative uni-polar 25-cycle square pulse with a drive voltage ramped from -0.5 to -7 V in 0.5 V increments. The results are compared to determine pressure reduction from removing the center element. Additionally, a COMSOL simulation of peak focal pressure was performed for this device and the full-aperture transducer to compare relative pressure change from removing the lens center. Voltage was

increased until cavitation was again confirmed visually, driving the transducer with a 17 cycle negative uni-polar pulse at 6.0 MHz drive frequency.

6.4 Results

6.4.1 Full Aperture PZT5A Device

The pre-parylene focal pressure plots for 1,2,3, 5-cycles are shown in Figure 6.3. Note, the pressure scale remains constant between each data set. Arrows in the 1-cycle plot indicate pulse arrival times from the center zone and the first three Fresnel rings. The arrival data for the fourth and fifth rings is cropped from the plots for clarity, as internal reflections cause substantial ringing prior to applying the matching layer.

The timing between the first peak and fourth peak arrivals is $0.992 \mu s$ which, given an N_f of two, corresponds to a six cycle delay and a design frequency of 6.05 MHz. The 2-cycle data shows that the second cycle fills the space between the labeled peaks in the 1-cycle data; however, the peak pressure does not increase. This is expected behavior as the Fresnel steps are delayed from each other by two cycles. When pulsed 3-cycle, constructive interference now increases the pressure at the labeled locations in the 3-cycle data (the same locations labeled in the 1-cycle data) and, finally, when pulsed with 5-cycles constructive interference once again increases pressure. The 4-cycle data is not shown, but it behaves as the 2-cycle data where the peak pressure does not improve but additional gaps are filled in. To

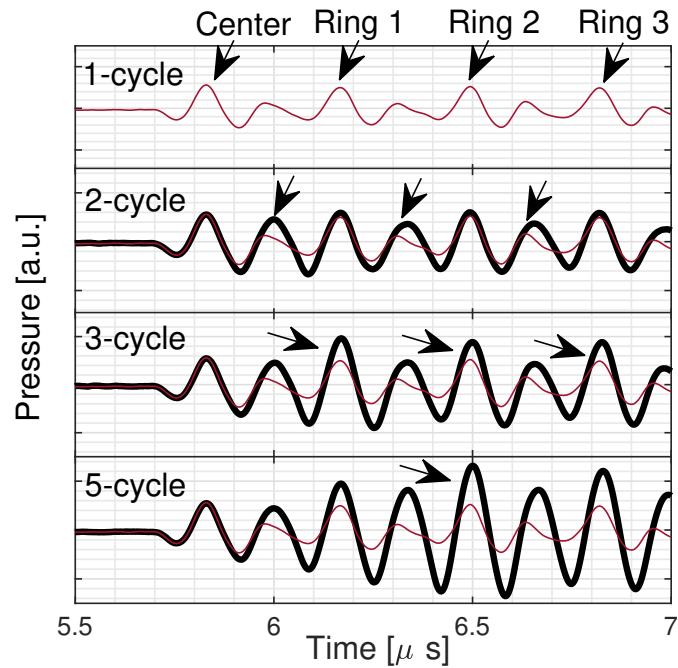


Figure 6.3: Normalized focal pressure measurements from a single, two (2), three (3) and five (5) cycle 6.0 MHz pulse are plotted with the single-cycle response additionally plotted in red for the two, three and five cycle responses. Arrows on the upper curve indicate the pulse arrival times from the center zone and the first three Fresnel rings.

confirm this behavior is expected, a comparison of the data from Figure 6.3 is made to time-domain FEM simulations from COMSOL in Figure 6.4

The simulated time-domain data shows similar behavior to the measured data where, for a single-cycle pulse, the peaks arriving from each Fresnel ring line-up well between measurement and simulations, and there is a gap between peaks due to the design choice of $N_f = 2$. In the 2-cycle plot, the space between pulses is filled while the original pulse amplitudes labeled in the 1-cycle data remain consistent. For the 3-cycle and 5-cycle plots, simulated data seems to act as expected where constructive interference leads to an increase in pressure at the labeled points. The

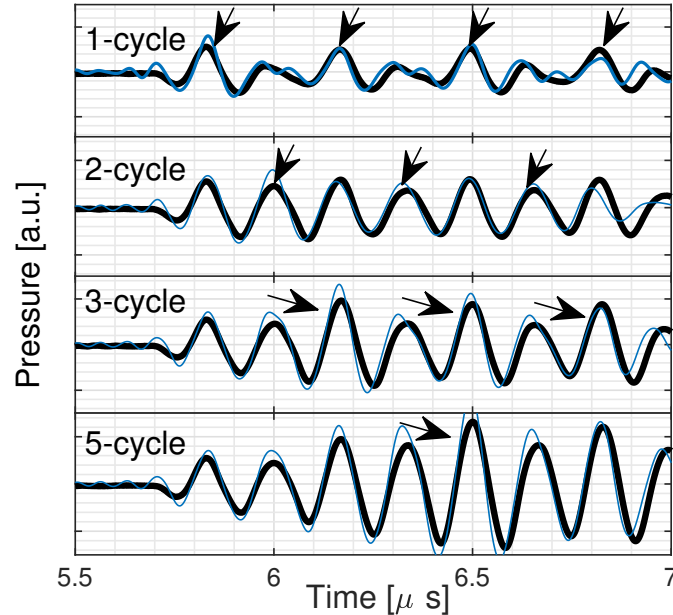


Figure 6.4: Normalized focal pressure measurements from a single, two (2), three (3) and five(3) cycle 6.0 MHz pulse are plotted along with their respective time-domain FEM simulations.

data presented in Figure 6.3 and Figure 6.4 shows that the machined lens matches the design parameters, but it is also important to confirm the maximum pressure also occurs at or near the design frequency of 6.0 MHz.

The results of measuring steady-state focal pressure as a function of drive voltage, presented in Figure 6.5 show that the peak-to-peak pressure reaches a maximum of 2.18 MPa at 6.1 MHz, with a reasonably flat pressure plateau from 6.05 MHz to 6.3 MHz. This measurement was performed also without parylene to avoid any potential frequency shifting of the result.

A measurement of the steady-state focal pressure at 6.1 MHz, the optimum determined in Figure 6.5, for the device without a parylene matching layer, with a

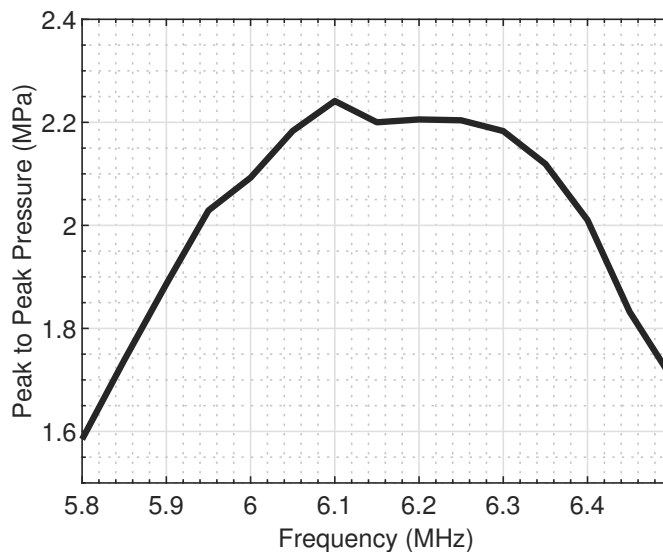


Figure 6.5: The 8.0 V drive level steady state focal pressure as a function of frequency swept from 5.8 to 6.5 MHz, showing a peak at 6.1 MHz with a pressure plateau from 6.05 MHz to 6.3 MHz.

parylene matching layer but without an epoxy fill, and after filling the lens curvature with epoxy is shown in Figure 6.6.

The peak-to-peak pressure for the uncoated lens is 2.2 MPa, for the parylene coated lens is 3.2 MPa, and for the parylene coated lens with Aptflex F7 filling the lens curvature is 3.0 MPa, meaning the addition of parylene increases output pressure by 1.0 MPa or 45%, and the Aptflex F7 reduced the pressure by 0.2 MPa, or a 6% reduction from peak pressure.

The pressure field through the focus and normal to the lens axis of symmetry was measured after parylene coating and the results are shown in Figure 6.7 as a surface plot with the X and Y direction pressure fields through the focus plotted on their respective axis along with COMSOL simulated results as dashed red lines.

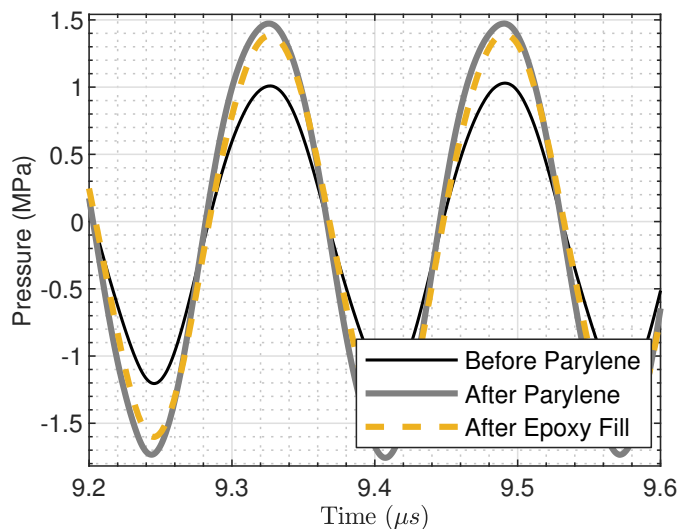


Figure 6.6: Three curves show the focal pressure at 6.1 MHz for a device without coatings (black), the same device with a quarter-wave matching layer (thick grey) and that device with a quarter-wave matching layer and the lens curve filled with epoxy. Parylene increases the peak-to-peak pressure output by 45% from 2.2 MPa to 3.2 MPa, and the epoxy reduces pressure output by 6% from 3.2 MPa to 3.0 MPa.

The measured full-width at half maximum (FWHM) in the x-axis is 0.34 mm while in the y-axis 0.29 mm, showing some asymmetry in the field while the FWHM in the COMSOL simulations is calculated to be 0.274 mm. The pressure field along the focal axis is also measured and presented in Figure 6.8.

The measured -3 dB beam lengths are 0.88 mm and 0.99 mm for the measured and simulated data, a difference of 11%, while the -6 dB beam lengths are 1.23 mm and 1.48 mm, a difference of 17%. To confirm the transducer can generate a bubble cloud, the transducer was immersed in degassed water and pulsed. The first sustained bubble cloud was found at a drive voltage of 190 V, at a 1 ms repetition rate with 17 cycles at 6.0 MHz. The voltage was increased progressively, and clouds at voltages of 190, 220, 250, 310, 340, and 370 V are shown in Figure 6.9.

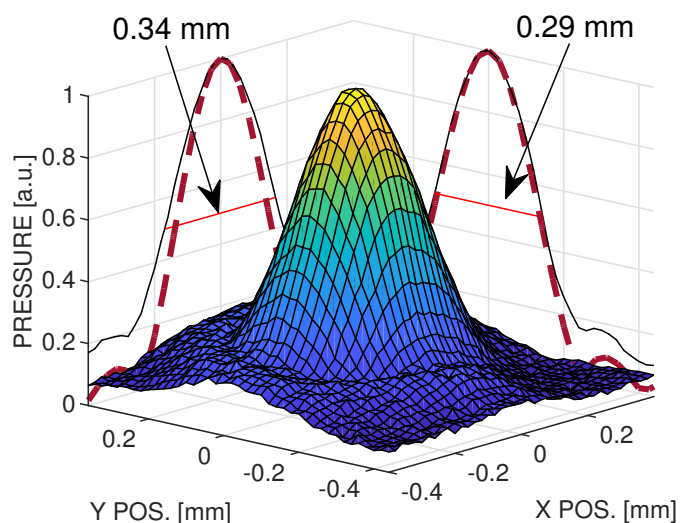


Figure 6.7: A surface plot of the measured pressure field in a focal-intersection plane normal to the direction of acoustic propagation shows a FWHM of 0.34 mm in the x-direction and 0.29 mm in the y-direction. The red dashed line shows COMSOL simulated pressure measurements, where the FWHM is calculated 0.274 mm.

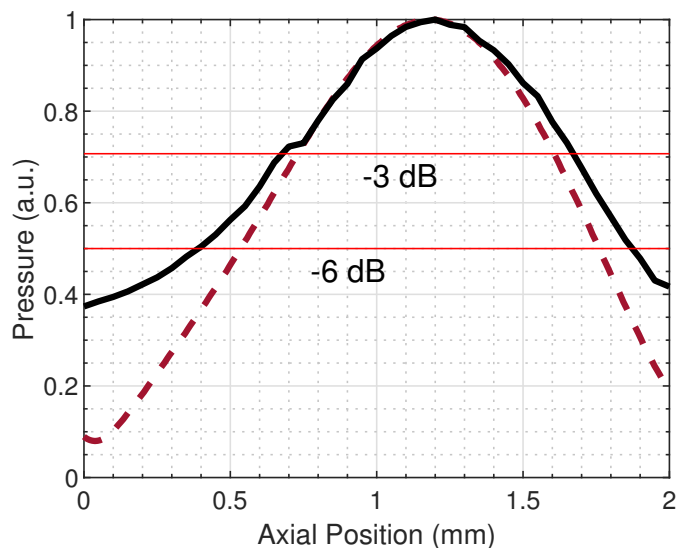


Figure 6.8: The black curve shows the measured pressure versus axial position around the focus for the PZT5A Fresnel lens, while the red dashed line provides a simulated result. The measured -3 dB beam lengths are 0.88 mm and 0.99 mm for the measured and simulated data and 1.23 mm and 1.48 mm at -6 dB.

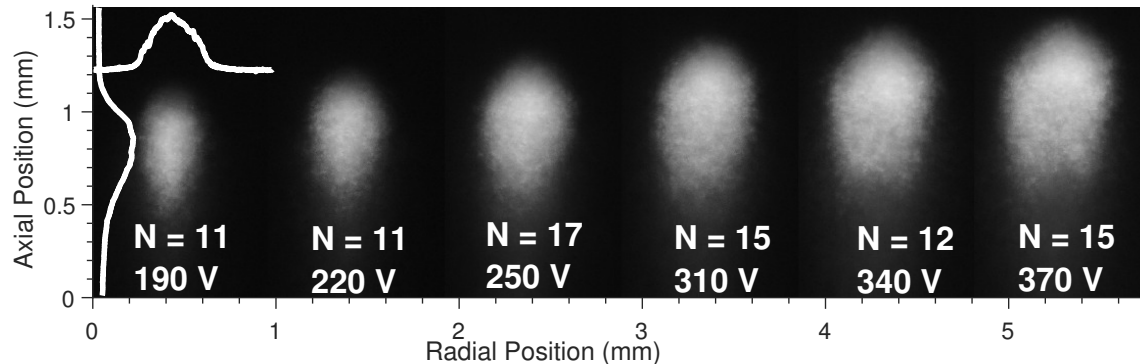


Figure 6.9: Six bubble cloud images, each composed of N median-filtered images at their respective voltages, show the cloud size increasing as drive voltage is increased from 190 V to 370 V. The 190 V cloud includes two curves - brightness versus position on the plot through the largest radial and axial portions of the cloud.

Each cloud is a composite of N images, combined using a median filter in MATLAB. The individual images making up each composite were acquired by setting the camera described in Section 6.3 to burst mode and holding down the shutter button on the camera. The variation in N is from holding the shutter button for different lengths of time, however, the variations in N do not appear to significantly change estimates of cloud size. The longest dimension of each cloud axially and radially was identified by summing lines of pixel, both radially and axially, and finding the largest sum and then the identified image line is used to determine cloud size. Example curve plotting the image brightness along the widest radial and axial dimensions of the 190 V bubble cloud are shown overlaid above and to the left of the 190 V cloud, respectively. Cloud sizes are estimated by visually determining where the transition from cloud to background image occurs, a transition estimated to occur at a brightness value of 80, where brightness could range from 0-255. The results and number

of compounds per image are summarized in Table 6.2.

Table 6.2: Estimated Bubble Cloud Sizes for Fresnel Lens

Voltage (V)	190	220	250	310	340	370
N Compounded Images	11	11	17	15	12	15
Radial Width (mm)	0.31	0.35	0.43	0.46	0.49	0.51
Axial Length (mm)	0.53	0.57	0.71	0.77	0.78	0.81

The radial cloud width monotonically increases with size ranging from 0.31 mm at 190 V to 0.51 mm at 370V, while the axial cloud length increases by 0.28 mm from 0.53 mm at 190 V to 0.81 mm at 370 V. It should be noted the transition choice of 80 was based on visual examination of individual cloud images as well as the composite frames in Figure 6.9.

6.4.2 Removed Center Element Transducer

Normalized pressure per volt measurements between the full-aperture and removed center element transducers are shown in Figure 6.10. Note, these measurements were normalized as they were taken with an un-calibrated hydrophone. Measurement of absolute pressures is ongoing. That said, both devices were measured within minutes of each other at the same drive frequency so relative comparisons are valid. Removing the center element reduced the focal pressure by 38%, suggesting a significant amount of pressure comes from the central element despite it only accounting for 14.4% of the total transducer area. A frequency-domain COMSOL simulation, modified from

that used for pressure field data in Section 6.4.1 to include a central hole, showed a 33% reduction in focal pressure after removing the transducer center element.

Voltage was increased and cavitation was observed to occur intermittently at 370 V drive levels, with cavitation maintaining a consistent observable bubble cloud at a 400 V drive level.

6.5 Discussion

The results from Figures 6.3 and 6.4 showing pulses arriving from each individual Fresnel ring at a delay of two-lambda validate the lens curvature and the use of Equation 6.1 for the Fresnel step distance. This is corroborated by the COMSOL time-domain simulations of focal pressure lining up with the measured one-way pulse measurement, although slight inconsistencies in relative pressure amplitudes between model and measurement can be attributed to the signal in the simulation being a pressure source and not accurately capturing the impulse response function of the transducer. It can also be reasonably concluded that the lens was machined to an acceptable tolerance, since cavitation generation occurred. In Figure 6.3 the delay between the first and fourth peaks should be $1.0 \mu\text{s}$ for a 6.0 MHz pulse delayed by six cycles but was measured to be $0.992 \mu\text{s}$ - a deviation which could be explained by slight machining variation or error in the speed of sound used to calculate D_f . That said, Figures 6.7 and 6.8 show there may be room for improvement in the lens

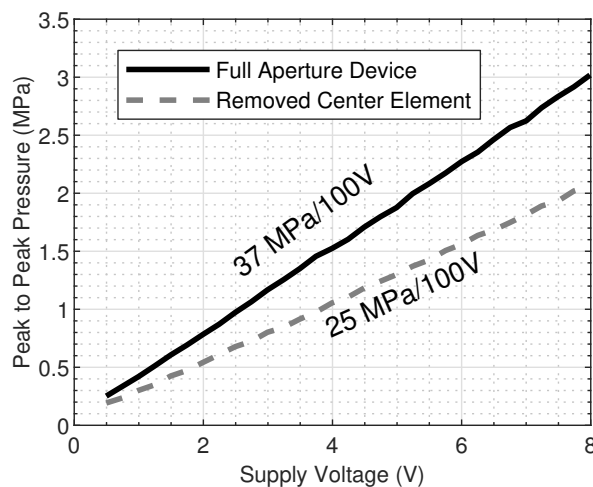


Figure 6.10: The pressure per voltage in units normalized to the peak full-aperture device pressure, where the device with a missing center element shows a slope of 8.68 arbitrary pressure units per 100 V, compared to the 14.00 a.u. per 100 V. This is a 38% reduction in pressure.

curvature. It has been shown in previous work that there can be a good match between our COMSOL simulations and measured pressure fields for a given lens model [141], suggesting the deviation of the FWHM and -3 dB beam dimensions could be due to things such as flatness of the composite-attached lens face, or difficulty in maintaining dimensional tolerances over the full lens shape.

We know from previous work that attaching an impedance matched piezo to lens leads to a maximum power output at frequencies significantly higher than the piezo design frequency[102]. Figure 6.5 showing a broad frequency range of maximum pressure output is likely a consequence of this, where the lens has a peak output at between 6.0 and 6.1 MHz, however, the piezo-on-aluminum frequency shift effect may provide a maximum pressure closer to 6.2 or 6.3 MHz, broadening the range over

which the device can be driven at the cost of maximum output. It could be possible to improve overall pressure output by making the piezo elements thicker, matching the maximum stack output to the Fresnel design frequency.

The focal pressure increase by a matching layer, in this case by 45%, as shown by the data in Figure 6.6 has been simulated in KLM [102] and the behavior has been consistently observed when fabricating aluminum-lens based devices where cavitation drive levels were lower with a parylene layer, but this measurement confirms the behavior experimentally. To understand the behavior, consider that an aluminum lens without a matching layer would have a power reflection coefficient from aluminum to water of 70%, assuming normal incidence for simplicity; however, and all of that energy would be back-scattered at a range of angles based on the lens curvature. This back-scattered energy would reflect internally in the lens, but would likely not contribute to the output pressure. Consider the alternative where a quarter-wave matching layer of parylene is placed on the lens face. With the matching layer, the power reflection coefficient should be zero, ideally, ensuring maximum power transfer to the medium. In reality, something in-between exists as parylene is not a perfect match between aluminum and water.

The drop in pressure from 3.2 MPa to 3.0 MPa with the addition of Aptflex F7 is equivalent to a -0.56 dB change in pressure. Given the attenuation coefficient of ~ 3 dB/mm at 6.0 MHz, the average path length spent within the epoxy is 0.186 mm.

This relatively small loss in pressure suggests a thicker epoxy layer could be applied for additional robustness of the device if needed. For perspective, the average path length spent in epoxy for a 15 mm diameter non-Fresnel lens with a focus 8 mm from the aperture can be estimated by taking the volume inside the lens curvature and dividing by the aperture area. For a lens of this design, the volume was measured in CAD software to be 369.65 mm^3 , and the aperture area 176.78 mm^2 , giving an average path length of 2.09 mm - corresponding to -6.27 dB of loss, or a pressure loss of 48.5% compared to no epoxy fill. Note, this is an underestimate of the actual loss, but still illustrates the benefit in reducing the lens curvature.

The measured pressure fields shown in Figures 6.7 and 6.8 show the focus to be larger in the radial and axial directions than simulations predict. Given previous, similar models show a good agreement between COMSOL model and measured pressure fields [141], it is believed that machining limitations may be the cause of this discrepancy. The lens face that the piezo is attached to may not be normal to the acoustic axis, explaining the slightly uneven beam widths shown in Figure 6.7. Additionally, the aluminum lens becomes thin near the peak of each Fresnel ring, meaning the aluminum could become misshapen during the machining process, reducing how well the actual piece matches the CAD design. Nonetheless, the focus does allow cavitation to occur, and improvements to the machining process can only reduce the voltage level needed for cavitation, allowing reduction in lens size or increased ablation rates.

The cloud sizes presented in Table 6.2 are based on a subjective brightness threshold of 80 out of 255 to delineate between cloud and background. The justification for this choice comes from visual examination of a set of clouds, where the edge was chosen and labeled, and it was found that each point had a brightness of somewhere between 70 and 90. The average, 80 was used, however, using any value between 70 and 90 had minimal effect on the estimated cloud size. This brightness threshold will depend on a number of factors such as cloud illumination, camera ISO and aperture settings, and exposure time, therefore the threshold must be identified on an experiment by experiment basis. Nevertheless, these estimated cloud sizes in water provide a point of reference for potential ablation sizes at these drive levels in tissue and show that ablation size should grow with increasing drive level.

Removing the center transducer element lead to more than doubling drive levels to reach free-field cavitation. Given the center element only contributes 14.4% of the total piezo area and should contribute the same amount to the acoustic power emitted, additional factors must contribute to this drive level requirement. First, the COMSOL simulation does suggest removal of the center element reduced focal pressure by 33%. We suspect this significant contribution to the pressure by the center element is due to the outer elements self-occluding each other. Examining Figure 6.1 we see line-of-sight to the focus from the bottom of each subsequent ring is blocked by the neighboring ring. By drawing lines from the focus at 8 mm, and having

these lines intersect each Fresnel ring and the peak of the next inner ring, it can be shown that 68.13 mm^2 of the total 176.7 mm^2 piezo element area may be occluded from contributing to the focal pressure, although this assumes no diffraction which is a useful but likely not fully accurate assumption. Nevertheless, this means that total effective area of piezo is only 108.5 mm^2 , meaning the center element contributes 23.5% to the active piezo area. Removal of the center element will also change the depth of field and beam widths, potentially spreading acoustic energy over a broader area and reducing peak pressure. Additionally, outside of the linear acoustics regime, this device likely operates through shock-scatter histotripsy with such a large number of cycles, and given the outer rings are further from the focus they may be more susceptible to the compounding non-linear effects and therefore frequency dependent attenuation. It would be difficult to quantify such an effect through simulation due to the complex lens shape as typically only simple lens shapes are used in KZK modeling - a common method to simulate non-linear acoustics. The self-occlusion of elements would become less of a problem if the focus were pushed out further, although this then opens the device up to additional non-linear effects and an overall reduction in focal gain.

One downside of the Fresnel design is the number of cycles needed to reach steady pressure - at least two per Fresnel zone. This requires more power, and precludes the possibility of achieving intrinsic threshold histotripsy. That being said, because

of the high frequency shock-scatter ablation still maintains a tight ablation zone that may be acceptable in most applications. If intrinsic threshold cavitation is necessary, one may be able to etch a pattern in the electrode on the device and create a phased array, delaying the pulse from each Fresnel zone to allow focusing with one or two cycles.

6.6 Conclusion

A single-element flat-aperture 6.0 MHz histotripsy transducer capable of gel-coupling to tissue was successfully fabricated and was presented along with measurements and simulations to validate the design. The measured pressure fields matched reasonably well with simulation, but improvements in the lens fabrication process may improve this. Cavitation occurred free-field in water and images captured of the cloud show that small volumes could be ablated. With imaging co-registration, it is believed that this device will allow researchers to apply histotripsy to new, and as-of-yet unexplored areas of research and medical treatments without the complication of needing to cover the transducer with a water sac or fill a large lens curvature with epoxy or gel.

Chapter 7

Conclusion and Future Work

The individual conclusions of each chapter stand on their own as a summary of the works. From a holistic view, this thesis presents a collection of devices that push transducer fabrication in a direction previously unseen for histotripsy. The use of high-frequency (6 MHz range) and single-element aluminum lens designs matched to the piezo element should allow researchers to build devices directly from this work with an ablation spot size smaller than previously reported. The composites from Smart Materials Inc., and solid piezo material from Meggitt are both low cost and easy to order in custom shapes and thicknesses. The one barrier to fabrication may be parylene coating for matching layers, but even these can be contracted out to a number of companies whose regular business is custom parylene layer deposition. The simple pulser design from Brown *et. al.* [147] should also be easy to replicate for driving these devices.

The small form-factor for devices presented in Chapters 5 and 6 could lead to surgical options not previously explored, although the path through pre-clinical and

clinical trials as well as regulatory approvals and meeting of the IEC 60601 standard required for all medical devices are still a significant barrier. It was mentioned that the target is neural ablations, but any difficult to reach tumors outside of the brain are also well within the capability of these devices. Obese patients, on whom the current generation of histotripsy may have difficulty with due to the high attenuation factor and thickness of adipose tissue, could have liver tumors ablated through a laparoscopic device which bypasses these layers. Pancreatic tumor treatment, which may be difficult for previous generation devices due to their relatively large focal spot sizes and the size of the pancreas itself, may be possible with the smaller spot size and precise positioning these small form-factor devices allow. And, all of this combined with the recent discovery of histotripsy 'tumor inoculation' effect mean devices such as these may be in demand within the near future.

7.1 Future Work

The focus of this work was on transducer design, fabrication, and validation, so in this thesis there are few applications tested with a clear lack of small-animal work past the proof-of-concept ablations in Chapter 4 and 5. One of the obvious future directions will be showing that these devices can ablate with high precision and accuracy on mouse models, with spot sizes small enough to target not just the larger organs such as the brain or liver. Survival studies on brain ablations, followed by tumor implantation

and ablation while monitoring immune response will be key in moving forward.

From an academic perspective, devices of even higher frequency should be made, pushing the envelope on how small of a spot size can be achieved. Devices with a tighter focus, and higher frequency could be used on tissue samples, potentially competing with LGFU in the ablation of individual cells but, without the need for a laser, or integrated into lab equipment as a compact way to blend or lyse cells. A more in-depth exploration of the non-linear fields generated by these devices should also be performed, although this would require a special fiber hydrophone or membrane hydrophone. The ability to build and validate a model of the non-linear fields could lead to improvements on future devices or a way to predict if a device will work prior to fabrication.

Bibliography

- [1] J. Scalici, B. B. Laughlin, M. A. Finan, W. Bin, and R. P. Rocconi, “The trend towards minimally invasive surgery (mis) for endometrial cancer: An acs-nsqip evaluation of surgical outcomes,” *Gynecologic Oncology*, vol. 136, pp. 512–515, 2015.
- [2] V. Velanovich, “Laparoscopic vs open surgery,” *Surgical Endoscopy*, vol. 14, pp. 16–21, 2000.
- [3] J. M. Regan, E. Worley, C. Shelburne, R. Pullarkat, and J. C. Watson, “Burr hole washout versus craniotomy for chronic subdural hematoma: Patient outcome and cost analysis,” *PLoS One*, vol. 10, no. 1, p. e0115085, 2015.
- [4] Y. Mondorf, M. Abu-Owaimer, M. R. Gaab, and J. M. K. Oertel, “Chronic subdural hematoma–craniotomy versus burr hole trepanation.,” *British journal of neurosurgery*, vol. 23, pp. 612–6, Dec 2009.
- [5] C. Y. Peterson, K. Palazzi, J. K. Parsons, D. C. Chang, and S. L. Ramamoorthy, “The prevalence of laparoscopy and patient safety outcomes: an analysis of colorectal resections,” *Surgical Endoscopy*, vol. 28, pp. 608–616, Feb 2014.
- [6] H. Ueno, H. Kobayashi, T. Konishi, F. Ishida, T. Yamaguchi, T. Hinoi, Y. Kanemitsu, Y. Inoue, N. Tomita, N. Matsubara, K. Komori, H. Ozawa, T. Nagasaka, H. Hasegawa, M. Koyama, Y. Akagi, T. Yatsuoka, K. Kumamoto, K. Kurachi, K. Tanakaya, K. Yoshimatsu, T. Watanabe, K. Sugihara, and H. Ishida, “Prevalence of laparoscopic surgical treatment and its clinical outcomes in patients with familial adenomatous polyposis in japan,” *International Journal of Clinical Oncology*, vol. 21, pp. 713–722, Aug 2016.
- [7] G. V. R. Inc., “Surgical equipment/instruments market analysis by product (sutures & staplers, handheld & electrosurgical devices), by application (neurosurgery, plastic & reconstructive surgery, obstetrics & gynecology, cardiovascular, orthopedic), and segment forecasts, 2014 - 2025,” Market Research Report GVR-1-68038-240-2, Grand View Research Inc., July 2017.
- [8] Z. Xu, A. Ludomirsky, L. Y. Eun, T. L. Hall, B. C. Tran, J. B. Fowlkes, and C. A. Cain, “Controlled ultrasound tissue erosion.,” *IEEE transactions on ultrasonics, ferroelectrics, and frequency control*, vol. 51, pp. 726–36, Jun 2004.
- [9] W. W. Roberts, T. L. Hall, K. Ives, J. S. Wolf, J. B. Fowlkes, and C. A. Cain, “Pulsed cavitation ultrasound: a noninvasive technology for controlled tissue

- ablation (histotripsy) in the rabbit kidney.," *The Journal of urology*, vol. 175, pp. 734–8, Feb 2006.
- [10] N. Lu, D. Gupta, B. J. Daou, A. Fox, D. Choi, J. R. Sukovich, T. L. Hall, S. Camelo-Piragua, N. Chaudhary, J. Snell, *et al.*, "Transcranial magnetic resonance-guided histotripsy for brain surgery: Pre-clinical investigation," *Ultrasound in Medicine & Biology*, 2021.
- [11] Y.-F. Zhou, "High intensity focused ultrasound in clinical tumor ablation.," *World journal of clinical oncology*, vol. 2, pp. 8–27, Jan 2011.
- [12] A. Bezanson, R. Adamson, and J. Brown, "Fabrication and performance of a miniaturized 64-element high-frequency endoscopic phased array.," *IEEE transactions on ultrasonics, ferroelectrics, and frequency control*, vol. 61, pp. 33–43, Jan 2014.
- [13] C. A. Samson, A. Bezanson, and J. A. Brown, "A sub-nyquist variable sampling, high-frequency phased array beamformer," *IEEE Transactions on Ultrasonics, Ferroelectrics, and Frequency Control*, vol. 64, pp. 568–576, March 2017.
- [14] M. P. Heron, "Deaths: leading causes for 2017," *National Vital Statistics Reports*, vol. 68, no. 6, 2019.
- [15] K. D. Miller, L. Nogueira, A. B. Mariotto, J. H. Rowland, K. R. Yabroff, C. M. Alfano, A. Jemal, J. L. Kramer, and R. L. Siegel, "Cancer treatment and survivorship statistics, 2019," *CA: a cancer journal for clinicians*, vol. 69, no. 5, pp. 363–385, 2019.
- [16] E. van Sonnenberg, W. McMullen, and L. Solbiati, *Tumor ablation: principles and practice*. Springer Science & Business Media, 2005.
- [17] T. W. Kang and H. Rhim, "Recent advances in tumor ablation for hepatocellular carcinoma," *Liver Cancer*, vol. 4, no. 3, pp. 176–187, 2015.
- [18] S. Wang, N. Shi, L. You, M. Dai, and Y. Zhao, "Minimally invasive surgical approach versus open procedure for pancreaticoduodenectomy: A systematic review and meta-analysis," *Medicine*, vol. 96, no. 50, 2017.
- [19] F. Liu, Q. Li, Y. Wei, and B. Li, "Laparoscopic versus open liver resection for difficult lesions: a meta-analysis," *Journal of Laparoendoscopic & Advanced Surgical Techniques*, vol. 28, no. 12, pp. 1428–1436, 2018.
- [20] K. T. Nguyen, J. W. Marsh, A. Tsung, J. J. L. Steel, T. C. Gamblin, and D. A. Geller, "Comparative benefits of laparoscopic vs open hepatic resection: a critical appraisal," *Archives of surgery*, vol. 146, no. 3, pp. 348–356, 2011.
- [21] E. S. Flamm, J. Ransohoff, D. Wuchinich, and A. Broadwin, "Preliminary experience with ultrasonic aspiration in neurosurgery," *Neurosurgery*, vol. 2, no. 3, pp. 240–245, 1978.

- [22] W. Hodgson, "Ultrasonic surgery," *Annals of the Royal College of Surgeons of England*, vol. 62, no. 6, p. 459, 1980.
- [23] F. Fasulo, A. Giori, S. Fissi, F. Bozzetti, R. Doci, and L. Gennari, "Cavitron ultrasonic surgical aspirator (cusa) in liver resection," *International surgery*, vol. 77, no. 1, pp. 64–66, 1992.
- [24] J. Little and M. Hollands, "Impact of the cusa and operative ultrasound on hepatic resection," *HPB Surgery*, vol. 3, no. 4, pp. 271–278, 1991.
- [25] R. T. Chopp, B. B. Shah, and J. C. Addonizio, "Use of ultrasonic surgical aspirator in renal surgery," *Urology*, vol. 22, no. 2, pp. 157–159, 1983.
- [26] "Cusa nxt ultrasonic tissue ablation system," tech. rep., Integra LifeSciences Corporation, 2013.
- [27] N. Sanghvi, F. J. Fry, R. Bihrl, R. Foster, M. Phillips, J. Syrus, A. Zaitsev, and C. Hennige, "Noninvasive surgery of prostate tissue by high-intensity focused ultrasound," *IEEE Transactions on Ultrasonics, Ferroelectrics, and Frequency Control*, vol. 43, no. 6, pp. 1099–1110, 1996.
- [28] N. T. Sanghvi, W.-H. Chen, R. Carlson, C. Weis, R. Seip, T. Uchida, and M. Marberger, "Clinical validation of real-time tissue change monitoring during prostate tissue ablation with high intensity focused ultrasound," *Journal of Therapeutic Ultrasound*, vol. 5, no. 1, p. 24, 2017.
- [29] O. Al-Bataineh, J. Jenne, and P. Huber, "Clinical and future applications of high intensity focused ultrasound in cancer.," *Cancer treatment reviews*, vol. 38, pp. 346–53, Aug 2012.
- [30] S. A. Quadri, M. Waqas, I. Khan, M. A. Khan, S. S. Suriya, M. Farooqui, and B. Fiani, "High-intensity focused ultrasound: past, present, and future in neurosurgery," *Neurosurgical focus*, vol. 44, no. 2, p. E16, 2018.
- [31] T. Hall, J. Fowlkes, and C. Cain, "Imaging feedback of tissue liquefaction (histotripsy) in ultrasound surgery," in *Ultrasonics Symposium, 2005 IEEE*, vol. 3, pp. 1732–1734, IEEE, 2005.
- [32] A. M. Lake, Z. Xu, J. E. Wilkinson, C. A. Cain, and W. W. Roberts, "Renal ablation by histotripsy—does it spare the collecting system?," *The Journal of urology*, vol. 179, pp. 1150–4, Mar 2008.
- [33] G. R. Schade, T. L. Hall, and W. W. Robers, "Urethral-sparing histotripsy of the prostate in a canine model," *Urology*, vol. 80, no. 3, pp. 730–735, 2012.
- [34] E. Vlasisavljevich, Y. Kim, S. Allen, G. Owens, S. Pelletier, C. Cain, K. Ives, and Z. Xu, "Image-guided non-invasive ultrasound liver ablation using histotripsy: feasibility study in an in vivo porcine model.," *Ultrasound in medicine & biology*, vol. 39, pp. 1398–409, Aug 2013.

- [35] A. D. Maxwell, G. Owens, H. S. Gurm, K. Ives, D. D. Myers Jr, and Z. Xu, “Noninvasive treatment of deep venous thrombosis using pulsed ultrasound cavitation therapy (histotripsy) in a porcine model,” *Journal of vascular and interventional radiology*, vol. 22, no. 3, pp. 369–377, 2011.
- [36] J. R. Sukovich, C. A. Cain, A. S. Pandey, N. Chaudhary, S. Camelo-Piragua, S. P. Allen, T. L. Hall, J. Snell, Z. Xu, J. M. Cannata, *et al.*, “In vivo histotripsy brain treatment,” *Journal of Neurosurgery*, vol. 1, no. aop, pp. 1–8, 2018.
- [37] V. A. Khokhlova, J. B. Fowlkes, W. W. Roberts, G. R. Schade, Z. Xu, T. D. Khokhlova, T. L. Hall, A. D. Maxwell, Y.-N. Wang, and C. A. Cain, “Histotripsy methods in mechanical disintegration of tissue: towards clinical applications.,” *International journal of hyperthermia : the official journal of European Society for Hyperthermic Oncology, North American Hyperthermia Group*, vol. 31, pp. 145–62, Mar 2015.
- [38] A. Maxwell, O. Sapozhnikov, M. Bailey, L. Crum, Z. Xu, B. Fowlkes, C. Cain, and V. Khokhlova, “Disintegration of tissue using high intensity focused ultrasound: Two approaches that utilize shock waves,” *Acoustics Today*, vol. 8, no. 4, pp. 24–36, 2012.
- [39] Y.-N. Wang, T. Khokhlova, M. Bailey, J. H. Hwang, and V. Khokhlova, “Histological and biochemical analysis of mechanical and thermal bioeffects in boiling histotripsy lesions induced by high intensity focused ultrasound,” *Ultrasound in medicine & biology*, vol. 39, no. 3, pp. 424–438, 2013.
- [40] M. Hoogenboom, D. C. Eikelenboom, R. J. van den Bijgaart, A. Heerschap, P. Wesseling, M. H. den Brok, J. J. Fütterer, and G. J. Adema, “Impact of mr-guided boiling histotripsy in distinct murine tumor models,” *Ultrasonics sonochemistry*, vol. 38, pp. 1–8, 2017.
- [41] G. R. Schade, Y.-N. Wang, S. D’Andrea, J. H. Hwang, W. C. Liles, and T. D. Khokhlova, “Boiling histotripsy ablation of renal cell carcinoma in the eker rat promotes a systemic inflammatory response,” *Ultrasound in medicine & biology*, vol. 45, no. 1, pp. 137–147, 2019.
- [42] T. D. Khokhlova, G. R. Schade, Y.-N. Wang, S. V. Buravkov, V. P. Chernikov, J. C. Simon, F. Starr, A. D. Maxwell, M. R. Bailey, W. Kreider, *et al.*, “Pilot in vivo studies on transcutaneous boiling histotripsy in porcine liver and kidney,” *Scientific reports*, vol. 9, no. 1, pp. 1–12, 2019.
- [43] V. A. Khokhlova, P. V. Yuldashev, P. B. Rosnitskiy, A. D. Maxwell, W. Kreider, M. R. Bailey, and O. A. Sapozhnikov, “Design of hifu transducers to generate specific nonlinear ultrasound fields,” *Physics procedia*, vol. 87, pp. 132–138, 2016.

- [44] A. L. Klibanov, “Microbubble contrast agents: targeted ultrasound imaging and ultrasound-assisted drug-delivery applications,” *Investigative radiology*, vol. 41, no. 3, pp. 354–362, 2006.
- [45] K. Kooiman, H. J. Vos, M. Versluis, and N. de Jong, “Acoustic behavior of microbubbles and implications for drug delivery,” *Advanced drug delivery reviews*, vol. 72, pp. 28–48, 2014.
- [46] N. Sheikov, N. McDannold, N. Vykhodtseva, F. Jolesz, and K. Hynynen, “Cellular mechanisms of the blood-brain barrier opening induced by ultrasound in presence of microbubbles,” *Ultrasound in medicine & biology*, vol. 30, no. 7, pp. 979–989, 2004.
- [47] H.-L. Liu, C.-H. Fan, C.-Y. Ting, and C.-K. Yeh, “Combining microbubbles and ultrasound for drug delivery to brain tumors: current progress and overview,” *Theranostics*, vol. 4, no. 4, p. 432, 2014.
- [48] Y. Wu, T. Sun, J. Tang, Y. Liu, and F. Li, “Ultrasound-targeted microbubble destruction enhances the antitumor efficacy of doxorubicin in a mouse hepatocellular carcinoma model,” *Ultrasound in Medicine & Biology*, vol. 46, no. 3, pp. 679–689, 2020.
- [49] Y. Kaneko, T. Maruyama, K. Takegami, T. Watanabe, H. Mitsui, K. Hanajiri, H. Nagawa, and Y. Matsumoto, “Use of a microbubble agent to increase the effects of high intensity focused ultrasound on liver tissue,” *European radiology*, vol. 15, no. 7, pp. 1415–1420, 2005.
- [50] G. Dimcevski, S. Kotopoulis, T. Bjånes, D. Hoem, J. Schjøtt, B. T. Gjertsen, M. Biermann, A. Molven, H. Sorbye, E. McCormack, *et al.*, “A human clinical trial using ultrasound and microbubbles to enhance gemcitabine treatment of inoperable pancreatic cancer,” *Journal of Controlled Release*, vol. 243, pp. 172–181, 2016.
- [51] L. Feldman, P. Fuchshuber, and D. B. Jones, *The SAGES manual on the fundamental use of surgical energy (FUSE)*. Springer, 2012.
- [52] R. J. Aragon and N. L. Solomon, “Techniques of hepatic resection,” *Journal of gastrointestinal oncology*, vol. 3, pp. 28–40, Mar 2012.
- [53] “Treatment of liver cancer, by stage.”
- [54] J. Brotchi, “Intrinsic spinal cord tumor resection,” *Neurosurgery*, vol. 50, no. 5, pp. 1059–1063, 2002.
- [55] J.-M. Escoffre and A. Bouakaz, *Therapeutic ultrasound*, vol. 880. Springer, 2015.
- [56] W. C. Dewey, “Arrhenius relationships from the molecule and cell to the clinic,” *International journal of hyperthermia*, vol. 10, no. 4, pp. 457–483, 1994.

- [57] S. Dasgupta, R. K. Banerjee, P. Hariharan, and M. R. Myers, "Beam localization in hifu temperature measurements using thermocouples, with application to cooling by large blood vessels," *Ultrasonics*, vol. 51, pp. 171–80, Feb 2011.
- [58] J. Huang, R. G. Holt, R. O. Cleveland, and R. A. Roy, "Experimental validation of a tractable numerical model for focused ultrasound heating in flow-through tissue phantoms.," *The Journal of the Acoustical Society of America*, vol. 116, pp. 2451–8, Oct 2004.
- [59] L. Dorr and K. Hynynen, "The effects of tissue heterogeneities and large blood vessels on the thermal exposure induced by short high-power ultrasound pulses," *International journal of hyperthermia*, vol. 8, no. 1, pp. 45–59, 1992.
- [60] P. R. Mueller and A. Adam, "Interventional oncology,"
- [61] M. Ichihara, K. Sasaki, S.-I. Umemura, M. Kushima, and T. Okai, "Blood flow occlusion via ultrasound image-guided high-intensity focused ultrasound and its effect on tissue perfusion," *Ultrasound in medicine & biology*, vol. 33, no. 3, pp. 452–459, 2007.
- [62] J. E. Kennedy, "High-intensity focused ultrasound in the treatment of solid tumours," *Nature reviews cancer*, vol. 5, no. 4, pp. 321–327, 2005.
- [63] Z. Ram, Z. R. Cohen, S. Harnof, S. Tal, M. Faibel, D. Nass, S. E. Maier, M. Hadani, and Y. Mardor, "Magnetic resonance imaging-guided, high-intensity focused ultrasound for brain tumor therapy.," *Neurosurgery*, vol. 59, pp. 949–55; discussion 955–6, Nov 2006.
- [64] D. Coluccia, J. Fandino, L. Schwyzer, R. O’Gorman, L. Remonda, J. Anon, E. Martin, and B. Werner, "First noninvasive thermal ablation of a brain tumor with mr-guided focusedultrasound," *Journal of therapeutic ultrasound*, vol. 2, no. 1, pp. 1–7, 2014.
- [65] N. McDannold, G. T. Clement, P. Black, F. Jolesz, and K. Hynynen, "Tran-scranial magnetic resonance imaging-guided focused ultrasound surgery of brain tumors: initial findings in 3 patients," *Neurosurgery*, vol. 66, no. 2, pp. 323–332, 2010.
- [66] N. Vykhodtseva, V. Sorrentino, F. A. Jolesz, R. T. Bronson, and K. Hynynen, "Mri detection of the thermal effects of focused ultrasound on the brain," *Ultrasound in medicine & biology*, vol. 26, no. 5, pp. 871–880, 2000.
- [67] Y. Zhou, "High-intensity focused ultrasound treatment for advanced pancreatic cancer," *Gastroenterology research and practice*, vol. 2014, 2014.
- [68] T. J. Dubinsky, C. Cuevas, M. K. Dighe, O. Kolokythas, and J. H. Hwang, "High-intensity focused ultrasound: current potential and oncologic applications," *American journal of roentgenology*, vol. 190, no. 1, pp. 191–199, 2008.

- [69] E. Vlaisavljevich, A. Maxwell, M. Warnez, E. Johnsen, C. A. Cain, and Z. Xu, "Histotripsy-induced cavitation cloud initiation thresholds in tissues of different mechanical properties," *IEEE transactions on ultrasonics, ferroelectrics, and frequency control*, vol. 61, pp. 341–52, Feb 2014.
- [70] K.-W. Lin, Y. Kim, A. D. Maxwell, T.-Y. Wang, T. L. Hall, Z. Xu, J. B. Fowlkes, and C. A. Cain, "Histotripsy beyond the intrinsic cavitation threshold using very short ultrasound pulses: microtripsy," *IEEE transactions on ultrasonics, ferroelectrics, and frequency control*, vol. 61, pp. 251–65, Feb 2014.
- [71] A. D. Maxwell, T.-Y. Wang, C. A. Cain, J. B. Fowlkes, O. A. Sapozhnikov, M. R. Bailey, and Z. Xu, "Cavitation clouds created by shock scattering from bubbles during histotripsy," *The Journal of the Acoustical Society of America*, vol. 130, pp. 1888–98, Oct 2011.
- [72] M. P. Krafft, "Fluorine in medical microbubbles—methodologies implemented for engineering and investigating fluorocarbon-based microbubbles," *Journal of Fluorine Chemistry*, vol. 177, pp. 19–28, 2015.
- [73] N. Sheikov, N. McDannold, S. Sharma, and K. Hynynen, "Effect of focused ultrasound applied with an ultrasound contrast agent on the tight junctional integrity of the brain microvascular endothelium," *Ultrasound in medicine & biology*, vol. 34, no. 7, pp. 1093–1104, 2008.
- [74] J. Deng, Q. Huang, F. Wang, Y. Liu, Z. Wang, Z. Wang, Q. Zhang, B. Lei, and Y. Cheng, "The role of caveolin-1 in blood–brain barrier disruption induced by focused ultrasound combined with microbubbles," *Journal of molecular neuroscience*, vol. 46, no. 3, pp. 677–687, 2012.
- [75] J. J. Choi, J. A. Feshitan, B. Baseri, S. Wang, Y.-S. Tung, M. A. Borden, and E. E. Konofagou, "Microbubble-size dependence of focused ultrasound-induced blood–brain barrier opening in mice in vivo," *IEEE Transactions on Biomedical Engineering*, vol. 57, no. 1, pp. 145–154, 2009.
- [76] S.-Y. Wu, Y.-S. Tung, F. Marquet, M. E. Downs, C. S. Sanchez, C. C. Chen, V. Ferrera, and E. Konofagou, "Transcranial cavitation detection in primates during blood-brain barrier opening—a performance assessment study," *IEEE transactions on ultrasonics, ferroelectrics, and frequency control*, vol. 61, no. 6, pp. 966–978, 2014.
- [77] S. Wang, J. A. Hossack, and A. L. Klibanov, "Targeting of microbubbles: contrast agents for ultrasound molecular imaging," *Journal of drug targeting*, vol. 26, no. 5-6, pp. 420–434, 2018.
- [78] S. M. Chowdhury, L. Abou-Elkacem, T. Lee, J. Dahl, and A. M. Lutz, "Ultrasound and microbubble mediated therapeutic delivery: Underlying mechanisms and future outlook," *Journal of Controlled Release*, 2020.

- [79] N. Rosenthal and S. Brown, “The mouse ascending: perspectives for human-disease models,” *Nature cell biology*, vol. 9, no. 9, pp. 993–999, 2007.
- [80] E. Vlaisavljevich, J. Greve, X. Cheng, K. Ives, J. Shi, L. Jin, A. Arvidson, T. Hall, T. H. Welling, G. Owens, *et al.*, “Non-invasive ultrasound liver ablation using histotripsy: chronic study in an in vivo rodent model,” *Ultrasound in medicine & biology*, vol. 42, no. 8, pp. 1890–1902, 2016.
- [81] T. Worlikar, M. Mendiratta-Lala, E. Vlaisavljevich, R. Hubbard, J. Shi, T. L. Hall, C. S. Cho, F. T. Lee, J. Greve, and Z. Xu, “Effects of histotripsy on local tumor progression in an in vivo orthotopic rodent liver tumor model,” *BME frontiers*, vol. 2020, 2020.
- [82] S. Qu, T. Worlikar, A. E. Felsted, A. Ganguly, M. V. Beems, R. Hubbard, A. L. Pepple, A. A. Kevelin, H. Garavaglia, J. Dib, *et al.*, “Non-thermal histotripsy tumor ablation promotes abscopal immune responses that enhance cancer immunotherapy,” *Journal for ImmunoTherapy of Cancer*, vol. 8, no. 1, 2020.
- [83] W. H. Miller, C. Hartmann-Siantar, D. Fisher, M.-A. Descalle, T. Daly, J. Lehmann, M. R. Lewis, T. Hoffman, J. Smith, P. D. Situ, *et al.*, “Evaluation of beta-absorbed fractions in a mouse model for 90y, 188re, 166ho, 149pm, 64cu, and 177lu radionuclides,” *Cancer biotherapy & radiopharmaceuticals*, vol. 20, no. 4, pp. 436–449, 2005.
- [84] M. Chavez, M. T. Silvestrini, E. S. Ingham, B. Z. Fite, L. M. Mahakian, S. M. Tam, A. Ilovitsh, A. M. Monjazebe, W. J. Murphy, N. E. Hubbard, *et al.*, “Distinct immune signatures in directly treated and distant tumors result from tlr adjuvants and focal ablation,” *Theranostics*, vol. 8, no. 13, p. 3611, 2018.
- [85] A. Eranki, P. Srinivasan, M. Ries, A. Kim, C. A. Lazarski, C. T. Rossi, T. D. Khokhlova, E. Wilson, S. M. Knoblach, K. V. Sharma, *et al.*, “High-intensity focused ultrasound (hifu) triggers immune sensitization of refractory murine neuroblastoma to checkpoint inhibitor therapy,” *Clinical Cancer Research*, 2019.
- [86] A. M. Lake, T. L. Hall, K. Kieran, J. B. Fowlkes, C. A. Cain, and W. W. Roberts, “Histotripsy: minimally invasive technology for prostatic tissue ablation in an in vivo canine model,” *Urology*, vol. 72, no. 3, pp. 682–686, 2008.
- [87] T. D. Khokhlova, Y. A. Haider, A. D. Maxwell, W. Kreider, M. R. Bailey, and V. A. Khokhlova, “Dependence of boiling histotripsy treatment efficiency on hifu frequency and focal pressure levels,” *Ultrasound in medicine & biology*, vol. 43, no. 9, pp. 1975–1985, 2017.
- [88] N. J. McDannold, N. I. Vykhodtseva, and K. Hynynen, “Microbubble contrast agent with focused ultrasound to create brain lesions at low power levels: Mr imaging and histologic study in rabbits,” *Radiology*, vol. 241, no. 1, pp. 95–106, 2006.

- [89] D. L. Miller, N. B. Smith, M. R. Bailey, G. J. Czarnota, K. Hynynen, and I. R. S. Makin, "Overview of therapeutic ultrasound applications and safety considerations.," *Journal of ultrasound in medicine : official journal of the American Institute of Ultrasound in Medicine*, vol. 31, pp. 623–34, Apr 2012.
- [90] W. R. Cook, H. Jaffe, and B. Jaffe, *Piezoelectric ceramics*. 1971.
- [91] C. Corporation, "Piezoelectric polycrystalline (pzt) components and wafers," Product Specification 2017.04, CTS Corporation, April 2017.
- [92] T. Gururaja, W. A. Schulze, L. E. Cross, R. E. Newnham, B. A. Auld, Y. J. Wang, *et al.*, "Piezoelectric composite materials for ultrasonic transducer applications. part i: Resonant modes of vibration of pzt rod-polymer composites," *IEEE Trans. Sonics Ultrason*, vol. 32, no. 19985, pp. 481–498, 1985.
- [93] T. Gururaja, W. A. Schulze, L. E. Cross, and R. E. Newnham, "Piezoelectric composite materials for ultrasonic transducer applications. part ii: Evaluation of ultrasonic medical applications," *IEEE Transactions on sonics and ultrasonics*, vol. 32, no. 4, pp. 499–513, 1985.
- [94] W. A. Smith and B. A. Auld, "Modeling 1-3 composite piezoelectrics: thickness-mode oscillations," *IEEE transactions on ultrasonics, ferroelectrics, and frequency control*, vol. 38, no. 1, pp. 40–47, 1991.
- [95] J. A. Brown, S. Sharma, J. Leadbetter, S. Cochran, and R. Adamson, "Mass-spring matching layers for high-frequency ultrasound transducers: A new technique using vacuum deposition," *IEEE transactions on ultrasonics, ferroelectrics, and frequency control*, vol. 61, no. 11, pp. 1911–1921, 2014.
- [96] J. Woodacre, T. Landry, and J. Brown, "Real-time imaging, targeting, and ablation of ex-vivo tissue using a handheld histotripsy transducer and coregistered 64-element high-frequency endoscopic phased array," in *2016 IEEE international ultrasonics symposium (IUS)*, pp. 1–4, IEEE, 2016.
- [97] M. Mallay, J. Woodacre, T. Take, E. Napier, S. Gorgey, and J. Brown, "A miniature 16-element endoscopic histotripsy transducer with electronically steerable focus," in *2019 IEEE International Ultrasonics Symposium (IUS)*, pp. 1797–1800, IEEE, 2019.
- [98] M. Mallay, J. Woodacre, T. Landry, and J. Brown, "A 10 mm aperture 8-element annular array histotripsy transducer," in *2021 IEEE International Ultrasonics Symposium (IUS)*, pp. 1–4, IEEE, 2021.
- [99] R. Krimholtz, D. A. Leedom, and G. L. Matthaei, "New equivalent circuits for elementary piezoelectric transducers," *Electronics Letters*, vol. 6, no. 13, pp. 398–399, 1970.

- [100] D. Leedom, R. Krimholtz, and G. Matthaei, "Equivalent circuits for transducers having arbitrary even-or odd-symmetry piezoelectric excitation," *IEEE Transactions on Sonics and Ultrasonics*, vol. 18, no. 3, pp. 128–141, 1971.
- [101] B. E. Treeby and B. T. Cox, "k-wave: Matlab toolbox for the simulation and reconstruction of photoacoustic wave fields," *Journal of biomedical optics*, vol. 15, no. 2, p. 021314, 2010.
- [102] J. K. Woodacre, T. G. Landry, and J. A. Brown, "A low-cost miniature histotripsy transducer for precision tissue ablation," *IEEE transactions on ultrasonics, ferroelectrics, and frequency control*, vol. 65, no. 11, pp. 2131–2140, 2018.
- [103] Y. Mondorf, M. Abu-Owaimer, M. R. Gaab, and J. M. Oertel, "Chronic subdural hematoma-craniotomy versus burr hole trepanation," *British Journal of Neurosurgery*, vol. 23, no. 6, pp. 612–616, 2009.
- [104] Y.-F. Zhou, "High intensity focused ultrasound in clinical tumor ablation," *World Journal of Clinical Oncology*, vol. 2, no. 1, pp. 8–27, 2011.
- [105] O. Al-Bataineh, J. Jenne, and P. Huber, "Clinical and future applications of high intensity focused ultrasound in cancer," *Cancer Treatment Reviews*, vol. 38, no. 5, pp. 346–353, 2012.
- [106] A. M. Lake, T. L. Hall, K. Kieran, B. J. Fowlkes, C. A. Cain, and W. W. Roberts, "Histotripsy: minimally invasive technology for prostatic tissue ablation in an in vivo canine model," *Urology*, vol. 72, no. 4, pp. 682–686, 2008.
- [107] E. Vlasisavljevich, Y. Kim, S. Allen, G. Owens, S. Pelletier, C. Cain, K. Ives, and Z. Xu, "Image-guided non-invasive ultrasound liver ablation using histotripsy: feasibility study in an in vivo porcine model," *Ultrasound in medicine and biology*, vol. 39, no. 8, pp. 1398–1409, 2013.
- [108] A. D. Maxwell, G. Owens, H. S. Gurm, K. Ives, D. D. Myers, and Z. Xu, "Non-invasive treatment of deep venous thrombosis using pulsed ultrasound cavitation therapy (histotripsy) in a porcine model," *Journal of Vascular and Interventional Radiology*, vol. 22, no. 3, pp. 369–377, 2011.
- [109] J. Tavakkoli, R. Seip, V. V. Rao, R. F. Paterson, A. P. Evan, A. L. Shalhav, and N. T. Sanghvi, "A laparoscopic hifu probe for kidney ablation prior to partial nephrectomy," in *2001 IEEE Ultrasonics Symposium. Proceedings. An International Symposium (Cat. No.01CH37263)*, vol. 2, pp. 1369–1372 vol.2, 2001.
- [110] W. W. Roberts, T. L. Hall, K. Ives, J. S. Wolf, J. B. Fowlkes, and C. A. Cain, "Pulsed cavitation ultrasound: A noninvasive technology for controlled tissue ablation (histotripsy) in the rabbit kidney," *The Journal of Urology*, vol. 175, no. 2, pp. 734–738, 2006.

- [111] A. D. Maxwell, T.-Y. Wang, C. A. Cain, J. B. Fowlkes, O. A. Sapozhnikov, M. R. Bailey, and Z. Xu, "Cavitation clouds created by shock scattering from bubbles during histotripsy," *The Journal of the Acoustical Society of America*, vol. 130, no. 4, pp. 1888–1898, 2011.
- [112] N. R. Styn, J. C. Wheat, L. Hall, Timothy, and W. W. Roberts, "Histotripsy of vx-2 tumor implanted in a renal rabbit model," *Journal of Endourology*, vol. 24, no. 7, pp. 1145–1150, 2010.
- [113] K.-W. Lin, A. P. Duryea, Y. Kim, T. L. Hall, Z. Xu, and C. A. Cain, "Dual-beam histotripsy: a low-frequency pump enabling a high-frequency probe for precise lesion formation.," *IEEE transactions on ultrasonics, ferroelectrics, and frequency control*, vol. 61, pp. 325–40, Feb 2014.
- [114] E. Vlasisavljevich, K.-W. Lin, A. Maxwell, M. T. Warnez, L. Mancia, R. Singh, A. J. Putnam, B. Fowlkes, E. Johnsen, C. Cain, and Z. Xu, "Effects of ultrasound frequency and tissue stiffness on the histotripsy intrinsic threshold for cavitation," *Ultrasound in Medicine and Biology*, vol. 41, no. 6, pp. 1651–1667, 2015.
- [115] H. W. Baac, T. Lee, J. G. Ok, T. Hall, and L. Jay Guo, "Dual-frequency focused ultrasound using optoacoustic and piezoelectric transmitters for single-pulsed free-field cavitation in water," *Applied Physics Letters*, vol. 103, no. 23, p. 234103, 2013.
- [116] T. Lee, J. G. Ok, L. J. Guo, and H. W. Baac, "Low f-number photoacoustic lens for tight ultrasonic focusing and free-field micro-cavitation in water," *Applied Physics Letters*, vol. 108, no. 10, p. 104102, 2016.
- [117] T. Lee, W. Luo, Q. Li, H. Demirci, and L. J. Guo, "Laser-induced focused ultrasound for cavitation treatment: Toward high-precision invisible sonic scalpel," *small*, vol. 13, no. 38, p. 1701555, 2017.
- [118] J. Kim, B. D. Lindsey, W.-Y. Chang, X. Dai, J. M. Stavas, P. A. Dayton, and X. Jiang, "Intravascular forward-looking ultrasound transducers for microbubble-mediated sonothrombolysis," *Scientific reports*, vol. 7, no. 1, p. 3454, 2017.
- [119] J. R. Sukovich, Z. Xu, Y. Kim, H. Cao, T.-S. Nguyen, A. S. Pandey, T. L. Hall, and C. A. Cain, "Targeted lesion generation through the skull without aberration correction using histotripsy," *IEEE transactions on ultrasonics, ferroelectrics, and frequency control*, vol. 63, no. 5, pp. 671–682, 2016.
- [120] W. Smith, A. Shaulov, and B. Singer, "Properties of composite piezoelectric materials for ultrasonic transducers," in *IEEE 1984 Ultrasonics Symposium*, pp. 539–544, IEEE, 1984.

- [121] K.-B. Kim, D. K. Hsu, B. Ahn, Y.-G. Kim, and D. J. Barnard, "Fabrication and comparison of pmn-pt single crystal, pzt and pzt-based 1-3 composite ultrasonic transducers for nde applications.," *Ultrasonics*, vol. 50, pp. 790–7, Aug 2010.
- [122] C. Dang, *Electromechanical characterization of ultrasonic NDE systems*. PhD thesis, Iowa State, 2001.
- [123] F. Levassort, L.-P. Tran-Huu-Hue, P. Marechal, E. Ringgaard, and M. Lethiecq, "Characterization of thin layers of parylene at high frequency using pzt thick film resonators," *Journal of the European Ceramic Society*, vol. 25, pp. 2985–2989, 2005.
- [124] P. Maréchal, F. Levassort, L.-P. Tran-Huu-Hue, and M. Lethiecq, "Lens-focused transducer modeling using an extended klm model.," *Ultrasonics*, vol. 46, pp. 155–67, May 2007.
- [125] R. S. Cobbold, *Foundations of biomedical ultrasound*. Oxford University Press, 2006.
- [126] J. A. Brown and G. R. Lockwood, "Low-cost, high-performance pulse generator for ultrasound imaging," *IEEE Transactions on Ultrasonics, Ferroelectrics, and Frequency Control*, vol. 49, pp. 848–851, June 2002.
- [127] E. Vlaisavljevich, T. Gerhardson, T. Hall, and Z. Xu, "Effects of f-number on the histotripsy intrinsic threshold and cavitation bubble cloud behavior," *Physics in Medicine & Biology*, vol. 62, no. 4, p. 1269, 2017.
- [128] E. Vlaisavljevich, A. Maxwell, M. Warnez, E. Johnsen, C. A. Cain, and Z. Xu, "Histotripsy-induced cavitation cloud initiation thresholds in tissues of different mechanical properties," *IEEE Transactions on Ultrasonics, Ferroelectrics, and Frequency Control*, vol. 61, pp. 341–352, February 2014.
- [129] J. K. Woodacre, T. G. Landry, and J. A. Brown, "Fabrication and characterization of a 5 mm x 5mm aluminum lens based histotripsy transducer," *IEEE Transactions on Ultrasonics, Ferroelectrics, and Frequency Control*, 2022.
- [130] Z. Xu, T. L. Hall, E. Vlaisavljevich, and F. T. Lee Jr, "Histotripsy: the first non-invasive, non-ionizing, non-thermal ablation technique based on ultrasound," *International Journal of Hyperthermia*, vol. 38, no. 1, pp. 561–575, 2021.
- [131] A. D. Maxwell, C. A. Cain, T. L. Hall, J. B. Fowlkes, and Z. Xu, "Probability of cavitation for single ultrasound pulses applied to tissues and tissue-mimicking materials," *Ultrasound in medicine & biology*, vol. 39, no. 3, pp. 449–465, 2013.
- [132] F. Levassort, L.-P. Tran-Huu-Hue, P. Marechal, E. Ringgaard, and M. Lethiecq, "Characterisation of thin layers of parylene at high frequency using pzt thick film resonators," *Journal of the European Ceramic Society*, vol. 25, no. 12, pp. 2985–2989, 2005.

- [133] MATLAB, *version 9.9.0 (R2020b)*. Natick, Massachusetts: The MathWorks Inc., 2020.
- [134] J. Soneson, “Hitu simulator v2.0.” Acquired from https://github.com/jsoneson/HITU_Simulator, on date 2022-02-22.
- [135] G. Paxinos and C. Watson, *The Rat Brain in Stereotaxic Coordinates: Hard Cover Edition*. Academic Press, 2013.
- [136] T. G. Landry and J. A. Brown, “B-mode and doppler imaging of in vivo rat brain and ex vivo human brain with a high frequency endoscopic phased array,” in *2019 IEEE International Ultrasonics Symposium (IUS)*, pp. 2133–2136, IEEE, 2019.
- [137] T. Landry, M. Mallay, N. Campbell, E. Vlasisavljevich, and J. Brown, “In-vivo high-resolution imaging + histotripsy in rat brains using a combined endoscopic device [conference presentation],” in *2021 IEEE International Ultrasonics Symposium (IUS)*, IEEE, 2021.
- [138] J. Woodacre, E. Simpson, and J. Brown, “A 5 mm × 5 mm square, aluminum lens based histotripsy transducer: Reaching the endoscopic form factor,” in *2018 IEEE International Ultrasonics Symposium (IUS)*, pp. 1–4, IEEE, 2018.
- [139] R. Krimholtz, D. Leedom, and G. Matthaei, “New equivalent circuits for elementary piezoelectric transducers,” *Electronics Letters*, vol. 6, no. 13, pp. 398–399, 1970.
- [140] J. Woodacre and J. Brown, “An evaluation of pzt5a, pin-pmn-pt single crystal, and high-dielectric pzt for a 5mm x 5mm histotripsy transducer,” in *2019 IEEE International Ultrasonics Symposium (IUS)*, pp. 2596–2599, Oct 2019.
- [141] M. G. Mallay, J. K. Woodacre, T. G. Landry, N. A. Campbell, and J. A. Brown, “A dual frequency lens focused endoscopic histotripsy transducer,” *IEEE Transactions on Ultrasonics, Ferroelectrics, and Frequency Control*, 2021.
- [142] J. Gateau, J. Aubry, D. Chauvet, A. Boch, M. Fink, and M. Tanter, “In vivo bubble nucleation probability in sheep brain tissue,” *Physics in Medicine & Biology*, vol. 56, no. 22, p. 7001, 2011.
- [143] S. Goss, L. Frizzell, and F. Dunn, “Ultrasonic absorption and attenuation in mammalian tissues,” *Ultrasound in medicine & biology*, vol. 5, no. 2, pp. 181–186, 1979.
- [144] M. M. Callesen, S. S. Árnadóttir, I. Lyskjær, M.-B. W. Ørntoft, S. Høyer, F. Dagnæs-Hansen, Y. Liu, R. Li, H. Callesen, M. H. Rasmussen, *et al.*, “A genetically inducible porcine model of intestinal cancer,” *Molecular oncology*, vol. 11, no. 11, pp. 1616–1629, 2017.

- [145] J. L. Rowell, D. O. McCarthy, and C. E. Alvarez, “Dog models of naturally occurring cancer,” *Trends in molecular medicine*, vol. 17, no. 7, pp. 380–388, 2011.
- [146] A. Parvinian, L. C. Casadaban, and R. C. Gaba, “Development, growth, propagation, and angiographic utilization of the rabbit vx2 model of liver cancer: a pictorial primer and “how to” guide,” *Diagnostic and interventional radiology*, vol. 20, no. 4, p. 335, 2014.
- [147] J. A. Brown and G. R. Lockwood, “A low-cost, high-performance pulse generator for ultrasound imaging,” *IEEE transactions on ultrasonics, ferroelectrics, and frequency control*, vol. 49, pp. 848–51, Jun 2002.

Appendix A

Copyright Permissions

Figure 1.1 - 145 mm histotripsy transducer

WOLTERS KLUWER HEALTH, INC. LICENSE TERMS AND CONDITIONS

Nov 26, 2021

This Agreement between Mr. Jeffrey Woodacre ("You") and Wolters Kluwer Health, Inc. ("Wolters Kluwer Health, Inc.") consists of your license details and the terms and conditions provided by Wolters Kluwer Health, Inc. and Copyright Clearance Center.

License Number 5196511069048

License date Nov 26, 2021

Licensed Content Publisher Wolters Kluwer Health, Inc.

Licensed Content Publication Journal of Urology

Licensed Content Title Pulsed Cavitation Ultrasound: A Noninvasive Technology for Controlled Tissue Ablation (Histotripsy) in the Rabbit Kidney

Licensed Content Author William W. Roberts, Timothy L. Hall, Kimberly Ives, et al

Licensed Content Date Nov 9, 2018

Licensed Content Volume 175

Licensed Content Issue 2

Type of Use Dissertation/Thesis

Requestor type University/College

Sponsorship No Sponsorship

Format Electronic

Will this be posted online? Yes, on an unrestricted website

Portion Figures/tables/illustrations

Number of figures/tables/illustrations 1

Author of this Wolters Kluwer article No

Will you be translating? No

Intend to modify/change the content No

Title On the Development of Small Form Factor Histotripsy Devices for Neurosurgical Applications and Small Animal Experiments

Institution name Dalhousie University

Expected presentation date Mar 2022

Portions Figure 1: Image on page 2 of annular phase array ultrasound system at bottom of degassed water tank.

Terms and Conditions

Wolters Kluwer Health Inc. Terms and Conditions Duration of License: Permission is granted for a one time use only. Rights herein do not apply to future reproductions, editions, revisions, or other derivative works. This permission shall be effective as of the date of execution by the parties for the maximum period of 12 months and should be renewed after the term expires. When content is to be republished in a book or journal the validity of this agreement should be the life of the book edition or journal issue. When content is licensed for use on a website, internet, intranet, or any publicly accessible site (not including a journal or book), you agree to remove the material from such site after 12 months, or request to renew your permission license Credit Line: A credit line must be prominently placed and include: For book content: the author(s), title of book, edition, copyright holder, year of publication; For journal content: the author(s), titles of article, title of journal, volume number, issue number, inclusive pages and website URL to the journal page; If a journal is published by a learned society the credit line must include the details of that society. Warranties: The requestor warrants that the material shall not be used in any manner which may be considered derogatory to the title, content, authors of the material, or to Wolters Kluwer Health, Inc. Indemnity: You hereby indemnify and hold harmless Wolters Kluwer Health, Inc. and its respective officers, directors, employees and agents, from and against any and all claims, costs, proceeding or demands arising out of your unauthorized use of the Licensed Material Geographical Scope: Permission granted is non-exclusive and is valid throughout the world in the English language and the languages specified in the license.

Figure 2.1 - Comparison of Ablation Types

Source: V. A. Khokhlova, P. V. Yuldashev, P. B. Rosnitskiy, A. D. Maxwell, W. Kreider, M. R. Bailey, and O. A. Sapozhnikov, "Design of hifu transducers to generate specific nonlinear ultrasound fields," *Physics procedia*, vol. 87, pp. 132–138, 2016;

This article [and its contents] is available under the Creative Commons CC-BY-NC-ND license and permits non-commercial use of the work as published, without adaptation or alteration provided the work is fully attributed.

Figure 2.2 - HIFU Transducer and Ablation Pattern

SPRINGER NATURE LICENSE TERMS AND CONDITIONS

Jan 30, 2022

This Agreement between Mr. Jeffrey Woodacre ("You") and Springer Nature ("Springer Nature") consists of your license details and the terms and conditions provided by Springer Nature and Copyright Clearance Center. License Number

5238920498909

License date

Jan 30, 2022
Licensed Content Publisher
Springer Nature
Licensed Content Publication
Springer eBook
Licensed Content Title
HIFU Tissue Ablation: Concept and Devices
Licensed Content Author
Gail ter Haar
Licensed Content Date
Jan 1, 2016
Type of Use
Thesis/Dissertation
Requestor type
non-commercial (non-profit)
Format
electronic
Portion
figures/tables/illustrations
Number of figures/tables/illustrations
2
Will you be translating?
no
Circulation/distribution
1 - 29
Author of this Springer Nature content
no
Title
On the Development of Small Form Factor Histotripsy Devices for Neurosurgical
Applications and Small Animal Experiments
Institution name
Dalhousie University
Expected presentation date
Mar 2022
Portions
Figures 1.1 and 1.5
Requestor Location
Mr. Jeffrey Woodacre 5790 University Avenue Room 233
Halifax, NS B3H1V7 Canada Attn: Jeffrey Woodacre
Total
0.00 USD
Terms and Conditions
Springer Nature Customer Service Centre GmbH Terms and Conditions

This agreement sets out the terms and conditions of the licence (the Licence) between you and Springer Nature Customer Service Centre GmbH (the Licensor). By clicking 'accept' and completing the transaction for the material (Licensed Material), you also confirm your acceptance of these terms and conditions.

Grant of License

The Licensor grants you a personal, non-exclusive, non-transferable, world-wide licence to reproduce the Licensed Material for the purpose specified in your order only. Licences are granted for the specific use requested in the order and for no other use, subject to the conditions below.

The Licensor warrants that it has, to the best of its knowledge, the rights to license reuse of the Licensed Material. However, you should ensure that the material you are requesting is original to the Licensor and does not carry the copyright of another entity (as credited in the published version).

If the credit line on any part of the material you have requested indicates that it was reprinted or adapted with permission from another source, then you should also seek permission from that source to reuse the material.

Scope of Licence

You may only use the Licensed Content in the manner and to the extent permitted by these TsCs and any applicable laws.

A separate licence may be required for any additional use of the Licensed Material, e.g. where a licence has been purchased for print only use, separate permission must be obtained for electronic re-use. Similarly, a licence is only valid in the language selected and does not apply for editions in other languages unless additional translation rights have been granted separately in the licence. Any content owned by third parties are expressly excluded from the licence.

Similarly, rights for additional components such as custom editions and derivatives require additional permission and may be subject to an additional fee. Please apply to Journalpermissions@springernature.com/bookpermissions@springernature.com for these rights.

Where permission has been granted free of charge for material in print, permission may also be granted for any electronic version of that work, provided that the material is incidental to your work as a whole and that the electronic version is essentially equivalent to, or substitutes for, the print version.

An alternative scope of licence may apply to signatories of the STM Permissions Guidelines, as amended from time to time.

Duration of Licence

A licence for is valid from the date of purchase ('Licence Date') at the end of the relevant period in the below table:

Scope of Licence	Duration of Licence	Post on a website	12 months	Presentations
	12 months	Books and journals	Lifetime	of the edition in the language purchased

Acknowledgement

The Licensor's permission must be acknowledged next to the Licenced Material in print. In electronic form, this acknowledgement must be visible at the same time as

the figures/tables/illustrations or abstract, and must be hyperlinked to the journal/book's homepage. Our required acknowledgement format is in the Appendix below.

Restrictions on use

Use of the Licensed Material may be permitted for incidental promotional use and minor editing privileges e.g. minor adaptations of single figures, changes of format, colour and/or style where the adaptation is credited as set out in Appendix 1 below. Any other changes including but not limited to, cropping, adapting, omitting material that affect the meaning, intention or moral rights of the author are strictly prohibited. You must not use any Licensed Material as part of any design or trademark.

Licensed Material may be used in Open Access Publications (OAP) before publication by Springer Nature, but any Licensed Material must be removed from OAP sites prior to final publication.

Ownership of Rights

Licensed Material remains the property of either Licensor or the relevant third party and any rights not explicitly granted herein are expressly reserved.

Warranty

IN NO EVENT SHALL LICENSOR BE LIABLE TO YOU OR ANY OTHER PARTY OR ANY OTHER PERSON OR FOR ANY SPECIAL, CONSEQUENTIAL, INCIDENTAL OR INDIRECT DAMAGES, HOWEVER CAUSED, ARISING OUT OF OR IN CONNECTION WITH THE DOWNLOADING, VIEWING OR USE OF THE MATERIALS REGARDLESS OF THE FORM OF ACTION, WHETHER FOR BREACH OF CONTRACT, BREACH OF WARRANTY, TORT, NEGLIGENCE, INFRINGEMENT OR OTHERWISE (INCLUDING, WITHOUT LIMITATION, DAMAGES BASED ON LOSS OF PROFITS, DATA, FILES, USE, BUSINESS OPPORTUNITY OR CLAIMS OF THIRD PARTIES), AND WHETHER OR NOT THE PARTY HAS BEEN ADVISED OF THE POSSIBILITY OF SUCH DAMAGES. THIS LIMITATION SHALL APPLY NOTWITHSTANDING ANY FAILURE OF ESSENTIAL PURPOSE OF ANY LIMITED REMEDY PROVIDED HEREIN.

Limitations

BOOKS ONLY:Where 'reuse in a dissertation/thesis' has been selected the following terms apply: Print rights of the final author's accepted manuscript (for clarity, NOT the published version) for up to 100 copies, electronic rights for use only on a personal website or institutional repository as defined by the Sherpa guideline (www.sherpa.ac.uk/romeo/).

For content reuse requests that qualify for permission under the STM Permissions Guidelines, which may be updated from time to time, the STM Permissions Guidelines supersede the terms and conditions contained in this licence.

Termination and Cancellation

Licences will expire after the period shown in Clause 3 (above).

Licensee reserves the right to terminate the Licence in the event that payment is not received in full or if there has been a breach of this agreement by you.

Figure 2.4 - Shock-scatter method of action

This Agreement between Mr. Jeffrey Woodacre ("You") and AIP Publishing ("AIP Publishing") consists of your license details and the terms and conditions provided by AIP Publishing and Copyright Clearance Center.

License Number 5196630687541

License date Nov 26, 2021

Licensed Content Publisher Acoustical Society of America

Licensed Content Publication The Journal of the Acoustical Society of America

Licensed Content Title Cavitation clouds created by shock scattering from bubbles during histotripsy

Licensed Content Author Adam D. Maxwell, Tzu-Yin Wang, Charles A. Cain, et al

Licensed Content Date Oct 1, 2011

Licensed Content Volume 130

Licensed Content Issue 4

Type of Use Thesis/Dissertation

Requestor type Student

Format Print and electronic

Portion Figure/Table

Number of figures/tables 1

Will you be translating? No

Title On the Development of Small Form Factor Histotripsy Devices for Neurosurgical Applications and Small Animal Experiments

Institution name Dalhousie University

Expected presentation date Mar 2022

Portions FFigure 4 Figure 8

Requestor Location Mr. Jeffrey Woodacre 5790 University Avenue Room 233


Halifax, NS B3H1V7 Canada Attn: Jeffrey Woodacre

Figure 2.5 - Boiling Histotripsy

Source: A. Maxwell, O. Sapozhnikov, M. Bailey, L. Crum, Z. Xu, B. Fowlkes, C. Cain, and V. Khokhlova, "Disintegration of tissue using high intensity focused ultrasound: Two approaches that utilize shock waves," *Acoustics Today*, vol. 8, no. 4, pp. 24-36, 2012;

used in accordance with the Creative Commons Attribution (CC BY) license: (<https://creativecommons.org/licenses/by/4.0/>).

Figure 2.6 - Shock waves and bubble cloud size



Microtripsy beyond the intrinsic cavitation threshold using very short ultrasound pulses: microtripsy

Author: Kuang-Wei Lin
 Publication: IEEE Transactions on Ultrasonics, Ferroelectrics, and Frequency Control
 Publisher: IEEE
 Date: February 2014

Copyright © 2014, IEEE

Thesis / Dissertation Reuse

The IEEE does not require individuals working on a thesis to obtain a formal reuse license, however, you may print out this statement to be used as a permission grant:

Requirements to be followed when using any portion (e.g., figure, graph, table, or textual material) of an IEEE copyrighted paper in a thesis:

- 1) In the case of textual material (e.g., using short quotes or referring to the work within these papers) users must give full credit to the original source (author, paper, publication) followed by the IEEE copyright line © 2011 IEEE.
- 2) In the case of illustrations or tabular material, we require that the copyright line © [Year of original publication] IEEE appear prominently with each reprinted figure and/or table.
- 3) If a substantial portion of the original paper is to be used, and if you are not the senior author, also obtain the senior author's approval.

Requirements to be followed when using an entire IEEE copyrighted paper in a thesis:

- 1) The following IEEE copyright/ credit notice should be placed prominently in the references: © [year of original publication] IEEE. Reprinted, with permission, from [author names, paper title, IEEE publication title, and month/year of publication]
- 2) Only the accepted version of an IEEE copyrighted paper can be used when posting the paper or your thesis online.
- 3) In placing the thesis on the author's university website, please display the following message in a prominent place on the website: In reference to IEEE copyrighted material which is used with permission in this thesis, the IEEE does not endorse any of [university/educational entity's name goes here]'s products or services. Internal or personal use of this material is permitted. If interested in reprinting/republishing IEEE copyrighted material for advertising or promotional purposes or for creating new collective works for resale or redistribution, please go to http://www.ieee.org/publications_standards/publications/rights/rights_link.html to learn how to obtain a License from RightsLink.

If applicable, University Microfilms and/or ProQuest Library, or the Archives of Canada may supply single copies of the dissertation.

Figure 2.7 - Blood Brain Barrier Tight Junctions Opening

SPRINGER NATURE LICENSE TERMS AND CONDITIONS

Nov 29, 2021

This Agreement between Mr. Jeffrey Woodacre ("You") and Springer Nature ("Springer Nature") consists of your license details and the terms and conditions provided by Springer Nature and Copyright Clearance Center. License Number 5198330507666
License date Nov 29, 2021

Licensed Content Publisher Springer Nature

Licensed Content Publication Springer eBook

Licensed Content Title Microbubble-Assisted Ultrasound for Drug Delivery in the Brain and Central Nervous System

Licensed Content Author Alison Burgess, Kullervo Hynynen

Licensed Content Date Jan 1, 2016

Type of Use Thesis/Dissertation

Requestor type non-commercial (non-profit)

Format print and electronic

Portion figures/tables/illustrations

Number of figures/tables/illustrations 1

Will you be translating? no

Circulation/distribution 1 - 29

Author of this Springer Nature content no

Title On the Development of Small Form Factor Histotripsy Devices for Neurosurgical Applications and Small Animal Experiments

Institution name Dalhousie University

Expected presentation date Mar 2022

Portions Figure 16.2

Requestor Location Mr. Jeffrey Woodacre 5790 University Avenue Room 233 Halifax, NS B3H1V7 Canada Attn: Jeffrey Woodacre

Figure 2.8 - Microbubbles Method of Action

ELSEVIER LICENSE TERMS AND CONDITIONS

Apr 09, 2022

This Agreement between Mr. Jeffrey Woodacre ("You") and Elsevier ("Elsevier") consists of your license details and the terms and conditions provided by Elsevier and Copyright Clearance Center. License Number 5284910451309

License date

Apr 09, 2022

Licensed Content Publisher

Elsevier

Licensed Content Publication

Journal of Controlled Release

Licensed Content Title
Ultrasound and microbubble mediated therapeutic delivery: Underlying mechanisms and future outlook

Licensed Content Author
Sayan Mullick Chowdhury, Lotfi Abou-Elkacem, Taehwa Lee, Jeremy Dahl, Amelie M. Lutz

Licensed Content Date
Oct 10, 2020

Licensed Content Volume
326

Licensed Content Issue
n/a

Licensed Content Pages
16

Start Page
75

End Page
90

Type of Use
reuse in a thesis/dissertation

Portion
figures/tables/illustrations

Number of figures/tables/illustrations
1

Format
electronic

Are you the author of this Elsevier article?
No

Will you be translating?
No

Title
On the Development of Small Form Factor Histotripsy Devices for Neurosurgical Applications and Small Animal Experiments

Institution name
Dalhousie University

Expected presentation date
Apr 2022

Portions
Figure 1

Requestor Location
Mr. Jeffrey Woodacre 5790 University Avenue Room 233 Halifax, NS B3H1V7
Canada

Chapters 4 and 5 - IEEE Usage Requirements



A Low-Cost Miniature Histotripsy Transducer for Precision Tissue Ablation

Author: Jeffrey K. Woodacre

Publication: IEEE Transactions on Ultrasonics, Ferroelectrics, and Frequency Control

Publisher: IEEE

Date: Nov. 2018

Copyright © 2018, IEEE

Thesis / Dissertation Reuse

The IEEE does not require individuals working on a thesis to obtain a formal reuse license, however, you may print out this statement to be used as a permission grant:

Requirements to be followed when using any portion (e.g., figure, graph, table, or textual material) of an IEEE copyrighted paper in a thesis:

- 1) In the case of textual material (e.g., using short quotes or referring to the work within these papers) users must give full credit to the original source (author, paper, publication) followed by the IEEE copyright line © 2011 IEEE.
- 2) In the case of illustrations or tabular material, we require that the copyright line © [Year of original publication] IEEE appear prominently with each reprinted figure and/or table.
- 3) If a substantial portion of the original paper is to be used, and if you are not the senior author, also obtain the senior author's approval.

Requirements to be followed when using an entire IEEE copyrighted paper in a thesis:

- 1) The following IEEE copyright/ credit notice should be placed prominently in the references: © [year of original publication] IEEE. Reprinted, with permission, from [author names, paper title, IEEE publication title, and month/year of publication]
- 2) Only the accepted version of an IEEE copyrighted paper can be used when posting the paper or your thesis on-line.
- 3) In placing the thesis on the author's university website, please display the following message in a prominent place on the website: In reference to IEEE copyrighted material which is used with permission in this thesis, the IEEE does not endorse any of [university/educational entity's name goes here]'s products or services. Internal or personal use of this material is permitted. If interested in reprinting/republishing IEEE copyrighted material for advertising or promotional purposes or for creating new collective works for resale or redistribution, please go to http://www.ieee.org/publications_standards/publications/rights/rights_link.html to learn how to obtain a License from RightsLink.

If applicable, University Microfilms and/or ProQuest Library, or the Archives of Canada may supply single copies of the dissertation.